

**NUMERICAL ANALYSIS OF TRANSIENT TEFLON ABLATION IN
PULSED PLASMA THRUSTERS**

By

David Paul Stechmann

July 3rd, 2007

A Thesis submitted to the Faculty of
WORCESTER POLYTECHNIC INSTITUTE

In partial fulfillment of the requirements for the degree of

Master of Science

in

Mechanical Engineering

David Paul Stechmann

Approved:

Dr. Nikolaos A. Gatsonis, Advisor
Professor, Mechanical Engineering Department

Dr. John J. Blandino, Committee Member
Associate Professor, Mechanical Engineering Department

Dr. Islam I. Hussein, Committee Member
Assistant Professor, Mechanical Engineering Department

Lawrence Byrne, Committee Member
Research Engineer, BUSEK Co.

Dr. Mark W. Richman, Graduate Committee Representative
Associate Professor, Mechanical Engineering Department

Abstract

One of the general processes of interest in Pulsed Plasma Thrusters is the ablation of the solid fuel. In general, ablation occurs when a short pulse of applied energy removes a portion of the fuel surface. Although this ablation process is relatively straight-forward in simple materials that sublime, ablation in Pulsed Plasma Thrusters is significantly more complicated. This is caused by the transient conditions and the complex behavior of Teflon that does not sublime but rather undergoes both physical and chemical changes prior to leaving the surface. These two effects combine to make Teflon ablation a highly nonlinear function of heat flux, material property variations, changing molecular weight, and phase transformation behavior.

To gain greater insight into the ablation process, a one-dimensional ablation model is developed that addresses the more detailed thermal and thermodynamic behavior of Teflon during simulated operation of a Pulsed Plasma Thruster. The mathematical model is based on the work of *Clark* (1971), which focused on two-phase, one-dimensional Teflon ablation in the context of thermal protection systems. The model is modified for use in simulated PPT operations and implemented numerically using an adaptive non-uniform grid, explicit finite-difference techniques, and a volume fraction method to capture the interface between the crystalline and amorphous Teflon phases. The ablation model is validated against analytical heat transfer and ablation solutions and compared with previous experimental results.

The Teflon ablation model is used to analyze several general ablation scenarios in addition to specific PPT conditions to gain greater insight into long-duration thruster firing, post-pulse material ablation, variable heat flux effects, variable material property effects, and the impact of surface re-crystallization on particulate emission. These simulations are considered in the context of prior experimental investigations of Pulsed Plasma Thrusters. The results of these simulations demonstrate the success of the numerical ablation model in predicting experimental trend and suggest potential paths of moderately improving thruster efficiency and operational repeatability in the future.

Acknowledgements

I would like to thank all those who have made this work possible. They are far too numerous to mention, but I will attempt to list as many as possible starting with those at Worcester Polytechnic Institute. First, I would like to thank my advisor, Professor Nikolaos A. Gatsonis. His initiative in starting this project and continued support and insight into all the various challenges that arose throughout have been invaluable. Second, I would like to thank Professor Damir Juric for providing a solid and well constructed initial code framework to develop and expand upon. Third, I would like to thank Professor John Blandino for his wonderful reference material that allowed me to validate the computer code. Fourth, I would like to thank all those who worked behind the scenes to develop and fund this project including Lawrence Byrne at BUSEK Corporation, those at the Air Force Research Laboratory, and those at The Massachusetts Space Grant Consortium. Finally, I would like to thank my committee members, the faculty of the Aerospace office, the graduate students in the CGPL, and the Mechanical Engineering Department in general. You have all given me a home the last few years.

I am extremely grateful to the wonderful group of educators and mentors I have had over the years. These include those who gave me my initial education at Montessori, the amazing teachers at the Waldorf School, and the outstanding faculty of Totino-Grace high school. Thank you for giving me so many opportunities and never limiting me to one specific path of learning. Of course, this would not be complete without thanking the various instructors who managed and taught the summer camps, science programs, music lessons, dance lessons, flying lessons, gymnastics, theatre, and so many other activities I participated in throughout my educational career. I don't remember all of them because it has been too long, but their contributions will never be forgotten.

In conclusion, I would like to thank my parents Kathy and Eric, and my extended family. Thanks so much for looking over this work and offering suggestions and insight, for always instilling in me the desire to learn, and for making so many of the aforementioned educational opportunities possible. None of this would have been possible without you.

Table of Contents

Abstract.....	II
Acknowledgements	III
Table of Contents	IV
List of Figures.....	VI
List of Tables	IX
Nomenclature	X
Chapter 1: Introduction	1
1.1. Teflon Ablation Overview.....	4
1.2. Review of Experimental Ablation Studies	6
1.3. Review of Ablation Modeling	8
1.4. Review of Experimental PPT Studies.....	17
1.5. Review of PPT Modeling	18
1.6. Objectives and Approach.....	21
Chapter 2: One Dimensional Mathematical Model.....	25
2.1. Initial Conditions	25
2.2. First Ablation Stage	26
2.3. Second Ablation Stage.....	27
2.4. Third Ablation Stage.....	28
2.5. Material Properties.....	33
Chapter 3: One Dimensional Numerical Implementation	35
3.1. General Execution Sequence and Logic	35
3.2. Grid Generation and Volume Fraction Concept	38
3.3. Finite Difference Technique.....	43
3.4. Material Property Matrices	47
3.5. Heat Flux Interpolation.....	48
3.6. Virtual Probe Temperature Interpolation.....	49

3.7. Numerical Stability Analysis	49
3.8. A Computational Example	50
Chapter 4: Model Validation	56
4.1. Scenario One.....	57
4.2. Scenario Two	59
4.3. Scenario Three	61
4.4. Scenario Four.....	63
4.5. Scenario Five	66
4.6. Scenario Six	70
4.7. Scenario Seven.....	73
Chapter 5: Material Property Analysis	75
5.1. Material Property References	75
5.2. Effects of Property Error	78
Chapter 6: Pulsed Plasma Thruster Operational Analysis.....	84
6.1. Long-Duration PPT Pulsing	84
6.2. Particulate Emission	90
6.3. Effects of Variable Heat Flux	92
6.4. Effects of Variable Material Properties	96
Chapter 7: Conclusions	98
7.1. Implications for Pulsed Plasma Thrusters	99
7.2. Recommendations for Future Work	100
References.....	102
Appendix A: One Dimensional Program Architecture	106

List of Figures

Figure 1.1:	General schematic of the electrode and propellant arrangement in a solid fuel PPT.	2
Figure 1.2:	An example of a solid fuel PPT with a coaxial electrode configuration.	2
Figure 1.3:	General operational sequence of a single pulse fired on a coaxial solid-fuel pulsed plasma thruster.	3
Figure 1.4:	Two Examples of Crystalline Teflon shown relative to a paperclip.	5
Figure 1.5:	A Long Chain Teflon Polymer and a Teflon Monomer. Carbon atoms are black while Fluorine atoms are green. Bond angles are not exact.	6
Figure 1.6:	A general overview of the transient Teflon ablation process in a one-dimensional bar.	6
Figure 1.7:	Ablation Regions as defined by <i>Clark (1971)</i> .	10
Figure 1.8:	The XPPT-1 Pulsed Plasma Thruster during and immediately following a pulse. Particulate emission post-pulse is apparent (<i>Spanjers et al., 1998</i>)	18
Figure 2.1:	Initial Conditions for Mathematical Model	26
Figure 2.2:	Graphical depiction of the effective heat sink simulated by the heat sink boundary condition.	26
Figure 2.3:	Stage One Boundary Conditions	27
Figure 2.4:	Stage Two Boundary Conditions	28
Figure 2.5:	Detailed Representations of the different outer boundary components for the convective case in stage three operation (left) and the non-convective case in stage three operation (right).	31
Figure 2.6:	Stage Three Boundary Conditions and material phases for the convective case.	32
Figure 2.7:	Stage Three Boundary Conditions and material phases for the non-convective (PPT) case.	33
Figure 3.1:	General program execution structure	36
Figure 3.2:	Numerical grid with phase transformation and ablation boundaries	38
Figure 3.3:	Numerical grid with included representations of volume fractions.	39
Figure 3.4:	An example of the extreme temperature gradients present in a Pulsed Plasma Thruster	41
Figure 3.5:	The non-uniform grid methodology.	41
Figure 3.6:	The node transformation function applied to a typical domain 0.03 meters in length	43
Figure 3.7:	Pulsed heat flux profile applied sequentially at 1 second intervals in the example ablation scenario.	51

Figure 3.8:	Ablation rates during pulse 1 and pulse 360 as a function of pulse time in the example ablation scenario.....	52
Figure 3.9:	Temperature profiles in the entire Teflon domain at zero, 120, and 360 seconds prior to the start of the next applied heat flux sequence.....	53
Figure 3.10:	Thermocouple responses at three locations over the long duration simulation in the example Teflon domain.....	53
Figure 3.11:	Temperature profiles near the exposed Teflon surface at three time intervals after the start of the first pulse in the example pulse sequence.....	54
Figure 3.12:	Phase transformation boundary velocity and exposed surface ablation velocity during the first pulse in the example pulse sequence.	55
Figure 3.13:	Phase transformation boundary and exposed surface locations during the first pulse in the example pulse sequence.	55
Figure 4.1:	Temperature profile comparisons within the Teflon domain for Scenario One assumptions.	58
Figure 4.2:	Temperature profile comparisons within the Teflon domain using the assumptions and conditions of Scenario Two.	60
Figure 4.3:	Temperature profile used in the scenario three validation case shown with relative wall and node temperature values on a hybrid numerical and physical domain representation.	61
Figure 4.4:	Heat sink temperature response over time for the initial conditions and assumptions used in Scenario Three.	63
Figure 4.5:	Temperature profile comparisons within the Teflon domain for the assumptions used in Scenario Four.	66
Figure 4.6:	Temperature profile comparisons within the Teflon domain for the moving boundary assumptions of Scenario Five.	69
Figure 4.7:	Steady-State mass flux and surface recession velocity comparisons for the assumptions and conditions used in Scenario Six.	73
Figure 4.8:	Temperature profiles near the exposed surface as computed using a non-adaptive high resolution solution and a solution obtained using grid adaptation.	74
Figure 5.1:	Thermal conductivity relative to Teflon temperature as described by four Teflon researchers.	77
Figure 5.2:	Specific heat relative to Teflon temperature as described by four Teflon researchers.	77
Figure 5.3:	Density relative to Teflon temperature as described by four Teflon researchers.	78
Figure 5.4:	A general diagram of the experimental Teflon ablation samples and Thermocouple location undertaken by <i>Clark</i> (1971). The diagram is not shown to scale.	80

Figure 5.5:	Thermocouple one response in <i>Clark</i> (1971) sample one. Experimental results are shown relative to simulated results for the range of material property values specified by <i>Clark</i>	81
Figure 5.6:	Thermocouple two response in <i>Clark</i> (1971) sample two. Experimental results are shown relative to simulated results for the range of material property values specified by <i>Clark</i>	81
Figure 5.7:	Thermocouple two response in <i>Clark</i> (1971) sample 16. Experimental results are shown relative to simulated results for the range of material property values specified by <i>Clark</i>	82
Figure 6.1:	Mass ablated per pulse as a function of the number of pulses fired for the four different heat flux scenarios. Experimental data is shown in order to compare general trends (<i>Spanjers, et al.</i> 1998)	86
Figure 6.2:	Temperature distribution within the PPT at different points in time during the firing sequence for the 2 microsecond heat flux case.....	86
Figure 6.3:	Thermocouple response at four locations within the 3 cm PPT during long-duration firing of the 2 microsecond constant heat flux case.	87
Figure 6.4:	Propellant consumption per pulse as a function of pre-pulse surface temperature for four different discharge durations and heat fluxes.	88
Figure 6.5:	Temperature distributions in the Teflon propellant after 3000 seconds of firing at different heat flux pulse durations denoted in the plot.	89
Figure 6.6:	Total energy required to ablate 20 micrograms of Teflon in the simulated XPPT-1 as a function of the applied heat flux duration.....	90
Figure 6.7:	Time required to completely re-crystallize the propellant domain after a pulse fired at a given residual propellant temperature. The four PPT discharge scenarios outlined in 6.1 are used.....	92
Figure 6.8:	Mass flux shown relative to heat flux during the discharge in the simplified 2 microsecond constant heat flux simulation.	93
Figure 6.9:	Mass flux shown relative to heat flux for a more realistic PPT situation. Scales are selected to show relative comparison between the two fluxes.	94
Figure 6.10:	Mass flux shown relative to heat flux for a rippled application profile. Scales are selected to show relative comparison between the two fluxes.	95
Figure 6.11:	Differences in simulated mass flux profile due to differences in assumed material properties in an XPPT-1 thruster using a critically damped heat flux profile.	97

List of Tables

Table 5.1: A detailed listing of Teflon material properties from four references shown relative to a more simplified listing from a fifth reference. The reference temperatures for each property are given in the Nomenclature section.....	76
Table 5.2: Three material property cases that encompass the range of values described by <i>Clark</i> (1971).....	79
Table 5.3: The conditions of three <i>Clark</i> (1971) experimental runs. These conditions are used in numerical simulation as well for comparison purposes.....	80

Nomenclature

<u>Symbol</u>	<u>Definition</u>
A	Melting material constant of integration
a	Transpiration cooling factor exponent
A_p	Depolymerization frequency factor
B	Melting material constant of integration
b	Temperature gradient near exposed surface
B_p	Depolymerization activation temperature (E/R)
C	Specific heat (general)
C_a	Specific heat of amorphous Teflon
$[C_a]$	Matrix of amorphous cell specific heat values
$C_{a(i)}^n$	Specific heat of amorphous Teflon in grid cell i at the current time step
C_c	Specific heat of crystalline Teflon
$[C_c]$	Matrix of crystalline cell specific heat values
$C_{c(i)}^n$	Specific heat of crystalline Teflon in grid cell i at the current time step
C_h	High temperature reference specific heat value as measured at T_h
C_{hs}	Specific heat of heat sink
C_{ma}	Specific heat of amorphous Teflon at the phase transition temperature (T_m)
C_{mc}	Specific heat of crystalline Teflon at the phase transition temperature (T_m)
C_r	Low temperature reference specific heat value as measured at T_r
C_s	Specific heat capacity of Teflon located at the exposed surface boundary
E	Teflon activation energy (3.473 MJ/Kg)
H_e	Enthalpy of outer convective boundary layer
H_m	Latent heat of crystal to amorphous phase transition (heat of fusion)
H_p	Teflon depolymerization energy per unit mass
$[H_p]$	Matrix of cell depolymerization energy values per unit mass

$H_{p(i)}^n$	Depolymerization energy per unit mass in grid cell i at the current time step.
H_{p0}	Base depolymerization energy per unit mass
H_{p1}	Depolymerization energy temperature coefficient
H_s	Enthalpy of the convective boundary layer at the exposed surface
h	Convective heat transfer coefficient
h_s	Enthalpy of surface material
$h_{-\infty}$	Enthalpy of material far from the exposed surface in a semi-infinite domain
i	Generic cell index value
ics	Index number of grid cell to the left of the exposed surface boundary
$icsm$	Index number of grid cell to the left of the phase transformation boundary
$iploc$	Index number of grid cell to the left of the virtual probe location
j	Generic cell index value in the transformed grid
k	Thermal conductivity (general)
k_a	Thermal conductivity of amorphous Teflon
$[k_a]$	Matrix of amorphous cell thermal conductivity values
$k_{a(i)}^n$	Thermal conductivity of amorphous Teflon in grid cell i at the current time step
k_B	Boltzmann constant (1.38×10^{-23} J/K)
k_c	Thermal conductivity of crystalline Teflon
$[k_c]$	Matrix of crystalline cell thermal conductivity values
$k_{c(i)}^n$	Thermal conductivity of crystalline Teflon in grid cell i at the current time step
k_h	High temperature reference thermal conductivity value as measured at T_h
k_{ma}	Thermal conductivity of amorphous Teflon at the phase transition temperature (T_m)
k_{mc}	Thermal conductivity of crystalline Teflon at the phase transition temperature (T_m)
k_r	Low temperature reference thermal conductivity as measured at T_r
k_{ref}	Reference thermal conductivity
k_s	Thermal conductivity of Teflon located at the exposed surface boundary
k_{wall}^n	Thermal conductivity of the heat sink boundary at the current time step
L	Starting Teflon domain length
\dot{m}	Mass flux from the exposed Teflon surface
\dot{m}^{n+1}	New mass flux value calculated at the current time step

m_m	Mass of Teflon monomer (1.66×10^{-25} Kg)
M_s	Molecular weight of species leaving the Teflon surface
M_∞	Molecular weight of free-stream plasma species
N	Transpiration cooling factor constant
$n_{gcounter}$	Heat flux time step counter
n_x	Number of grid points.
p	Grid transformation exponent
p_c	Teflon empirical vapor pressure constant (1.84×10^{15} Pa)
$p_{surface}$	Vapor pressure of Teflon at the exposed surface
p_{plasma}	Vapor pressure of plasma at the exposed surface
q	Incident heat flux at the exposed Teflon surface
q^n	Current heat flux value as read from the input file
q^{n+1}	Heat flux value at the new input interval as read from the input file
q_g	Generic heat flux term
Q_p	Depolymerization energy absorption
$Q_{p(i)}^n$	Depolymerization energy absorption in grid cell i at the current time step
R	Universal gas constant in monomer Teflon vapor (83.14 J/Kg/K)
s	Location of the exposed surface as measured from the rear PPT wall
s^n	Location of the exposed surface boundary at the current time step
s^{n+1}	New calculated location of the exposed surface at the current time step
s_m	Location of the phase transition plane as measured from rear PPT wall
s_m^n	Location of the phase transition plane at the current time step
s_m^{n+1}	New calculated location of the phase transition plane at the current time step
T	Temperature (general)
t	Time
t_{pulse}	Duration of applied heat flux
T_a	Temperature of amorphous Teflon
$[T_a]$	Matrix of amorphous cell temperatures
$T_{a(i)}^n$	Temperature of amorphous Teflon in grid cell i at the current time step

$T_{a(i)}^{n+1}$	New temperature of amorphous Teflon in grid cell i at current time step
T_c	Temperature of crystalline Teflon
$[T_c]$	Matrix of crystalline cell temperatures
$T_{c(i)}^n$	Temperature of crystalline Teflon in grid cell i at the current time step
$T_{c(i)}^{n+1}$	New temperature of crystalline Teflon in grid cell i at the current time step
T_h	High material property reference temperature (889 K)
T_{hs}	Heat sink temperature
T_{hsinit}	Initial heat sink temperature
T_{init}	Initial Teflon temperature
T_m	Teflon phase transformation temperature (600 K)
T_{ploc}^n	Temperature of the virtual thermocouple in the current time step
T_r	Low material property reference temperature (298 K)
T_s	Exposed surface temperature
T_{sub}	Empirical sublimation temperature exponent.
t_{ss}	Time required to reach steady-state ablation
T_{wall}	Temperature of the rear PPT wall (set equal to T_{hs})
T_{wall}^n	Temperature of the rear PPT wall at the current time step
T_{wall}^{n+1}	New temperature of the rear PPT wall at the current time step
v	Exposed surface recession velocity (ablation velocity)
v^{n+1}	New exposed surface recession velocity at the current time step
$V_{ga(i)}$	Percentage of cell i that is amorphous Teflon (amorphous volume fraction)
$V_{gc(i)}$	Percentage of cell i that is crystalline Teflon (crystalline volume fraction)
v_m	Phase transition plane velocity (melting velocity)
v_m^{n+1}	New phase transition plane velocity at the current time step
v_{ss}	Steady-state exposed surface ablation velocity
X	Melted material distance as measured from the exposed surface
x	Distance along Teflon domain measured from rear PPT wall
$x_{cnonuniform(j)}$	Center location of cell j in the transformed non-uniform grid
$x_{cuniform(i)}$	Center location of cell i in the uniform grid

$x_{nonuniform(j)}$	Right edge location of cell j in the transformed non-uniform grid
x_{ploc}	Location of the virtual thermocouple as measured from the rear PPT wall
$x_{uniform(i)}$	Right edge location of cell i in the uniform grid
$x_{c(i)}$	Center location of cell i
$x_{(i)}$	Right edge location of cell i

Greek Symbol Definition

α	Thermal diffusivity $(k/\rho/C)$
α_{ref}	Reference thermal diffusivity $(k_{ref}/\rho_{ref}/C_{ref})$
α_s	Surface thermal diffusivity $(k_s/\rho_s/C_s)$
β	Thermal conductivity temperature coefficient
δ	Thermal penetration depth
δ_{hs}	Heat sink thickness
Δt	Time step size
Δt_{max}	Maximum time step size allowed by numerical stability criteria
Δt_{qinput}	Heat flux input time step size
$\Delta x_{(i)}$	Width of cell i
ε	Teflon Emissivity (~ 0.92)
η	Transpiration cooling factor (convective blockage factor)
μ	Moving boundary analytical solution constant
v	Variable transformation of temperature
v_i	Transformed temperature at the initial conditions
v_s	Transformed temperature at the surface conditions
ρ	Density (general)
ρ_a	Density of amorphous Teflon
$[\rho_a]$	Matrix of amorphous cell density values
$\rho_{a(i)}^n$	Density of crystalline Teflon in grid cell i at the current time step
ρ_c	Density of crystalline Teflon

$[\rho_c]$	Matrix of crystalline cell density values
$\rho_{c(i)}^n$	Density of crystalline Teflon in grid cell i at the current time step
ρ_h	High temperature reference density as measured at T_h
ρ_{hs}	Heat sink density
ρ_r	Low temperature Teflon reference density
ρ_m	Mean density of crystalline Teflon and amorphous Teflon as measured at T_m
ρ_{ma}	Density of amorphous Teflon at the phase transition temperature (T_m)
ρ_{mc}	Density of crystalline Teflon at the phase transition temperature (T_m)
ρ_{ref}	Ablation reference density (set equal to ρ_r)
ρ_s	Density of Teflon located at the exposed surface boundary
σ	Stefan-Boltzmann constant ($5.67 \times 10^{-8} \text{ W/m}^2/\text{K}^4$)

Chapter 1

Introduction

Civilization today depends heavily on spacecraft and space systems for everything from communication to defense. Space systems require onboard propulsion for positioning, repositioning, attitude orientation, and control. Many different types of propulsion systems exist, but the most common are chemical thrusters. Chemical thrusters have many advantages because they can provide high torque and high impulse capability, but they generally suffer from low performance with measured specific impulse values not exceeding 400 seconds. Much higher performance with specific impulse values of 1000 seconds or more can be achieved by electric propulsion systems that utilize power from the spacecraft bus to assist in accelerating the expelled mass. Electric propulsion systems range in size and capability, but all use either electrostatic, electromagnetic, or electro-thermal means of accelerating the propellant.

A Pulsed Plasma Thruster is an electric propulsion device shown schematically in Figure 1.1. PPTs are similar in principle to other electric propulsion systems and consist of two electrodes arranged in such a configuration that an electric arc between the two from a capacitive discharge will create a magnetic field in a pattern that imparts a Lorenz force to the arc plasma (*Burton and Turchi*, 1998). In addition to the Lorenz force created due to the magnetic field and current interaction, gas-dynamic forces are also generally significant (*Spanjers, et al.*, 1998). These forces combine to accelerate the plasma and produce thrust. Pulsed Plasma Thrusters can be scaled to produce very small and precise amounts of momentum (impulse bits) and are generally used in situations requiring particularly fine attitude control (*Keidar et al.*, 2006). PPTs with both rectangular and coaxial electrode geometries are the most common and have been investigated since the 1960s because of their specific impulses in excess of 1000 seconds, low power requirements, simple propellant management, and the success of initial flight tests (*Burton and Turchi*, 1998). These include the recent successful flight of a MicroPPT aboard TechSAT.

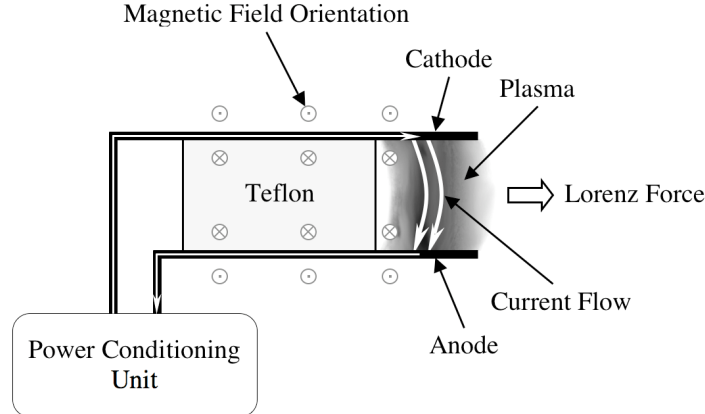


Figure 1.1: General schematic of the electrode and propellant arrangement in a solid fuel PPT.

Many types of fuel may be used in Pulsed Plasma Thrusters, but solid Teflon is one of the most attractive. An example of a solid fuel PPT with a coaxial electrode design is shown in Figure 1.2. Solid fuel is attractive because operational simplicity can be dramatically improved when valves and flow systems for liquid or gaseous propellants are eliminated (*Spanjers et al.*, 1998). Unlike steady-state liquid or solid fuel rocket engines, it is more difficult to compute the thrust and mass utilization in a solid fuel PPT due to the transient operational process shown in Figure 1.3. Nevertheless, it is known that the result of an arc discharge over the surface ablates and accelerates material containing primarily carbon and fluorine ions as well as a wide range larger molecules and some metal eroded from the electrodes (*Gatsonis, et al.* 2001). Various aspects of this complicated process have been the subject of significant research in the past forty years yet these continue to be relatively challenging topics. Consequently, a great deal of testing is still required to design new PPT configurations. Solid fuel PPTs are also not as efficient as theoretically possible (*Boyd*, 2006).

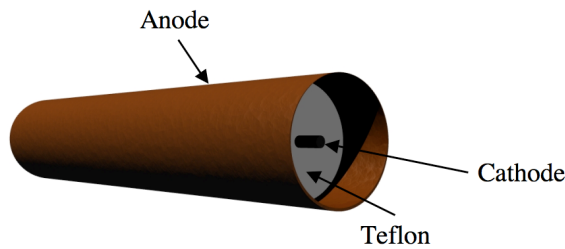


Figure 1.2: An example of a solid fuel PPT with a coaxial electrode configuration.

Given the expense of accurately testing PPTs to improve performance and control in either a simulated or real space environment, mathematical and numerical models are very popular among researchers investigating PPT characteristics. Numerical models also offer the potential of simplifying the design process. Unfortunately, the accuracy and scope of these models have, in the past, been limited

to simple one-dimensional or two-dimensional geometries with simple thruster operating procedures. These models also often incorporated significant simplifications in one or more of the physical processes taking place. The ablation process in particular is often subjected to considerable simplification. In fact, many modern computer simulations of PPT behavior still rely on empirical formulations of mass ablation and vaporization in spite of utilizing sophisticated Magneto-Hydro-Dynamic (MHD) models such as MACH2 to extensively account for the arc formation and plasma acceleration processes (also shown in Figure 1.3) (*Mikellides*, 1999).

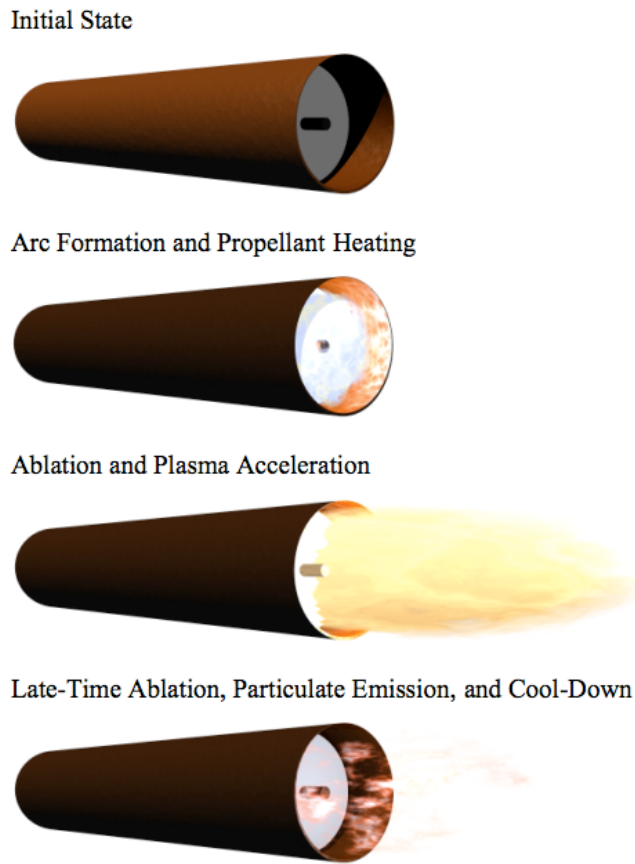


Figure 1.3: General operational sequence of a single pulse fired on a coaxial solid-fuel pulsed plasma thruster.

Because of the extensive simplifications in existing computational PPT models, this thesis focuses on the development and numerical implementation of a more accurate solid fuel ablation model for Pulsed Plasma Thrusters. This model is subsequently used to evaluate ablation and heat transfer trends observed in existing PPTs. Provisions are made for eventually coupling this model with existing high fidelity plasma flow models and with electro-mechanical models that approximate the entire PPT and plasma system as a simple dynamic electric circuit (*Laperriere, et. al.* 2005). This capability would

lead to a more comprehensive method of PPT performance evaluation and ultimately more efficient PPTs, more rapid PPT design and testing, and more precise spacecraft attitude control.

1.1 Teflon Ablation Overview

The ablation of the solid polymeric material is one of the general processes of interest in solid fuel PPTs and thermal protection systems and is one of the most difficult to simulate. Ablation generally occurs when a portion of the fuel surface is heated and removed by a short pulse of applied energy (*Burton and Turchi, 1998*). In the PPT, this applied energy originates from a high-current electric arc struck just above the surface. The radiant heat transfer from this arc and the conductive heat transfer from the associated plasma impart energy into the solid fuel medium. Polymeric fuels are usually used, so the coefficient of thermal conductivity is relatively low. As a result, the fuel surface will rapidly increase in temperature until some of the fuel becomes a vapor. This heat transfer process ultimately drives the ablation rate and subsequent mass removal. Because material ablation is important in many areas of engineering such as thermal protection systems and transpiration cooling methods, a great deal of research has been devoted to this process outside of the context of Pulsed Plasma Thrusters.

The ablation process is relatively straightforward in simple materials, but ablation of the polymeric materials used in Pulsed Plasma Thrusters is significantly more complicated. PTFE, also known as Polytetrafluoroethylene or by its more common name Teflon (*Clark, 1971*) is the most common material used in PPTs. “Teflon” is often used in reference to many types of fluoropolymer resins, but in this thesis applies primarily to crystalline PTFE. Teflon is generally used because it is inexpensive, easy to manufacture, difficult to char (carbonize), and remains relatively stable in the vacuum pressures encountered during spaceflight (*DuPont, 2004*). Unfortunately, the long-chain crystalline polymeric makeup that gives Teflon many of its advantages also means that the material undergoes both physical and chemical changes during heating and eventual vaporization. In general, the majority of research into Teflon ablation has focused on this process in the context of thermal protection systems such as spacecraft heat-shields or hypersonic vehicle nose cones. Nevertheless, this work has relevance to the ablation observed in Pulsed Plasma Thrusters.

One of the first investigations into the high temperature behavior of Teflon was performed by *Wentink (1959)* and identified the key properties and physical processes present in ablating Teflon. Teflon is essentially a white crystalline long-chain polymeric solid below 600K. An example of Crystalline Teflon is shown in Figure 1.4. Above 600K, the Teflon absorbs energy and changes into a mostly clear amorphous or gel-like phase. This phase transition is often described as “melting,” but the amorphous Teflon is still highly viscous (a viscosity of 10^{10} Kg/m/s confirmed by *Wentink (1959)* and

Clark (1971)) and is not considered a “liquid” by any standard. Due to this high viscosity, fluid modeling of Teflon ablation is unnecessary until the material has completely vaporized (*Clark*, 1971).

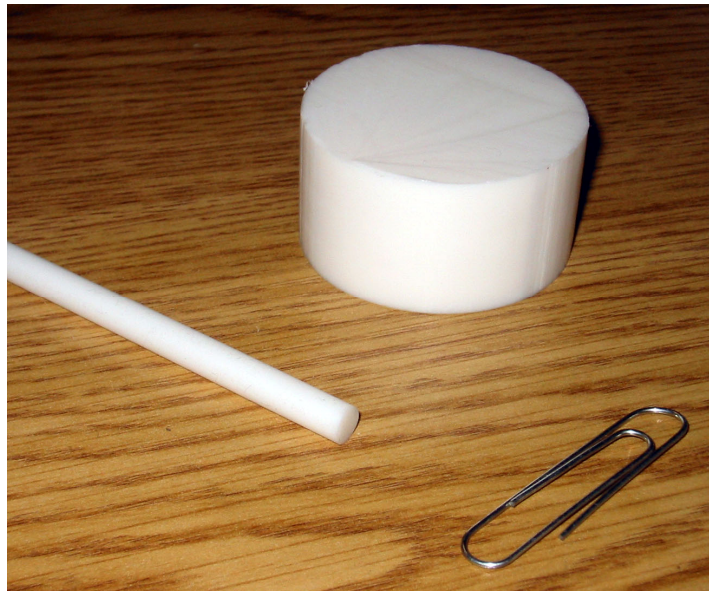


Figure 1.4: Two Examples of Crystalline Teflon shown relative to a paperclip.

Once Teflon has undergone this phase transformation, a further change takes place as the long chain Teflon polymers $(C_2F_4)_n$ shown in Figure 1.5 decompose. This process absorbs energy but does not take place at any specific temperature or energy threshold. Consequently, this decomposition occurs throughout the amorphous phase of the Teflon. The polymer decomposition was initially thought to take place by “unzipping” where carbon-carbon bonds were sequentially broken at the end of the polymer chains (*Wentink*, 1959). *Pope* (1975) pointed out that this was not completely correct, and that Teflon polymers depolymerize in a more random fashion. Regardless of the exact depolymerization method, the majority of the byproduct is the monomer C_2F_4 also shown in Figure 1.5 (*Wentink*, 1959). This monomer has a very high vapor pressure and consequently will break away from the surface as soon as it has been liberated from the longer molecule chain. The monomers are produced throughout the amorphous Teflon phase, but the majority are produced so close to the surface that it is assumed they leave the surface as soon as they have been liberated from the longer polymer chain (*Clark*, 1971). The Teflon material appears to simply sublime as a result of this process like many other materials. This description is not completely correct, however, because there is no specific boiling point and the large polymers themselves do not break free of the surface (*Wentink*, 1959). The fact that the long-chain polymers do not readily leave the surface translates into very low vapor pressures at crystalline temperatures and is one of the reasons Teflon is used in vacuum environments.

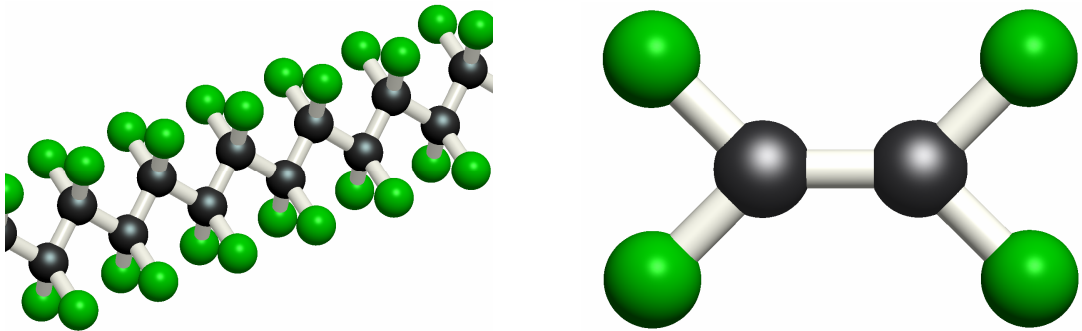


Figure 1.5: A Long Chain Teflon Polymer and a Teflon Monomer. Carbon atoms are black while Fluorine atoms are green. Bond angles are not exact.

From the general theory discussed above, the Teflon ablation process in a one-dimensional domain with transient heat flux can be schematically represented as shown in Figure 1.6. It should be noted that this schematic takes into account the fact that both the crystalline and amorphous (or gel) phases will expand when heated due to decreasing density.

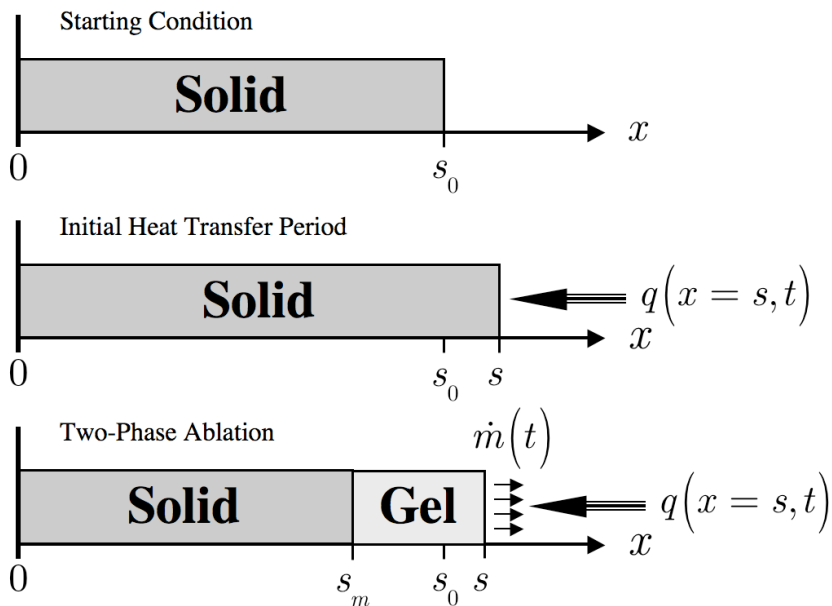


Figure 1.6: A general overview of the transient Teflon ablation process in a one-dimensional bar.

1.2 Review of Experimental Ablation Studies

An exact analytical solution of Teflon ablation is practically impossible to obtain because of the complexities ablation process described above (*Pope, 1975*). As a result, early ablation studies focused on experimental measurement often in the context of thermal protection systems for re-entering spacecraft or high speed atmospheric vehicles. *Vojvodich and Pope (1964)* performed an early general ablation

study in which several ablative and charring materials were subjected to different types of high temperature gas flows to determine if chemical reactions took place at the surface and the influence of these reactions on ablation and heating rates. They found that, while nitrogen and argon are generally inert in the vicinity of Teflon and thus produce predictable heat transfer characteristics, ablation in air is significantly more pronounced due to combustion effects. Consequently, the plasma species must be understood to completely evaluate the ablation process in convective types of environments.

Luikov, et al. (1968) performed a similar study specifically involving Teflon. In this study, several Teflon samples were subjected to high temperature gas flows similar to those used by *Vojvodich and Pope*. For the most part, these gas flows were chemically active, and the recorded data mainly focused on the differences in ablation rates between these types of flows. Studies by both *Wentink* (1959) and *Holzknecht* (1976) mentioned that data obtained from non-vacuum testing of Teflon ablation would not apply particularly well to vacuum ablation rates because of the way the different plasma species would react with the Teflon surface. For this reason, the experiments performed by *Luikov, Shashkov, and Yurevich* (1968) and *Vojvodich and Pope* (1964) did not have a significant impact on Teflon research with regard to vacuum applications.

A similar ablation experiment performed by *Clark* (1971) also subjected several Teflon samples to high temperature flows. Unlike *Luikov, Shashkov, and Yurevich* (1968), however, *Clark* was primarily interested in obtaining temperature data to correlate with early computer simulations and non-linear analysis of material properties. *Clark* also used argon to minimize thermo-chemical effects and he correlated observed temperature profiles with computed profiles from given sets of material properties. The net result was a complete dataset of high-temperature Teflon material properties including the associated error from the non-linear analysis. These material properties are still used because of their completeness and the inclusion of error analysis. Unfortunately, the error margins are fairly wide and other researchers have since developed properties that differ somewhat from those obtained by *Clark*. This illustrates that Teflon material properties are still not widely understood or agreed upon. Nevertheless, *Clark's* success in obtaining reasonably good agreement between his early numerical results and experimental data demonstrated the power of simulating ablation phenomenon.

Arai, et al. (1977) conducted experimental measurements of transient ablation on Teflon hemispheres in high heat flux, long-duration, convective conditions. The data obtained from these experiments indicated that thermal expansion significantly affected surface recession rates. It was not clear, however, if similar conclusions could be drawn for much shorter transient heating conditions because of the significantly reduced bulk material heating. *Arai* (1977) also observed that heat flow parallel to the surface could not be ignored in these convective environments. In other words, one-

dimensional models of ablation in convective conditions are generally inadequate due to the significantly changing flow characteristics at different points along the ablative material.

1.3 Review of Ablation Modeling

Given the difficulties and expenses associated with experimentally testing material ablation, a significant amount of research has focused on modeling the Teflon ablation process analytically and numerically. One of the most common ablation models treats Teflon as a sublimating solid (*Antonsen, et al.*, 2005). In this model, the mass flux per unit surface area is a simple function of the vapor pressure difference between the solid and the plasma, the Teflon surface temperature, the mass of each C_2F_4 vapor molecule, and the Boltzmann constant given by

$$\dot{m} \approx \frac{p_{surface} - p_{plasma}}{\sqrt{2\pi m_m k_B T_s}} \quad (1.1)$$

Generally the plasma pressure is relatively small compared to the Teflon surface vapor pressure and can be ignored (*Antonsen, et al.*, 2005). This reduces sublimation mass flux to a function of vapor pressure and surface temperature given by

$$\dot{m} \approx \frac{p_{surface}}{\sqrt{2\pi m_m k_B T_s}} \quad (1.2)$$

An additional simplification is made by expanding surface vapor pressure as a strict function of surface temperature and empirical constants p_c and T_{sub} as follows:

$$\dot{m} = \frac{p_c}{\sqrt{2\pi m_m k_B T_s}} \exp\left(-\frac{T_{sub}}{T_s}\right) \quad (1.3)$$

This model of Teflon mass flux is often used in numerical models that primarily focus on the plasma processes above the surface because it provides a boundary condition for the domain. However, this model does not represent a good method for further Teflon ablation research because it does not reflect the actual thermodynamic process Teflon undergoes when ablating. As previously mentioned, Teflon does not sublime as this model would suggest, but rather changes from a crystalline phase to an amorphous phase and subsequently decomposes into its C_2F_4 monomer constituents which escape from the surface (*Wentink*, 1959). Because of these differences, the more general vapor-pressure model would likely show erroneous results if used to determine mass flux in a range of operating conditions wider than previously tested (such as transient ablation).

Bespalov and Zalogin (1960) provided a more detailed mathematical derivation of the physical process to address the limitations of the vapor-pressure mass flux model. The *Bespalov and Zalogin* model focused primarily on steady-state boundary layer heat transfer when combined with ablation in convective environments. In this study, the heat transfer process was specified in terms of an energy balance at the ablation front given by

$$k \left(\frac{\partial T}{\partial x} \right) = \dot{m} (h_s - h_{-\infty}) \quad (1.4)$$

The mass flux from the surface was specified in terms of the Arrhenius reaction which is more appropriately suited to the kinetic polymer decomposition process and represented by

$$\dot{m} = \sqrt{\frac{A_p k \rho T_s^2 \exp(-E/RT_s)}{(h_s - h_{-\infty}) E}} \quad (1.5)$$

While this theoretical model was limited in scope, it provided a significant advance in Teflon ablation modeling by considering the decomposition in terms of the Arrhenius reaction law.

Kemp (1968) described the ablation process in a similar manner but avoided the theoretical aspects of atmospheric interaction to focus on the generic mass conservation, heat transfer, and ablation processes. *Kemp* was primarily interested in the total mass flux as well as the surface recession rate and simplified the relations by recognizing that, in general, ablation occurring through depolymerization mechanisms would be an extremely strong exponential function of temperature. By assuming a linear temperature gradient (b) near the surface and integrating the mass generated over this region with these simplified assumptions, *Kemp* obtained the following simple representation of the total mass flux:

$$\dot{m} = \sqrt{\frac{A_p \rho_s k_s T_s^2}{B_p (h_s - h_{-\infty})}} \exp\left(-\frac{B_p}{T}\right) \quad (1.6)$$

This relationship depended only on surface temperature, yet kept the depolymerization kinetic relationship. The ablated solid mass would equal the vapor mass in this case, so *Kemp* used the ablated mass value to solve for the ablation boundary velocity by

$$v = \sqrt{\frac{A_p k_s T_s^2}{B_p \rho_s (h_s - h_{-\infty})}} \exp\left(-\frac{B_p}{T}\right). \quad (1.7)$$

In addition to this basic mathematical ablation model, *Kemp* proposed a set of boundary conditions assuming a coordinate system fixed to the ablating boundary. Fixing a coordinate system in this way would create additional complexities in more dynamic transient ablation models, but it proved sufficient for steady-state ablation.

At this point, it should be noted that, while *Kemp* (1968) provided an early framework for more detailed modeling of the ablation and heat transfer process in Teflon, *Kemp* did not implement the model numerically. Instead, he made simplifying assumptions permitting him to achieve an analytical model similar to the vapor-pressure model but with a more accurate representation of the physical process. As a result, the ablation rates calculated using this method represent a good method of validating numerical ablation models that implement depolymerization kinetics. Still, several critical aspects of the physical process such as the Teflon phase transition prior to decomposition were left out of this analysis. In addition, several of the simplifying assumptions in this analytical representation (such as constant material properties or constant temperature gradients) were rather crude, especially in light of later work that demonstrated significant variability near the ablating surface *Clark* (1971).

The complete mathematical model of the ablation process was too difficult to solve analytically without significantly simplifications, so efforts turned to numerical simulation. *Clark* (1971), created one of the first ablation models specifically developed for numerical computation. Unlike previous simpler models, *Clark* factored in the Teflon phase transition at 600K. *Clark* also considered material properties (density, thermal conductivity, etc) to be linear functions of temperature and used non-linear estimation to determine some of these values (as discussed before). *Clark* divided his model into the two regions shown in Figure 1.7 to account for the discontinuities in material properties between each phase.

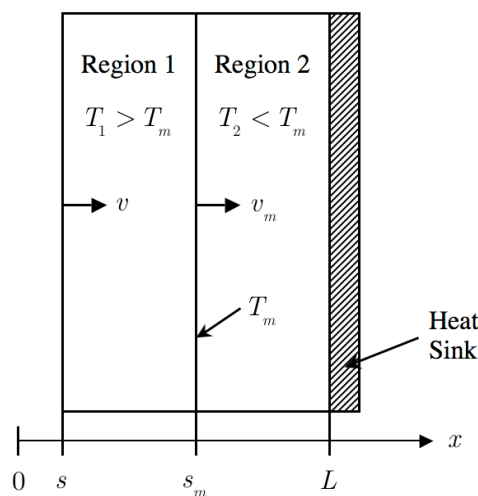


Figure 1.7: Ablation Regions as defined by *Clark* (1971)

In the schematic shown in Figure 1.7, Region 1 represents the amorphous Teflon ($T > 600\text{K}$), and Region 2 represents the crystalline Teflon ($T < 600\text{K}$). To compute the material temperature profile and mass flux, *Clark* defined the thermal response in both Regions 1 and 2 in terms of the one-dimensional Fourier equations. To compute the total energy flux absorbed by the decomposition process, *Clark* defined the decomposition rate in terms of the Arrhenius reaction law just as *Kemp* (1968) and *Bespakov and Zalomin* (1960) had done. It should be noted that while *Clark* (1971) initially specified the depolymerization and vaporization energy values as functions of temperature, results suggested the actual correlation was negligible and could be assumed to be constant if a simpler solution were desired (*Holzknecht*, 1976).

Clark computed the total material mass flux by integrating the decomposition rate between the ablating surface and the phase transition surface according to

$$\dot{m}(t) = A_p \int_s^{s_m} \rho_a(x, t) \exp\left(-\frac{B_p}{T_a(x, t)}\right) dx \quad (1.8)$$

Thermal expansion was neglected, so the surface recession velocity was specified as a simple function of the ablated mass flux and the initial material density given by

$$v(t) = \frac{\dot{m}(t)}{\rho_{ref}} \quad (1.9)$$

In addition to the mathematical description of the mass flux and surface recession processes, *Clark* provided detailed boundary conditions at the three computational boundaries: the ablation surface, phase transition interface, and far crystalline boundary (the heat sink). The most complex, the ablation surface boundary condition, took the form of a surface energy balance given by

$$-k_a \frac{\partial T_a}{\partial x} \Big|_s = q - \sigma \varepsilon T_s^4 - \dot{m} [\eta (H_e - H_s) - C_s T_s] \quad (1.10)$$

This energy balance related conduction into the exposed surface, the applied plasma flux (q) and the energy lost from the surface due to radiation and mass ejection. In this case, the boundary condition was based on the assumption that all the heat transfer to the surface came from a convective flow that was determined in the experimental analysis *Clark* later undertook for comparative purposes

Unlike *Kemp* (1968), *Clark* did not stop with simply deriving the model, but implemented it numerically using the FORTRAN computer programming language. This was a complex numerical problem, so *Clark* used a non-uniform morphing grid to fixed phase interface locations at specific grid

nodes. This introduced significant complexity but was necessary given the computational limitations at the time. This numerical implementation, combined with the experimental work, provided one of the most comprehensive and detailed models of Teflon ablation to date and aided in the development of detailed material properties mentioned earlier.

Pope (1975) followed the work of *Clark* and created a more simplified Teflon ablation model that described behavior in terms of boundary layer values that are more readily available in heat shield design. *Pope* used the simplified sublimation assumption to describe the ablation process. He included the heat of vaporization, the heat of fusion (phase change), and assumed the material was a single phase. These were significant simplifications but allowed the ablation model to be easily implemented numerically using the Chrysler Improved Numerical Differencing Analyzer on a CDC-6600 computer. The results of this simplified model were compared with experimental data from *Clark* (1971). Results were also compared with data from the NASA round robin ablation program. This program was focused primarily on obtaining experimental ablation data for a variety of materials in different atmospheric conditions. General trends matched reasonably well when inert gasses were used (10% error). However significant differences (40% or more) were observed when air was the convective transfer medium. Again, this was likely due to combustion effects that were not included in the model. Nevertheless, the results proved adequate for simplified heat-shield design at the time.

The use of numerical ablation models in heat shield design provided the driving force for two additional studies published by *Arai* (1976, 1979). These studies again focused on Teflon ablation in convective environments and again simplified the ablation process. In this case, however, a quadratic function was used to relate surface temperature to ablation rate. This was somewhat different from the sublimation assumption used by *Pope* (1975), but it was implemented for similar reasons. There were significant differences between the two models. *Arai* considered the full effects of both Teflon phases, which *Pope* neglected. *Arai* also used a two-dimensional geometry to better evaluate boundary layer effects on ablation. This would prove significant for aerodynamic ablation modeling when later experimental results verified the importance of tangential flow effects (*Arai, Karashima, and Sato*, 1977). The final *Arai* model was set up somewhat similar to the original model developed by *Clark* (1971) shown in Figure 1.7, except the outer exposed surface and the phase transition boundary were considered functions of both x and y . Using this two-dimensional ablation model, *Arai* demonstrated that the two-phase assumption was critical to accurately predicting temperature distributions and heat transfer characteristics in Teflon. *Arai* also demonstrated that increased surface temperature actually reduces gel layer thickness due to the increased recession rate of the outer surface. These results suggest that higher heat fluxes and the resulting faster ablation rates could reduce residual heating in the Teflon domain.

Following the two-dimensional ablation model that used simplified quadratic ablation assumptions, *Arai* (1979) proceeded to develop a more straightforward one-dimensional model which took into account the more accurate representation of the depolymerization kinetics as well as in-depth heating in radiative environments due to the optical transmittance of crystalline and amorphous Teflon. This model was consequently very similar to that developed by *Clark* (1971). The only significant difference between the two was the inclusion of volumetric radiative transfer relations in the heat conduction equation (Fourier's second law).

Arai used a coordinate transformation similar to that used by *Clark* to implement the one-dimensional ablation model numerically. This transformation fixed the ablation and phase transition boundaries at specific grid nodes but required modifications to the governing relationships. These modified equations were subsequently solved using an implicit finite difference method. It is interesting that *Arai* was able to resolve the stability challenges associated with implicit methods in moving boundary problems such as this. These stability challenges were noted by *Clark* (1971), who was unable to resolve them and resorted to a more consistently stable explicit technique. Once successfully implemented, however, *Arai* was able to determine that, while ablation in convective environments tends to reach steady-state operation fairly quickly, accounting for radiation effects draws this out. In addition, the in-depth radiative heating appeared to have significant impact on internal temperature distributions. *Arai* concluded from this that optical transmittance of Teflon cannot be neglected in intense radiative environments if an accurate representation of the ablation process is desired. It is not exactly clear how this conclusion relates specifically to PPTs since plasma conduction has been found to be the predominate mode of heat transfer in these devices (*Mikellides*, 1999).

Following the early work of *Clark* (1971), *Holzknecht* (1976) developed a very similar one-dimensional Teflon ablation model that took into account all ablation effects evaluated by *Clark*. In addition, *Holzknecht* included the effects of thermal expansion as well as the concept of higher-molecular weight compound formation in convective environments. The formation of higher molecular weight compounds occurs because at very high temperatures, not all of the monomer decomposition products are in monomer form. These radicals may subsequently react with other species in the local environment to form heavier compounds and affect the surface heat transfer. While this effect was found to be significant in high ambient pressure conditions, *Holzknecht* noted that the effect was minimal in low ambient pressure situations. The local atmospheric conditions are thus partially responsible for this effect.

While most of the effects considered by *Holzknecht* were described and implemented by *Clark* (1971), the additional effects described above required a somewhat different numerical implementation from those previously described. Thermal expansion effects resulted in material that was no longer stationary. Conservation of mass became a necessary solution condition, and all boundary coordinate

transformations had to take into account local material velocity. In addition, the mass flux from the surface and exposed surface location were no longer defined by depolymerization alone, but also by the limiting molecular weight fraction at the surface. This limiting function took the form of a piecewise function dependent on surface temperature and was computed from empirical mass ablation data. In spite of these complications, *Holzknecht* was able to implement the ablation model using an implicit finite difference method similar to that used later by *Arai* (1979). The temperature profiles obtained from this numerical implementation compared well with experimental profiles obtained by *Clark* (1971). It is interesting to note that this agreement was obtained using a set of material properties completely different from those specified by *Clark*. It is unclear why these material properties were selected over those used by *Clark*.

Following the work *Clark* (1971), *Holzknecht* (1976), and *Arai* (1976, 1979), several other solution approaches to the general ablation problem have been investigated. *Zien* (1978) developed an analytical approach for one-dimensional ablation situations with time-dependent heat flux. *Zien* developed this analytical technique by applying an integral solution to Landau's idealized ablation model. However, phase transformation, depolymerization, and material property variation were all neglected using this approach. In addition, only certain time-dependent heat flux functions were allowed. These restricted the usefulness of the analytical solution to a very narrow set of possible ablation problems none of which apply well to Pulsed Plasma Thrusters.

Chung and Hsiao (1985) considered the same basic problem with the same limited assumptions, but employed different solution techniques including a heat-balance integral method, a zero-moment integral method, and an implicit finite-difference numerical method. The solutions obtained for a given heat flux function with each method were compared in order to evaluate each technique. It was found that the zero-moment integral method provided better accuracy than the heat-balance integral method. However, both analytical techniques required the assumption of a semi-infinite solid and tended to under-predict ablation rates when finite slabs were considered. The numerical solution was superior both in terms of result accuracy as well as boundary condition flexibility to the analytical techniques in this case, but it still only considered a single-phase, non-depolymerizing material with constant properties.

Long after the initial experimental research into the behavior of Teflon ablation in chemically active flows for thermal protection system design, *Bhutta and Lewis* (1992) and *Milos and Rasky* (1994) developed numerical models for such conditions by taking into account surface thermochemistry. *Bhutta and Lewis* achieved this by using a coupled-chemistry Parabolized Navier-Stokes (PNS) scheme. This was solved using an implicit method and applied to a quasi-steady Teflon ablation model that factored in temperature dependence of specific heat and density. *Milos and Rasky* used approximate CFD methods and semi-analytical solutions to the same problem. These coupled-chemistry models proved significantly

more sophisticated than prior analytical or numerical work in this area, but were only applicable to highly-convective environments with reactive species such as oxygen. This was thus not particularly useful to Pulsed Plasma Thrusters.

The quasi-steady ablation model developed by *Bhutta and Lewis* was more applicable to PPTs than the surface thermochemistry model, but it was fundamentally simple in nature. This model simply evaluated mass flux from the surface based on the enthalpy difference between the boundary layer and the in-depth material as well as the heat flux values determined from the coupled-chemistry analysis. The specific heat and density variation were factored into the enthalpy relation along with lumped values for depolymerization energy and phase transition. No actual temperature variation within the Teflon domain was considered, and consequently all the effects dependent on this were neglected as well. Given the significance of two-phase effects and depolymerization temperature dependence, this ablation model suffered from many of the limitations associated with the analytical models. Nevertheless, the model results appeared reasonably accurate when compared with a few specific wind-tunnel shock-flow scenarios.

Following the early numerical model development with respect to aerodynamic ablation, two additional studies considered ablation in convective and reactive environments but included two-phase effects. The first study, conducted by *Wei and Zien* (2001), developed the integral relationships for aerodynamic ablation when two phases were present. The organization of this model was somewhat similar to that of *Clark* (1971), but the governing relationships and subsequent solution were significantly different since only an analytical result was desired. Nevertheless, this solution represented a fairly simple method of obtaining values of ablation performance in convective environments. *Wei and Zien* noted that the error associated with this method and its inherent assumptions limited this analytical technique to situations where only estimates or approximate ablation analysis was required. The numerical ablation model developed in a second study by *Shih et al.* (2003) avoided some of the limitations associated with an analytical model. This model used a similar set of assumptions and was implemented numerically by applying a Landau transformation and a finite volume method to the governing relationships for both phases. The model was subsequently validated against several simplified analytical ablation solutions and used to evaluate ablation behavior in two types of thermal protection materials (H41N and MXBE-350). Results from this analysis indicated that accurate prediction of the performance of these thermal protection materials in high heat flux environments depends significantly on accounting for two-phase effects especially with materials that have low heats of ablation. As important as this study was in continuing to establish the importance of two-phase effects in ablation, material property variations were neglected and it did not account for depolymerization concepts since the objective was not the specific analysis of Teflon. In spite of nearly 30 years time, the numerical models

developed by *Clark* (1971), *Holzknecht* (1976), and *Arai* (1976, 1979) still represent the most detailed analysis of Teflon to date.

Any numerical solution technique applied to an ablation problem is complicated by the fact that boundaries move and efforts to account for this movement must be undertaken regardless of the technique employed. Cell deformation or coordinate transformations are the most common, but volume fractions and interpolation may also be used. The former is more accurate and often used in ablation problems where boundary movement is usually limited. However, it requires significant modifications to the governing equations. The latter technique often produces more error, but doesn't require changes to the governing equations and is more useful in a wider range of two-phase problems where boundaries are often much more dynamic such as fluid modeling. Either technique can be applied to ablation problems regardless of whether finite-difference or finite-element techniques are used. Finite-difference methods are the most common used in ablation simulation, but the recent popularity of finite-element methods has led to a few ablation models with this solution approach.

Hogge and Gerrekens (1985) developed an early model to apply the finite-element method to ablation. This model used a deforming two-dimensional finite-element mesh to account for both changing domain size and temperature gradients. To implement this technique, an additional convective matrix was necessary at the element level to act on the temperature unknowns, and the heat penetration depth was evaluated to determine the extent of grid refinement near the exposed surface. The results of this technique demonstrated the sophistication of such a method. Very few cell elements were required to predict ablation behavior fairly well. *Hogan et al.* (1996) used a similar approach but in this case, the grid was deformed based only on domain size. No dependence of grid size on temperature gradients was considered. Still, the performance and flexibility of the finite element method in different two-dimensional situations was apparent. Unfortunately, both finite-element ablation models focused on more general thermal protection materials and thus didn't take into account the depolymerization kinetics of Teflon, two-phase behavior, or variable material properties. In addition, the heat-penetration-depth method of refinement used by *Hogge and Gerrekens* has limited application when long ablation or heat transfer time scales are considered because the depth reaches the rear of the domain and the grid can no longer be refined. It is also not clear how well the finite-element meshes employed in these studies would handle heat fluxes several orders of magnitude greater than those discussed. A solution would likely present little challenge and the flexible nature of finite-element methods make such options potentially desirable for future ablation studies.

1.4 Review of Experimental PPT Studies

Experimental studies specifically directed toward Pulsed Plasma Thrusters have generally focused on the reasons for propulsion inefficiency in addition to performance evaluation of specific designs such as the LES 8/9 (*Gatsonis, et al.*, 2001). As mentioned previously, PPTs (and solid fuel PPTs in particular) are not as efficient as theoretically possible. In fact, the majority of PPTs developed to date have efficiencies around 10% to 20% (*Boyd*, 2006). Propulsion inefficiency has been found to stem from two primary mechanisms: thermal energy loss and poor propellant utilization (*Spanjers et al.*, 1998). Thermal energy loss has been attributed to residual heating of the propellant (the propellant further inside the PPT that does not ablate during the pulse) as well as heat transfer out of the PPT by means of wall conduction and propellant radiation. In one particular study, *Bushman and Burton* (2001) found that energy lost through wall conduction accounted for over half of the energy that reached the PPT from the power conditioning circuitry. *Spanjers, et al.* (1998) also investigated the impact of residual heating on propellant temperature and found that this increased propellant temperature had an effect on propellant utilization during later pulses. Decreased residual propellant temperature appeared to provide more favorable performance through decreased propellant use for a given thrust level. It can be concluded from these studies that PPT discharges are coupled with one another to a certain extent. This is important because most theoretical PPT modeling has focused on isolated pulse simulation and evaluation.

In addition to the effects of residual heating, poor propellant utilization has also been attributed to propellant charring (carbon back-flux onto the Teflon surface), large particulate emission, and late-time material ablation (ablation following PPT firing that does not significantly contribute to thrust) (*Keidar, et al.* 2004, *Spanjers, et al.* 1998, *Antonsen, et al.* 2005). *Keidar et al.* (2004) found that charring could be minimized if sufficient energy per unit of ablation area is used in the discharge. On the other hand, if too much discharge energy is used, significant non-uniformities in the arc can cause much greater propellant loss (*Keidar et al.*, 2006). In general, it appears selection of discharge energy level has a significant impact on these loss mechanisms (*Keidar et al.*, 2006).

Particulate emission and late-time material ablation have proved difficult to avoid. In two specific cases studied by *Antonsen et al.* (2005) and *Spanjers et al.* (1998), these phenomena contributed $40\pm3\%$ and $23\pm11\%$ of the lost propellant mass respectively. Since magnetic acceleration occurs during the initial heating and current sheet expulsion, this late-time ablation does not significantly contribute to thrust. Particulate emission 100 μs following a pulse from XPPT-1 can be observed in Figure 1.8. The general ablation and plasma acceleration processes during the pulse are also shown for contrast.

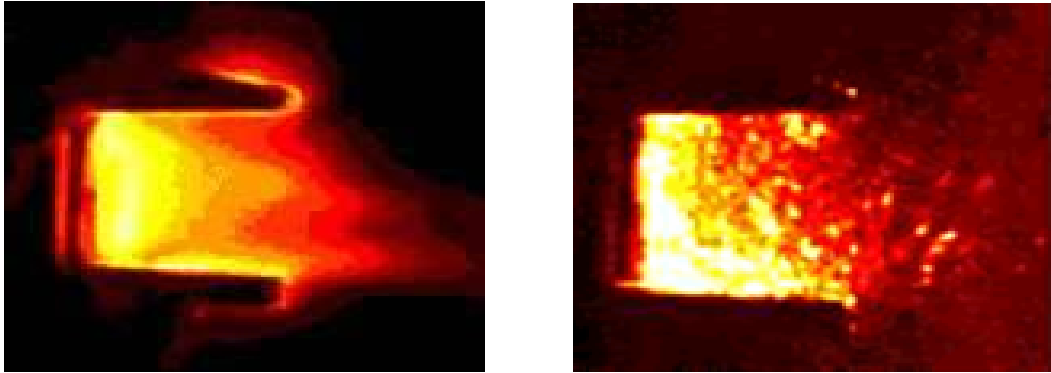


Figure 1.8: The XPPT-1 Pulsed Plasma Thruster during and immediately following a pulse. Particulate emission post-pulse is apparent (*Spanjers et al.*, 1998).

1.5 Review of PPT Modeling

A significant amount of research has investigated Teflon ablation, but other research has been exclusively devoted to modeling of PPTs. These models generally include the plasma processes and often allow comprehensive performance evaluation from PPT circuit parameters. *Michels, Heighway, and Johansen* (1966) developed an initial model directed toward coaxial capacitor-driven plasma guns rather than PPTs, but these are essentially the same devices. The model was analytical in nature but could approximate the performance and kinetic efficiency of PPTs based on mass loading distribution. This simplified model predicted that nearly 93% efficiency could be achieved if all mass to be accelerated was provided at the start of the current pulse. Unfortunately, solid fuel PPTs cannot function like this because the current used to accelerate the plasma also provides the energy for ablation. For less favorable mass flux profiles such as steady state, the model predicted that a minimum of 23% efficiency could be achieved. This efficiency value is still relatively high when compared to those of existing PPTs. *Michels, Heighway, and Johansen* noted, however, that the simplified model would tend to over-predict efficiency values across all mass profiles. It is therefore likely this early model actually provided fairly accurate representation of general PPT performance, given the fact that PPT mass flux profiles are usually far from optimal.

Turchi and Mikellides (1995) conducted later work in PPT modeling using the MACH2 two-dimensional magnetohydrodynamic (MHD) computer code coupled with an ablation subroutine. This ablation subroutine used the vapor-pressure model discussed earlier to compute mass flux based on surface temperature. While this vapor pressure assumption was not the best representation of the physical process, it did provide a more accurate boundary condition for the plasma interaction model than the previous practice of assuming a mass ablation profile based on limited experimental data. Results from this coupled model proved encouraging when compared with experimental results from the LES-6 PPT.

Additional work using the coupled MACH2 model was conducted by *Mikellides* (1999) to investigate whether PPT performance could be optimized based on modifying PPT current waveforms or electrode geometry. *Mikellides* found that, in general, the amount of material ablated from the surface was far greater than could be accelerated electromagnetically during the discharge. Current waveforms with short rise times and long decay times appeared to optimize thruster performance by minimizing this effect. *Mikellides* also found that coaxial PPT electrode geometries appeared to be less efficient than rectangular geometries and even better performance could be hypothetically obtained through the use of an “inverse pinch” electrode geometry that would provide more plasma expansion area. To the author’s knowledge, this type of electrode geometry has yet to be tested experimentally. Nevertheless, the results of *Mikellides* provide a interesting avenue for exploring improved thruster performance.

Following the extensive numerical work of *Turchi and Mikellides, Keidar, et al.* (2000) formulated a simple electromechanical model of the physical process present in coaxial PPTs during operation. The primary intent of the model was to provide upstream boundary conditions for particle and plume simulation models. For this reason, heat transfer to the Teflon was based largely on plasma parameters. These parameters were sufficient to approximate Teflon surface temperature, and this surface temperature was sufficient to obtain mass flux values through the use of the vapor-pressure sublimation model. Results from this model were in reasonable agreement with a limited set of experimental data. A similar study by *Keidar, et al.* (2001) and again by *Boyd* (2006) using the same ablation model found similar agreement. Unfortunately, the sublimation assumption still limited the model by providing an inaccurate representation of the physical process. The data obtained from this model also exhibited severe rate-of-change discontinuities in plasma temperature, plasma density, chemical composition, electron density, and Teflon temperature. These discontinuities were suspect because they were not explained, and similar discontinuities have not been observed in other computer models or experimental measurements. In addition, a maximum Teflon surface temperature of 650 K was reported which seems unrealistic, considering later experimental results obtained by *Keidar et al.* (2004) demonstrated surface temperatures above 1100 K. Nevertheless, the surface temperatures report by *Keidar, et al.* (2000) were generally in agreement with those found by *Mikellides* (1999), so it is likely the sublimation ablation model tends to under-predict Teflon surface temperatures relative to experimental results.

The ablation model developed by *Keidar, et al.* (2000) was later used by *Boyd, et al.* (2000) to provide the necessary boundary conditions for plasma plume modeling. This plume model coupled the original code with a two-dimensional plasma simulator using both “Particle-In-Cell” (PIC) as well as “Direct Simulation Monte Carlo” (DSMC) methods to describe the unsteady plume expansion process. The simulated behavior fit experimental observations fairly well early in the expansion, but differences were noted at later points in time. Nevertheless, results indicated that substantial differences exist in the

expansion behavior of the carbon ions, fluorine ions, and neutral species. *Gatsonis, et al.*, (2001) used a similar technique and included neutral-neutral, ion-neutral, and ion-electron collision effects. The results of this simulation were compared with substantial experimental data recorded using single-Langmuir probe, fast ionization gauge, and triple-Langmuir measurements from the LES-8/9 thruster. Ion speeds and trends similar to those noted by *Boyd, et al.* (2000) were replicated. In addition, *Gatsonis et al.*, (2001) noted that number densities in particular tended to drop more rapidly in simulation than in experiment at further distances from the Teflon surface. Neutral plume species were also found to continue expanding for up to one millisecond after the discharge. Analysis of the residual material in the vacuum chamber found mostly carbon and fluorine molecules of different chemistry though some copper from electrode erosion was also present. Further work by *Gatsonis and Yin* (2001) using the same model allowed prediction of backflow effects from discharge energy level – an important characteristic for spacecraft operation.

Plume studies allowed better characterization of spacecraft contamination and PPT operational issues, but they did not particularly influence ablation research. The opposite, however, was not true. All plume models require boundary conditions, and these originate from ablation behavior. This implies that ablation phenomenon, if better understood, could possibly provide additional insight into the plume characteristics and spacecraft contamination. More advanced ablation models could also be coupled with plume expansion models to allow better prediction of plume behavior particularly at later times and larger distances than is currently possible.

A technique for modeling PPTs developed by *Lin and Karniadakis* (2002) treated PPT firing (and specifically MicroPPT firing) as a single-fluid MHD flow where the ions and electrons carried different temperatures. This was coupled with an external power-conditioning circuit and a simplified ablation model to provide time-dependent boundary conditions for the plasma model. The objective of this modeling approach was to better resolve the viscous effects and other electro-dynamic and gas-dynamic behavior at the small scales characteristic of MicroPPTs (generally around one millimeter). *Lin and Karniadakis* also factored in the multi-species nature of the plasma originating from the Teflon surface since there is indeed wide variability in this area. One-dimensional simulation was first used in resolving these effects, but full three-dimensional MHD simulations were later implemented on structured as well as unstructured grids. *Lin and Karniadakis* found that viscosity does appear to affect PPT performance at these scales and they found a wide momentum distribution in the flow. They also found that the Knudsen number can be nearly an order of magnitude larger in MicroPPTs than in larger conventional PPTs. These effects were all primarily related to the fluid and plasma processes and did not appear to specifically depend on ablation. Nevertheless, the concept of using an ablation model to provide boundary conditions for extensive MHD simulation represents an important avenue to consider in

developing more comprehensive PPT models. *Lin and Karniadakis* also discussed the importance of addressing multiple length and time scales – an importance that carries over to the ablation processes.

A simplified PPT model presented by (*Laperriere, et al.*, 2005) approximated the PPT system as an electromechanical device. This assumed all processes could be computed from simple LCR circuit parameters. Several simplifications were necessary to derive this model including assumption of constant current sheet thickness, uniform current distribution per unit width, and constant plasma resistance. In reality, all of these parameters change during firing, but these simplifications provided an easy means of computing performance. Comparison of simulated results with experimental values measured from the LES-6 and LES-8/9 parallel-plate PPTs demonstrated that the simplified electromechanical model could predict circuit response, average plasma exit velocity, and specific impulse fairly well. This model was later used to evaluate the effects of applying a permanent magnetic field as a means of boosting PPT specific impulse in these particular thruster geometries. Results indicated that significant improvements were possible in high magnetic field fluxes. From a modeling standpoint, it was significant that a simplified model of this nature could predict performance so accurately. Nevertheless, it is not clear this success would apply to a much wider variety of situations and geometries where effects neglected by the model simplifications may be significant. MHD coupled ablation models tend to provide better means of evaluating more general situations since they take into account more aspects of the physical processes, however simplified models due have many advantages.

Most of the PPT models to date have focused on aspects related to performance or plasma processes, but a model developed by *Keidar, et al.* (2001) focused on simulating particulate emission. As discussed previously, large particles are generally given off by PPTs shortly after the pulse and contribute little to thrust. This model evaluated the effect of the residual PPT plasma on these particles and found that general charge and velocity conditions of the large particles observed during experimental analysis could be replicated numerically by assuming quasi-steady plasma conditions following the discharge. This assumption has very serious limitations considering the more realistic transient behavior following a PPT pulse. Consequently, this study did not offer any additional insight into the processes causing particulate formation that could lead to elimination of this phenomenon.

1.6 Objectives and Approach

Because of the simplifications assumed in the ablation behavior of existing computational PPT models, this thesis focuses on the construction and numerical implementation of a more accurate solid fuel Teflon ablation model specifically for Pulsed Plasma Thrusters and follows the general Teflon ablation research of *Clark* (1971), *Holzknecht* (1976), and *Arai* (1976, 1979). This model takes into

account all the major Teflon ablation effects considered important in PPT ablation environments and includes the following features:

1. One-Dimensional nature: One-dimensional ablation provides a fairly accurate representation of the physical process encountered in a PPT. While studies have shown 2D effects cannot be ignored in convective environments, heat transfer in PPTs has been found to be primarily conductive in nature and therefore these effects are likely fairly small and, if ignored, will not greatly impact the accuracy of the one-dimensional model (*Mikellides*, 1999).
2. Material property variation: Teflon material properties vary significantly between low temperatures and high temperatures and are discontinuous between phases. These variable properties are integrated into the model to provide a more accurate representation of the physical process.
3. Two-phase behavior: The phase transformation between a crystalline solid and an amorphous solid can significantly affect the temperature distribution in the material and is incorporated into the model. The melting and re-crystallization processes also absorb and give off heat, so these effects are taken into account.
4. Depolymerization: Teflon does not sublime but rather decomposes and this process is accurately represented throughout the amorphous phase.
5. Unsteady Heat input: Heat fluxes in PPTs vary widely during operation and this is implemented to accurately reflect the physical process.
6. Multiple physical and temporal scales: Ablation and heat transfer phenomenon in PPTs occur on scales characteristic of surface recession (nanometers and microseconds) as well as scales characteristic of entire devices in long-duration firing (centimeters and hours). Comprehensive investigation of ablation phenomenon requires analysis on these different scales, so the numerical implementation is designed to allow this flexibility.
7. Multiple stages: Teflon does not necessarily behave the same way in all temperature regimes, and this effect must be considered by providing sub-models for each stage of thermal and ablation response.

The features allow fairly comprehensive analysis of Teflon ablation behavior. Nevertheless, certain aspects of ablation behavior are neglected:

1. Thermal expansion: Thermal expansion effects are important in long-duration convective ablation situations, but it is not clear these effects are important in Pulsed Plasma Thrusters due to

the very small region of significant heating. Inclusion of thermal expansion effects would also somewhat compromise the desire for an extensible numerical implementation.

2. In-depth radiative absorption: In-depth radiation effects and optical properties are important in intense radiation environments. However, it has been found that the majority of heat transfer in PPTs results from plasma conduction (*Mikellides*, 1999). This effect is consequently ignored although future work might include these effects since some amount of radiative heat transfer will be present in PPTs.
3. Formation of higher molecular weight compounds: Higher molecular weight compounds constitute a significant percentage of the ejected mass in high temperature convective ablation conditions, but are only found outside the ablation layer in the convective boundary layer. Since convection is not the primary method of heat transfer in PPTs, it is unclear if a similar effect exists or if it has any significant impact on ablation. Consequently, this effect is neglected.

In addition to the scalable features of the ablation model, it is desirable to provide for the detailed two-phase behavior without requiring coordinate transformations. This will allow for a flexible numerical implementation that can be easily expanded in the future to account for other effects or additional dimensions. Provisions should also be made for eventually coupling the ablation model with existing high-fidelity plasma flow models or simpler electro-mechanical plasma/circuit models to develop a more comprehensive method of PPT performance evaluation. These aspects all require a model developed and implemented in the most flexible and modular method possible. The model creation and the ablation research process are broken down into the following steps:

1. Mathematical Model Development. The model is divided into three stages corresponding to pre-ablation heat transfer, heat-transfer with an initial melt layer, and two-phase heat transfer with ablation. The theoretical and mathematical formulations of the governing equations are established in each stage of operation. Stage one develops relationships for transient heat conduction in one phase materials as well as heat sink and unsteady heat flux boundary conditions. Stage two is similar but establishes an exposed surface boundary condition for the melting material. Stage three develops relationships for transient heat conduction in two-phase materials, depolymerization energy absorption, depolymerization mass flux, phase-interface boundary movement, and exposed surface recession. Relationships for variable material properties in all three stages are also established.
2. Numerical Implementation. The propellant domain is discretized numerically using either uniform or non-uniform grids that can be coarsened or refined during simulation. Node locations

are based on domain size, node quantity, and an algebraic mapping function (in the case of the non-uniform grid). Volume fractions are developed to allow phase interface and ablation boundary movement without grid transformations. The governing mathematical relationships are subsequently discretized using standard explicit finite difference techniques, and numerical stability using these techniques is analyzed. Additional numerical relationships are defined to allow straightforward unsteady heat flux input and virtual temperature probe analysis. Finally, an example ablation scenario is used to demonstrate the capabilities of the model.

3. Model Validation. Six heat transfer and ablation scenarios with analytical or prior numerical solutions are used to validate each aspect of the ablation model. These include validation of heat conduction, heat flux boundary conditions, heat sink boundary conditions, material property variation, phase interface boundary movement, ablation mass flux, and ablation surface recession. The solutions used in validating these physical aspects are derived in each case. Additionally, a seventh scenario is used to analyze error associated with the adaptive grid technique.
4. Material Property Analysis. Discussion of high-temperature Teflon material properties is presented and uncertainty in these values is established. The numerical ablation model is used to evaluate the impact of this uncertainty on thermal performance and ablation behavior in three general scenarios corresponding to experimental ablation samples tested by *Clark* (1971). The results of this analysis are used for formulate general statements about the effects of material property uncertainty on thermo-physical behavior.
5. PPT Analysis. The numerical ablation model is used to evaluate trends associated with long duration pulsing in PPTs including the effects on propellant consumption and residual heating. Several heat flux scenarios corresponding to conditions encountered in the XPPT-1 thruster are created for this purpose. The results of this analysis are compared with experimental XPPT-1 thruster results to formulate conclusions pertaining to long-term ablation effects. In addition, late-time ablation is evaluated in the context of variable heat flux, amorphous layer re-crystallization is evaluated in the context of particulate emission, and material property uncertainty is evaluated in the context of PPT ablation rates. General conclusions from these results are established.

The numerical ablation model also provides a unique tool for evaluating new thruster designs before experimental testing is required. It is hoped that thruster operation, efficiency, and propellant utilization for a given geometry and power input level can eventually be optimized through numerical simulation such as those presented in this work. This can ultimately lead to more rapid PPT design and testing, greater propulsive efficiency, and cheaper spacecraft attitude control systems.

Chapter 2

One Dimensional Mathematical Model

In order to simplify the ablation modeling process, the mathematical model implemented by *Clark* (1971) was chosen as a starting point. The ablation model was subsequently broken into three stages representing the different ablation behaviors that would occur during PPT operation. These three types of behavior were described respectively as heat transfer within purely crystalline Teflon, heat transfer during the initial formation of the amorphous phase, and complete ablation processes with two phases present. *Clark*'s mathematical model was chosen because it considered the phase transformation, depolymerization kinetics, and changing material properties. This provided a significantly more complete description of the ablation process with fewer considerations than many current Teflon ablation models. It also provided ample experimental data and material property analysis for future comparison and validation if necessary. While *Clark*'s mathematical model did not include thermal expansion effects, the formation of higher-order molecular weight products, or in-depth radiation effects as considered by later authors (*Holzknecht* and *Arai*), the author felt that including these effects would significantly compromise the goal of a simple and extensible code architecture with little added benefit. *Clark* was also able to obtain fairly reasonable results without considering these additional aspects of the problem, so they were neglected in this analysis.

2.1 Initial Conditions

The initial model conditions are straightforward and simply specify the initial Teflon material temperature and wall temperature. The rear surface of the one-dimensional bar is located at $x = 0$ while the exposed surface (s) is located at $x = L$. Initial crystalline material density (ρ_c), specific heat (C_c), and thermal conductivity (k_c) are functions of the initial temperature and are uniform throughout the bar. The only limitations on the initial temperature and wall temperature selection are that they be below the Teflon phase transition temperature (600K). A graphical representation of the problem domain with these initial conditions is shown in Figure 2.1.

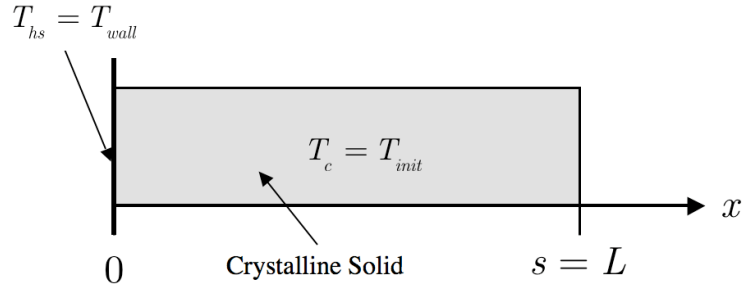


Figure 2.1: Initial Conditions for Mathematical Model

2.2 First Ablation Stage

The first model stage describes the simple heat conduction process throughout the crystalline Teflon bar due to an applied heat flux at the exposed surface. This process is modeled by solving the conservation of energy equation given by

$$\rho_e C_e \frac{\partial T_c}{\partial t} = \frac{\partial}{\partial x} \left(k_e \frac{\partial T_c}{\partial x} \right) \quad (2.1)$$

Stage one of the model is completed by applying a heat sink boundary condition at the inner surface ($x = 0$) where the heat sink has a density (ρ_{hs}), specific heat, (C_{hs}) and thickness (δ_{hs}) that are all independent of time. The effective heat sink thickness is shown in Figure 2.2. Thermal conductivity within the heat sink is assumed to be very high such that temperature variations within the heat sink itself can be neglected. These assumptions lead to

$$-k_e \frac{\partial T_c}{\partial x} = \rho_{hs} C_{hs} \delta_{hs} \frac{\partial T_{hs}}{\partial t} \quad (2.2)$$

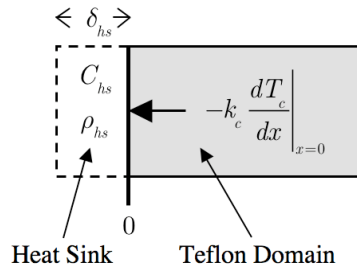


Figure 2.2: Graphical depiction of the effective heat sink simulated by the heat sink boundary condition.

In addition to the heat sink boundary condition, a heat flux boundary condition is also applied at the outer exposed surface ($x = s$) by

$$-k_c \frac{\partial T_c}{\partial x} \Big|_{x=s} = q - \sigma \varepsilon T_s^4 \quad (2.3)$$

It should be noted that while *Clark* implemented a similar heat sink boundary condition at the rear wall, he used slightly different notation where the heat sink density, specific heat capacity, and thickness were merged into a single “thermal mass” value. To allow greater flexibility, the heat sink properties in this model are defined in terms of physical heat sink properties using the method described by *Arai* (even though the evaluated results would remain the same). The exposed surface boundary condition, on the other hand, is taken directly from the work of *Clark* in which the conduction into the material is computed from an applied heat flux (q) with provisions for energy loss due to surface radiation. A graphical representation of these boundary conditions applied to the Teflon domain is shown in Figure 2.3.

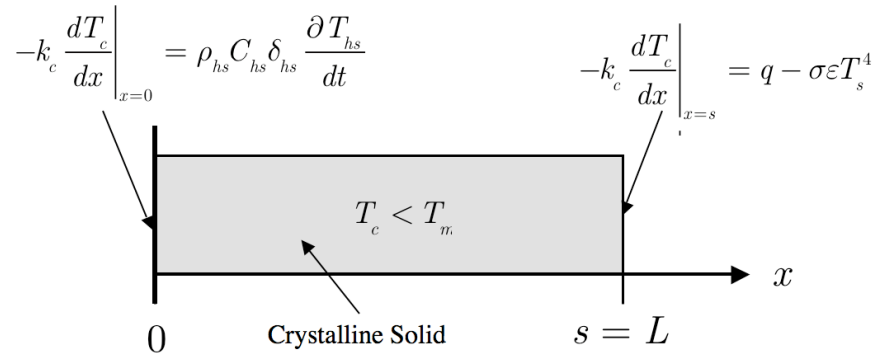


Figure 2.3: Stage One Boundary Conditions

The temperatures throughout the Teflon in this stage of the model are limited to less than the phase transition temperature ($T_m = 600K$). When the temperature of the exposed surface (the point of highest temperature) reaches the phase transition temperature, the model switches to stage two operating principles.

2.3 Second Ablation Stage

The second model stage describes the same process as stage one, except the boundary condition at the exposed surface is set to the phase transition temperature ($T_s = T_m$). Aside from the altered boundary condition, all other aspects of stage two operating behavior are the same. This minor adjustment to stage one behavior is implemented as an independent stage to ease the transition to later

operating behavior (since such a transition would generally only occur at one point in time during operation). Once the melt plane begins to recede into the material in this stage, the model switches to stage three operating principles. A graphical representation of the stage two boundary conditions is shown in Figure 2.4.

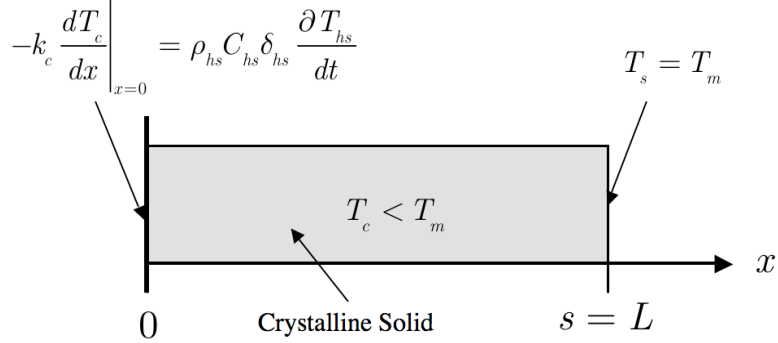


Figure 2.4: Stage Two Boundary Conditions

2.4 Third Ablation Stage

The third ablation stage describes the ablation and heat conduction process once the exposed Teflon surface temperature exceeds the phase transition temperature. This stage is significantly more complex than the two previous stages and accounts for all major ablation effects as well as the multiple Teflon phases. To account for these different aspects mathematically, the Teflon bar is divided into two sections corresponding to each phase. The crystalline phase is modeled in much the same way as in the previous stages. Conservation of energy is first applied throughout the domain by

$$\rho_c C_c \frac{\partial T_c}{\partial t} = \frac{\partial}{\partial x} \left(k_c \frac{\partial T_c}{\partial x} \right) \quad (2.4)$$

Next, the heat sink condition is applied at the rear ($x = 0$) boundary as before:

$$-k_c \frac{\partial T_c}{\partial x} = \rho_{hs} C_{hs} \delta_{hs} \frac{\partial T_{hs}}{\partial t} \quad (2.5)$$

Finally, the forward ($x = s$) boundary condition can be applied. In this case, the forward boundary of the crystalline stage is not located at the exposed surface but is instead located at the phase transition interface ($x = s_m$) where the temperature is fixed at the phase transition temperature by

$$T_c(x = s_m) = T_m \quad (2.6)$$

The amorphous phase is modeled by solving the conservation of energy equation as in the crystalline phase except the amorphous phase properties and temperatures are used in place of their crystalline values. In addition, the energy absorbed by the decomposing polymer in the amorphous phase (Q_p) is factored into the conservation of energy relationship to give

$$\rho_a C_a \frac{\partial T_a}{\partial t} = \frac{\partial}{\partial x} \left(k_a \frac{\partial T_a}{\partial x} \right) + Q_p \quad (2.7)$$

Since depolymerization is a chemical reaction, this energy absorption takes the form of the Arrhenius equation denoted by

$$Q_p = -A_p \rho_a H_p(T_a) \exp \left(-\frac{B_p}{T_a} \right) \quad (2.8)$$

The Arrhenius equation accounts for the statistical distribution of energy present at any given temperature within the material and its corresponding effects on the rate of reaction. This approach is historically significant because it was used successfully by *Clark, Arai, Bespalov and Zalogin, Holzknecht*, and many other researchers investigating the high temperature behavior of polymeric materials. It is also frequently used in analysis of other chemical reaction rates as well as molecular diffusion.

The first boundary condition in the amorphous phase is specified by the constant phase transition temperature at the phase interface (s_m) given by

$$T_a(x = s_m) = T_m \quad (2.9)$$

The second boundary condition in the amorphous phase is specified by the net heat flux into the material at the exposed surface (located at $x = s$). This condition takes into account the incident heat flux, the losses due to radiation, and the energy lost in the ablated material itself to give

$$-k_a \frac{\partial T_a}{\partial x} \Big|_{x=s} = q - \sigma \varepsilon T_s^4 - \dot{m} C_s T_s \quad (2.10)$$

For situations where the primary mode of heat transfer is through convection, the ablation process blocks a certain amount of the incoming heat flux because of interaction between the incoming and outgoing mass within the boundary layer. This is factored into the boundary condition through the use of a blockage factor (η) sometimes referred to as the transpiration cooling factor, and the enthalpy values of the incoming hot gas both outside the boundary layer (H_e) and at the Teflon surface (H_s). The boundary

layer enthalpy values are not evaluated in further detail because they generally depend on many other parameters outside the scope of this research. Nevertheless, the boundary condition modified for a convective case is given by

$$-k_a \frac{\partial T_a}{\partial x} \Big|_{x=s} = q - \sigma \varepsilon T_s^4 - \dot{m} [\eta (H_e - H_s) - C_s T_s] \quad (2.11)$$

The transpiration cooling factor is generally considered a function of the molecular weight ratios between the incoming and outgoing gases (or plasmas). This relationship is derived by *Pope* (1975) as

$$\eta = N \left(\frac{M_\infty}{M_s} \right)^a \quad (2.12)$$

The empirical constant and exponent used in finding the transpiration cooling factor usually fall within the ranges

$$\begin{aligned} 0.67 &\leq N \leq 0.72 \\ 0.25 &\leq a \leq 0.4 \end{aligned} \quad (2.13)$$

Graphical representations of the convective and non-convective boundary conditions applicable at the outer surface are shown in Figure 2.5.

The convective boundary condition is not particularly applicable to PPTs since very little convective heat transfer exists in these devices. It is nevertheless provided here because it is applicable in many other types of situations such as ablation analysis of thermal protection systems. Unfortunately, energy generation due to chemical reactions within the convective boundary layer are considered outside the scope of this research and are neglected with this approach. If high density oxidizing species of gas are used as the convective heat transfer medium, such reactions would occur and could significantly affect heat transfer to the Teflon surface (*Clark*, 1971). In these cases, the inclusion of a combustion boundary layer model would be necessary to properly account for these effects.

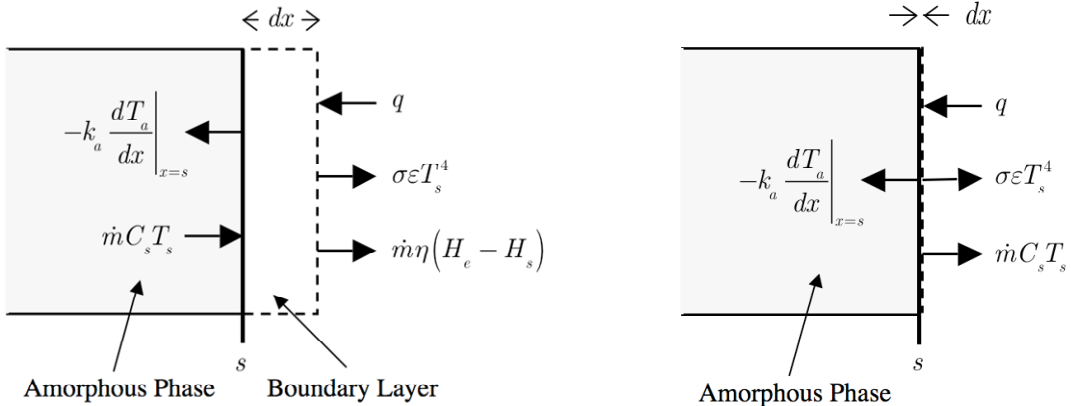


Figure 2.5: Detailed Representations of the different outer boundary components for the convective case in stage three operation (left) and the non-convective case in stage three operation (right).

In addition to the heat conduction characteristics, the phase interface boundary and exposed surface boundary move in this portion of PPT operation. The velocity (v_m) of the phase interface boundary (s_m) is given as a function of the heat conduction between the phases at the interface, the required heat of fusion (H_m), and the mean density (ρ_m) by

$$v_m = \frac{1}{\rho_m H_m} \left[k_{mc} \frac{dT_c}{dx} \Big|_{s_m} - k_{ma} \frac{dT_a}{dx} \Big|_{s_m} \right] \quad (2.14)$$

This velocity provides the position of the phase interface boundary over time when integrated by

$$s_m = \int v_m dt \quad (2.15)$$

The recession rate (v) of the exposed surface depends on the mass flux from the outer surface (\dot{m}) and the reference density (ρ_{ref}) by

$$v = -\frac{\dot{m}}{\rho_{ref}} \quad (2.16)$$

The reference density in this case represents the initial Teflon density prior to heating. This is used instead of the actual Teflon density at the exposed surface (ρ_s) because the actual density would give erroneous recession velocities in situations where thermal expansion is neglected (Clark, 1971). While actual surface density and reference density values may be significantly different in cases with very hot surface temperatures, this method still provides accurate boundary location information. The mass flux

used to derive surface recession is found by integrating the depolymerization rate over the entire amorphous domain by

$$\dot{m} = A_p \int_{s_m}^s \rho_a \exp\left(-\frac{B_p}{T_a}\right) dx \quad (2.17)$$

The position of the exposed surface is computed from the exposed surface recession rate in a similar manner to the phase interface position as follows:

$$s = \int v dt \quad (2.18)$$

Graphical representations of the surface locations and boundary conditions used in stage three analyses are shown in Figure 2.6 and Figure 2.7 for the convective and non-convective cases. The boundary layer depiction shown initially in Figure 2.5 for the convective case is not repeated in this graphical representation. These relations conclude the basic one-dimensional model. It should be noted that, while Teflon vapor mainly escapes from the surface (diffusion through the material has little effect), integrating the depolymerization reaction over the entire amorphous domain is still a fairly accurate method of determining mass flux due to the exponential dependence of the decomposition on temperature (Clark, 1971). The vast majority of material decomposition takes place within an extremely short distance of the surface, and it leaves the domain nearly immediately upon decomposition with few other effects.

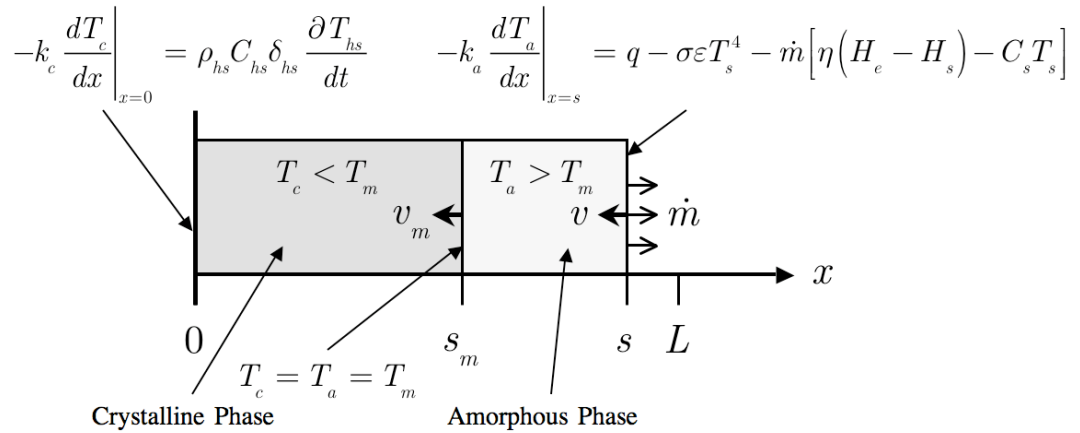


Figure 2.6: Stage Three Boundary Conditions and material phases for the convective case.

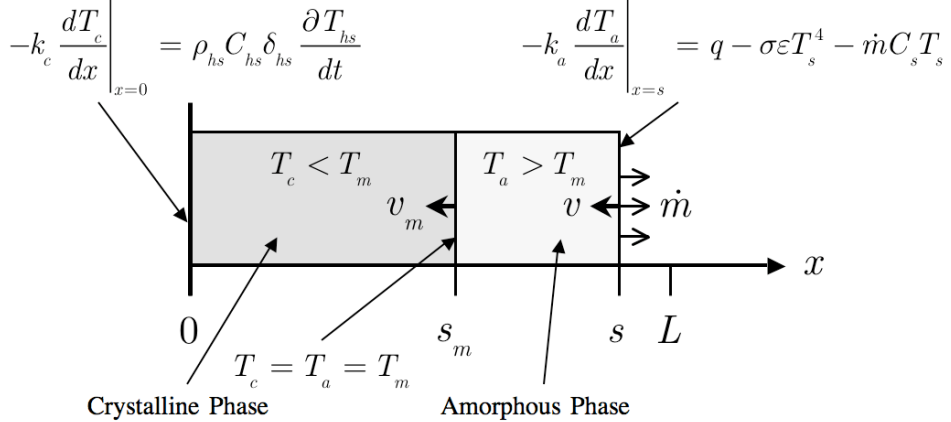


Figure 2.7: Stage Three Boundary Conditions and material phases for the non-convective (PPT) case.

2.5 Material Properties

The mathematics outlined in the previous portions of Chapter Two describe the majority of the ablation process, but that process depends on material properties. Unlike many past ablation models, this model does not make the assumption that material properties remain constant. To simplify normally complex material property relationships, several basic material properties including density, specific heat capacity, and thermal conductivity are considered linear functions of temperature within each respective phase (crystalline and amorphous). These material property functions are based on those originally provided by *Clark* (1971) and are computed from two measured reference properties at two reference temperature within each phase as follows:

$$\rho_c(T_c) = \rho_r + \left(\frac{\rho_{mc} - \rho_r}{T_m - T_r} \right) (T_c - T_r) \quad (2.19)$$

$$\rho_a(T_a) = \rho_h + \left(\frac{\rho_h - \rho_{ma}}{T_h - T_m} \right) (T_a - T_m) \quad (2.20)$$

$$C_c(T_c) = C_r + \left(\frac{C_{mc} - C_r}{T_m - T_r} \right) (T_c - T_r) \quad (2.21)$$

$$C_a(T_a) = C_h + \left(\frac{C_h - C_{ma}}{T_h - T_m} \right) (T_a - T_m) \quad (2.22)$$

$$k_c(T_c) = k_r + \left(\frac{k_{mc} - k_r}{T_m - T_r} \right) (T_c - T_r) \quad (2.23)$$

$$k_a(T_a) = k_h + \left(\frac{k_h - k_{ma}}{T_h - T_m} \right) (T_a - T_m) \quad (2.24)$$

Depolymerization energy is also considered a linear function of temperature within the amorphous phase by

$$H_p(T_a) = H_{p0} - H_{p1}T_a \quad (2.25)$$

While several more sophisticated quadratic representations of these material properties were later provided by *Holtzknecht* (1976), *Clark* provides one of the most comprehensive sets of Teflon material properties. Therefore, this approach appears to provide the greatest benefit while still retaining flexibility for future additions or changes in material property functions. A more detailed analysis of material properties is provided in Chapter Five.

Chapter 3

One Dimensional Numerical Implementation

The one-dimensional mathematical model outlined in Chapter Two describing Teflon ablation has been implemented utilizing the FORTRAN-95 computer programming language on high performance digital computers. Initial interest was focused on following the work of *Clark* (1971), however significant improvements and simplifications were possible because of the vastly superior computational tools available. The simplifications allowed a more modular implementation of the mathematics. Nevertheless, the large range of heat fluxes, domain scales, and time scales encountered when simulating PPT behavior still required a flexible and sophisticated grid architecture to minimize computational time.

3.1 General Execution Sequence and Logic

An execution structure is necessary to approach the ablation problem from a programming standpoint. This structure takes into account all aspects of the problem and solution process to compute the necessary parameters at the proper time in the execution procedure. In the case of the ablation problem under investigation, the execution logic is divided into two steps. These two steps and a general representation of the execution sequence are shown in Figure 3.1. A more detailed representation of the execution structure is provided in Appendix A.

The first step of code execution consists of array and variable definitions, data input, and problem initialization. Array and variable definitions are implemented by a single module to ensure variable consistency and effortless data-passing between all later subroutines. Data input consists of reading in problem-specific variables from one file, material property reference values from a second file, and an initial heat flux value from a third input file. Problem initialization consists of setting all arrays and variables to the initial conditions as well as setting up the grid architecture (discussed later).

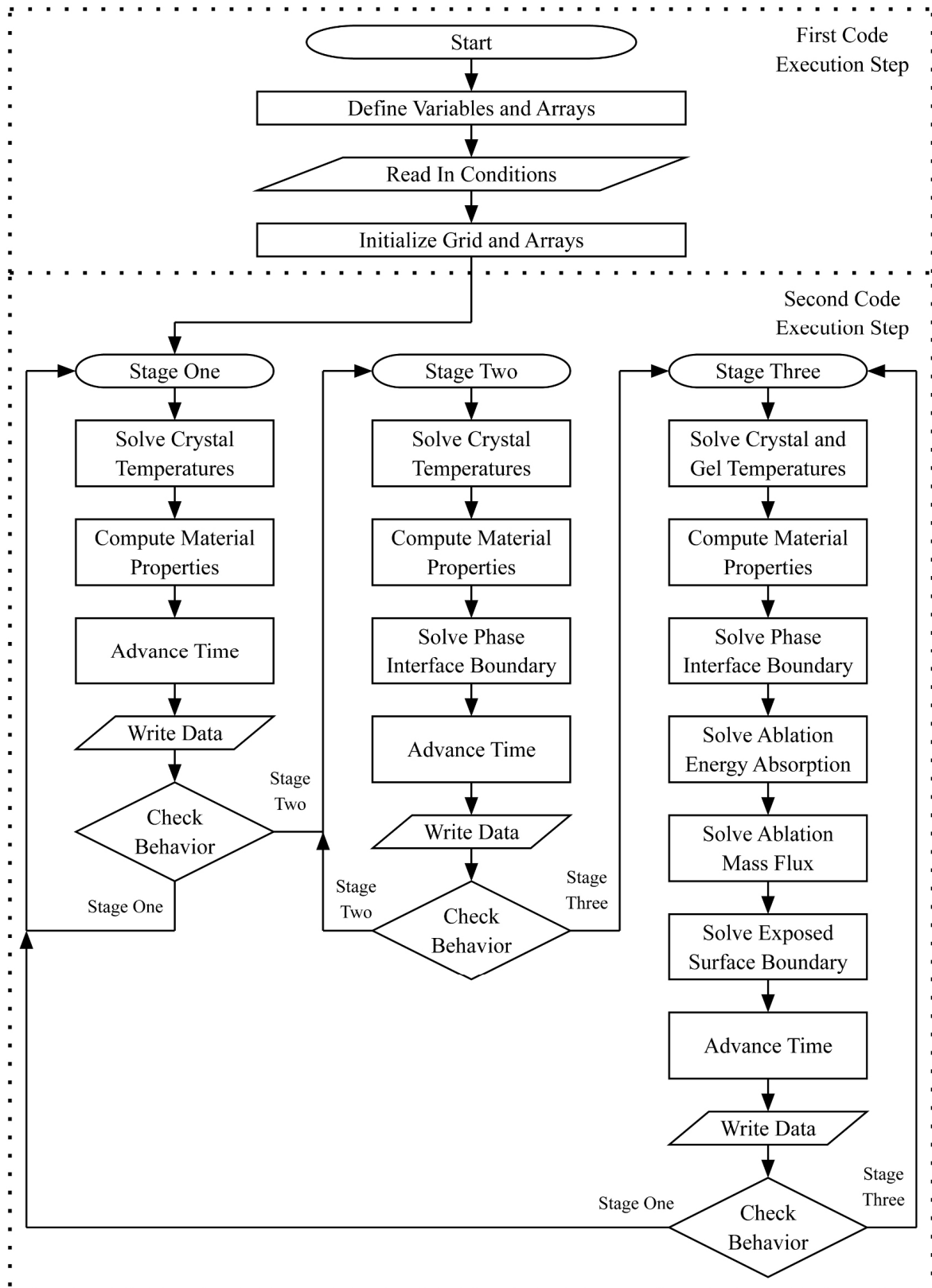


Figure 3.1: General program execution structure

The second execution step consists solely of the main solution iteration loop. Within this main loop, each stage of ablation behavior is treated separately in a sub-loop. Stage one simulates heat conduction within purely crystalline Teflon, stage two simulates heat condition within purely crystalline Teflon when the outer surface reaches the phase transition temperature, and stage three simulates heat conduction, boundary movement, and molecular depolymerization in two-phase crystalline and amorphous Teflon. This description follows the mathematical model discussed in Chapter Two. The results from one stage are passed to a subsequent stage when that portion of the behavior is no longer applicable. The phase interface and ablation boundaries are tracked during stage execution by referencing the cell index to the left of the actual boundary in the discrete physical domain. As time advances, the temperatures throughout the domain are continually updated by solving the conservation of energy relation (discussed in Chapter Two). The boundary conditions and material property matrices are computed based on any changes in input heat fluxes, new temperature values found throughout the Teflon bar, ablated mass flux calculations, and temperature gradients near the phase transformation interface.

Once these steps are completed, time is advanced by a specified time interval (Δt) and the loop is repeated. This process continues for each discrete time step until the end of the PPT pulse is encountered (defined in the input file). At this point, the domain grid can be regenerated in a coarser form (also specified in the input file) by calling a separate grid generation routine. This grid coarsening routine may be called from within any of the behavioral time loops. Grid coarsening is desirable in many circumstances because it allows faster computation during the relatively uneventful inter-pulse heat transfer process. The grid regeneration can take place two additional times during the inter-pulse time period (if these additional generations are specified at runtime). When another pulse of heat flux is encountered, the domain is returned to the initial high-resolution grid structure by calling the same routine. This process continues until the specified simulation end time is reached and all loops are halted.

The general processes outlined above appear straightforward, but several additional details regarding these steps must be addressed before the mathematical relationships discussed in Chapter Two can be used to successfully describe the ablation process. These details include establishing a discrete domain with volume fraction values from the continuous material, the algebraic relationships necessary for the discrete domain from the governing differential equations, the method of computing variable material properties in the discrete domain, the method of interpolating input heat flux data, the method of interpolating temperature values for virtual probe readings, and the parameters necessary to ensure numerical stability.

3.2 Grid Generation and Volume Fraction Concept

One of the primary areas of concern in numerically implementing a mathematical concept is the method employed to segment a continuous medium into a grid. *Clark* (1971) utilized material temperature gradients as well as boundary locations to specify the width and location of the grid centers and edges in a one-dimensional domain. *Clark's* grid was continually updated during execution of the model and created a discrete but morphing representation of the Teflon domain that was adaptable to both heat flux as well as boundary movement. This gave fairly accurate results with limited computational resources. However it required extensive changes to the mathematical model prior to implementation in order to address the grid size and boundary location dynamics. This resulted in excessive complexity and *Clark* found it also created significant numerical stability challenges. This approach was rejected to avoid these issues and retain as much modularity as possible.

There are vastly greater computational capabilities available at the time of this writing than were available for previous research efforts. This allows a simple fixed uniform grid defined at runtime based on domain length and number of grid cells to be used. Such a scheme generally proves adequate in balancing the dynamics of one-dimensional heat transfer problems with computational simplicity. The numerical grid methodology and visual representations of the boundaries are shown in Figure 3.2.

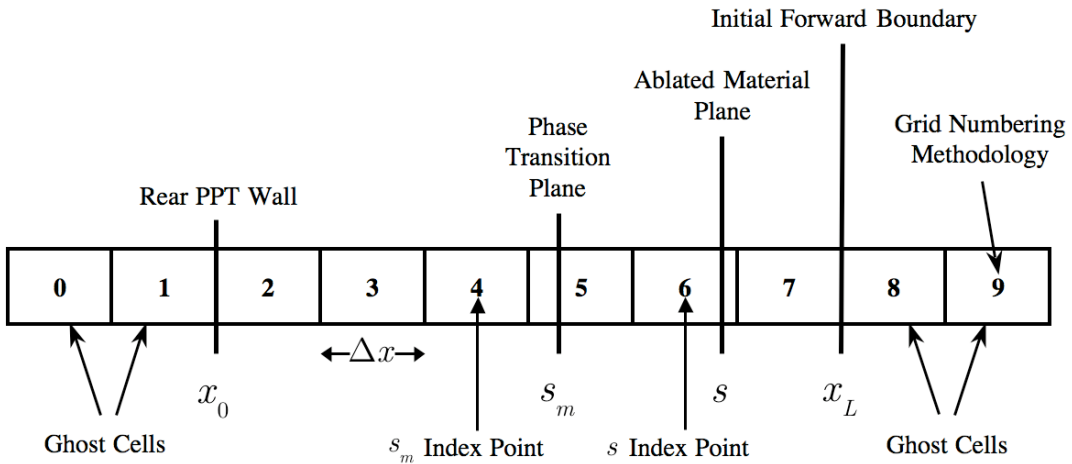


Figure 3.2: Numerical grid with phase transformation and ablation boundaries

Figure 3.2 also illustrates that the computational domain does not begin until the edge of grid cell two. This allows the flux condition at the heat sink interface to be implemented using ghost cells zero and one. Ghost cells are grid cells located outside of the physical domain. Ghost cells are also employed beyond the exposed surface to implement this boundary condition in a similar fashion. As the exposed surface boundary recedes during ablation, those grid cells that are no longer part of the primary domain

become ghost cells. This boundary and the phase transformation interface boundary are both tracked as they move by using a sub-loop during each time step to determine the index of the node to the immediate left of each boundary (nodes are defined at cell center locations). These indices (shown in Figure 3.2 and Figure 3.3) are used when relating the discretized conservation of energy relationships to the grid. They are also used in bounding the domain for additional computations such as determining the summation limit for mass flux within the amorphous domain (discussed later in this Chapter).

Two types of volume functions are used to minimize computational errors due to the domain discretization relative to the moving boundaries. These volume functions are sometimes referred to as material fractions or weighting functions. This document uses the term “volume fraction.” Examples of these volume fractions applied to the boundary cell indices are shown in Figure 3.3.

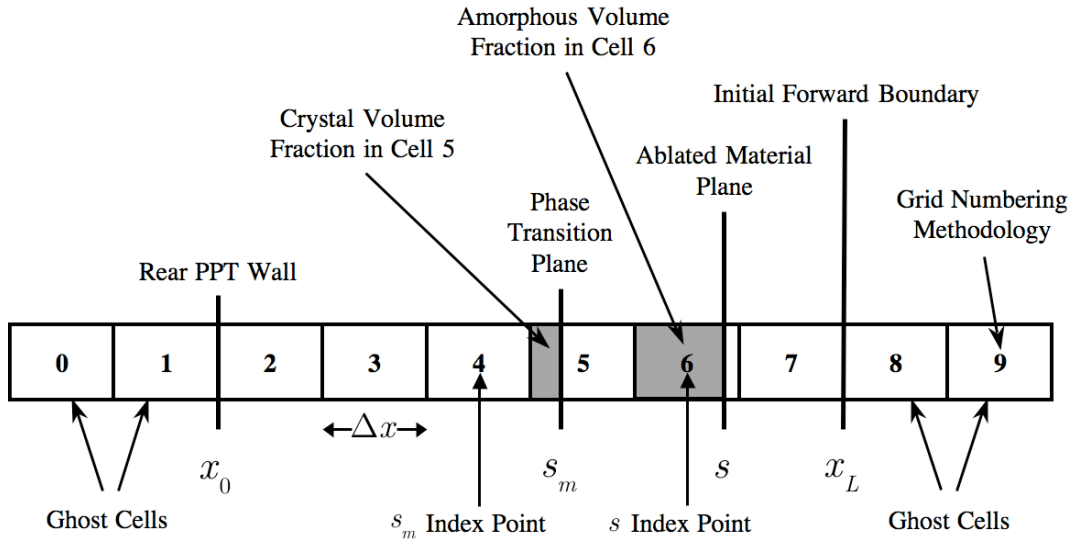


Figure 3.3: Numerical grid with included representations of volume fractions

The first volume fraction value represents the exact fraction of crystalline material in any given cell. It is computed by subtracting the left-hand cell edge of any given cell ($x_{(i-1)}$) from the interface boundary location (s_m) and dividing by the cell spacing as shown by

$$V_{gc(i)} = \max \left(0, \min \left(1, \frac{s_m - x_{(i-1)}}{\Delta x_{(i)}} \right) \right) \quad (3.1)$$

This volume fraction (represented by the grey box near the phase transition plane in Figure 3.3) is bounded between zero (completely amorphous material) and one (completely crystalline material).

The second volume fraction value represents the exact fraction of amorphous material in any given cell. The computation of this value resembles that of the first crystalline volume fraction but there are differences. The subtraction must be reversed because the amorphous material is located on the opposite side of the boundary. The amorphous material also exists only on the left side of the outer ablation surface, so an additional term is added. This additional term computes the amorphous volume fraction near the outer boundary by subtracting the left cell edge ($x_{(i-1)}$) from the exposed interface boundary location and dividing by the cell spacing ($\Delta x_{(i)}$). The exact amorphous fraction in any cell (represented at cell 6 in Figure 3.3 as the dark grey box left of the ablation surface) is bounded in the same way as before and given by

$$V_{ga(i)} = \max\left(0, \min\left(1, \frac{x_{(i)} - s_m}{\Delta x_{(i)}}, \frac{s - x_{(i-1)}}{\Delta x_{(i)}}\right)\right) \quad (3.2)$$

The two volume fraction values create a reference for the quantity of each phase in any given grid cell (i). When combined with the exact boundary locations, they suffice for computation purposes.

The domain methodology described above is straightforward to implement and generally applies well to the majority of heat transfer and ablation scenarios. Nevertheless, it can be computationally costly in very demanding situations. Unfortunately, PPTs often fit these demanding situations. They are likely to have extreme heat fluxes, temperature gradients, and ablation rates for very brief periods over comparatively large time scales of operation. An example of a temperature profile typically encountered in Pulsed Plasma Thrusters is shown in Figure 3.4. The extreme temperature gradients shown near the outer surface require very small grid spacing and correspondingly small time steps to accurately capture the physical behavior. This is computationally intensive if real-world domain sizes several centimeters in length or large multi-pulse time scales several hours in duration are required.

A uniform grid is not a realistic solution option in many cases given the extreme conditions experienced in PPTs. A non-uniform grid is absolutely necessary to group the majority of the computational nodes near the outer surface where the extreme heat fluxes and ablation velocities are present. This minimizes the total number of grid points and reduces the required computational time. It may appear that using a non-uniform grid significantly changes everything discussed previously with respect to grid methodology, but the majority of conditions remain the same. Cell indexing, material volume fractions and ghost cells are all implemented in the same manner. However, cell widths are no longer uniform and become functions of node location. The methodology shown earlier in Figure 3.3 is displayed again in Figure 3.5 with the minor changes required for a non-uniform grid.

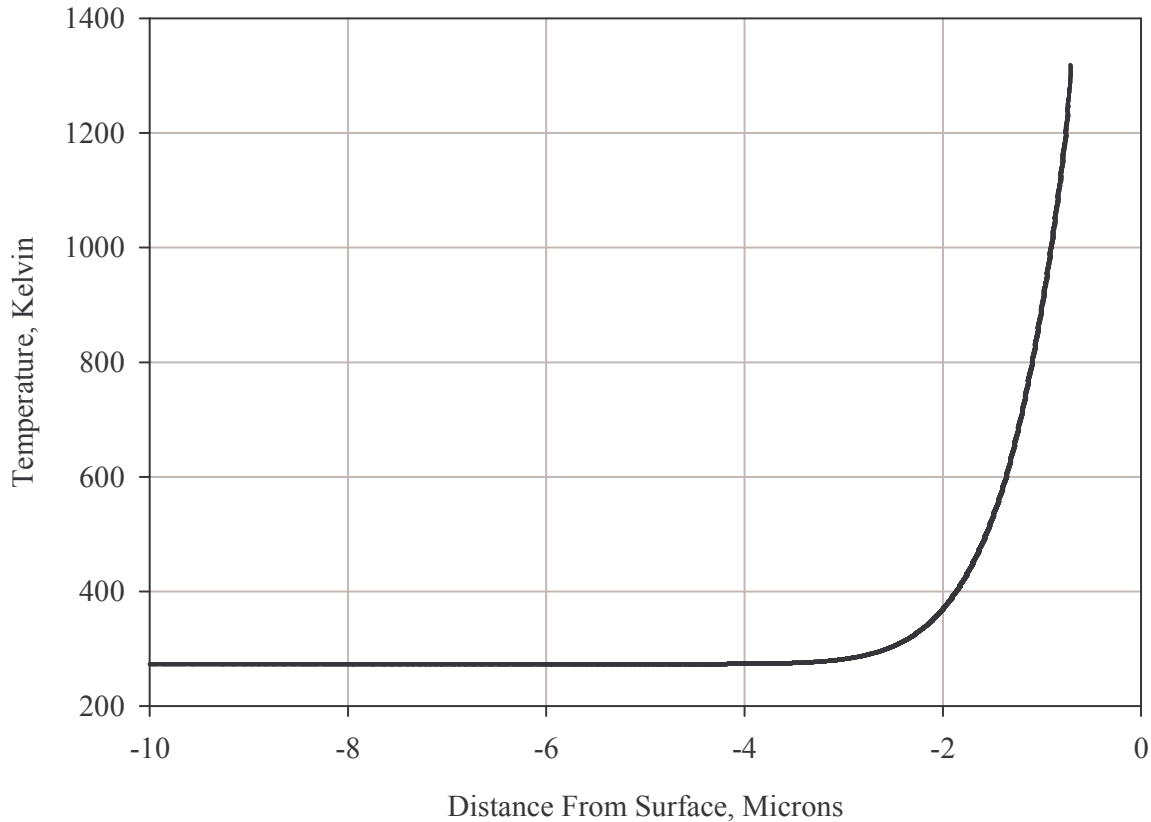


Figure 3.4: An example of the extreme temperature gradients present in a Pulsed Plasma Thruster.

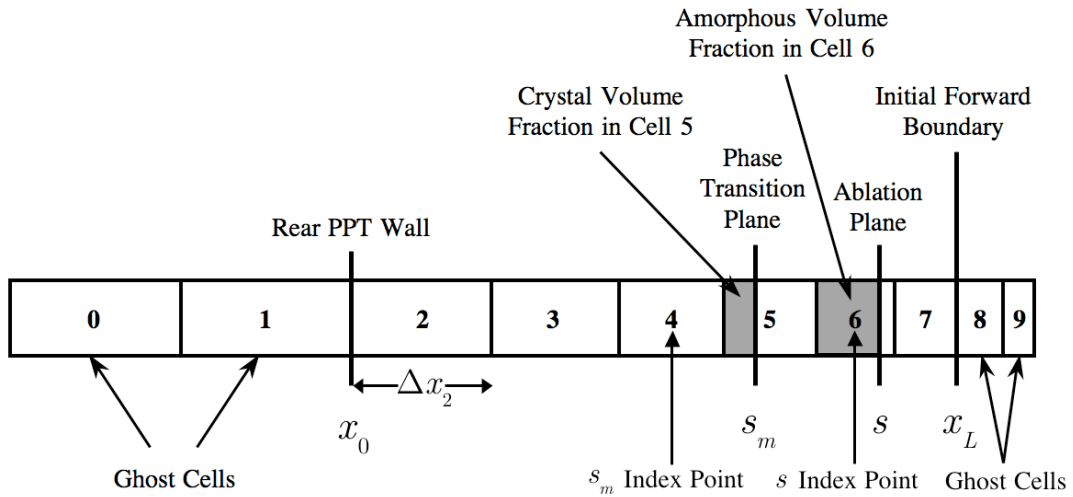


Figure 3.5: The non-uniform grid methodology.

To address both complicated ablation scenarios and more generic heat transfer problems while retaining as much flexibility as possible, either a uniform grid or non-uniform grid may be used for simulation. If a uniform grid is required, the grid is generated as discussed earlier using the domain

length and specified number of grid cells. If a non-uniform grid is required, the uniform domain discretization is still generated but is subsequently transformed into a non-uniform grid prior to computation using an algebraic mapping function given by

$$x_{cnonuniform(j)} = - \left[s + \left(\frac{4}{n_x} \right)^p \right] \left[\left(\frac{x_{cuniform(i)}}{s} \right)^p + s + \left(\frac{4}{n_x} \right)^p \right] \quad (3.3)$$

$$x_{nonuniform(j)} = - \left[s + \left(\frac{4}{n_x} \right)^p \right] \left[\left(\frac{x_{uniform(i)}}{s} \right)^p + s + \left(\frac{4}{n_x} \right)^p \right] \quad (3.4)$$

This mapping function moves the uniform grid cell centers (nodes) and cell edges into locations much closer to the exposed surface. This arrangement is more applicable to problems with extreme heat fluxes and ablation rates such as PPTs.

Equation 3.3 maps node locations (cell centers) and equation 3.4 maps cell edge locations from their uniform locations to the non-uniform locations. In this case, s represents the current domain length, n_x represents the number of grid nodes, and p represents the transformation power exponent (2, 4, 6, or 8 in practice). These expressions applied to an initial uniform domain result in the node transformation shown in Figure 3.6. As can be seen, this transformation places large numbers of nodes near the outer exposed surface (located at 0.03 meters in this case) where they are most useful in demanding simulations. It also retains a reasonable number of nodes in the rest of the domain to accurately account for residual heating of the material over the long time scales of multi-pulse operation. Although it appears the node transformation asymptotically approaches the outer domain surface, it actually passes through the outer surface. This is necessary in order to allow leave several ghost cells beyond the outer surface. It also prohibits grid cells within the domain from approaching a width of zero.

Even with the grid transformation discussed above, simulation of PPT conditions or similar problems with cyclical heat flux cycles is still challenging because of the long time scales of operation and the small time steps necessary. For example, a typical situation might apply extreme amounts of heat flux for 10 microseconds after which little heat flux would be applied until the next pulse cycle several seconds later. In such situations, a transformed high-resolution grid is absolutely necessary only when high heat fluxes and ablation rates are present. When these are not present, a lower-resolution grid is desirable to reduce computation time beyond that which can be achieved through the use of a non-uniform grid alone. To address these issues, the uniform and non-uniform grids described above are implemented such that they may be regenerated up to three times once the initial heat flux values have decreased. Each subsequent generation coarsens the grid by skipping one, three, or five of the original grid points to generate fewer total nodes and allow larger time step values. The number of grid

regenerations and the timing of these regenerations relative to the heat flux cycle are selected by the user at run time. When the portion of the cycle with high heat flux begins again, the original high-resolution grid is restored. This ability to use uniform or non-uniform grids that can be dynamically coarsened or refined during the simulation provides great flexibility in solving cyclical ablation and heat transfer problems with varying degrees of complexity or difficulty.

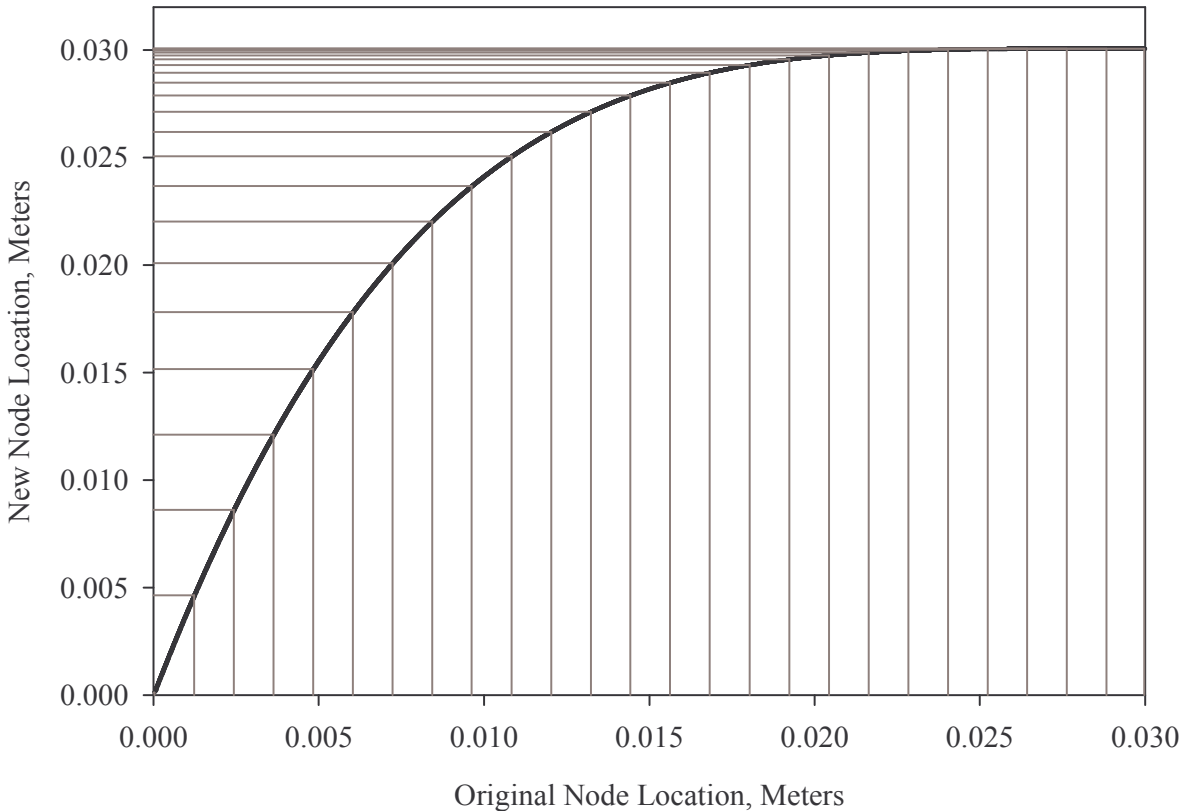


Figure 3.6: The node transformation function applied to a typical domain 0.03 meters in length.

3.3 Finite Difference Technique

The method employed to convert the continuous differential equations into discrete equations is of great importance in numerically implementing a mathematical concept. In this case, Fourier's second law describing heat conduction within the crystalline and amorphous phases provides the primary governing equation and is represented as

$$\rho C \frac{\partial T}{\partial t} = \frac{\partial}{\partial x} \left(k \frac{\partial T}{\partial x} \right) \quad (3.5)$$

Explicit finite-difference techniques are employed for a non-uniform grid to retain code simplicity and flexibility in the ablation model. Implicit finite difference techniques can offer improved performance, but they can also introduce additional stability challenges. *Clark* attempted to use an implicit technique while simulating the same basic problem but abandoned it when numerical stability could not be consistently maintained. There is also greater historical precedent for explicit methods in this type of problem, so explicit methods are viewed as the best choice.

A first-order, forward-difference, up-wind method is used to discretize the time derivative and results in

$$\rho C \frac{\partial T}{\partial t} = \rho_{(i)}^n C_{(i)}^n \frac{T_{(i)}^{n+1} - T_{(i)}^n}{\Delta t} \quad (3.6)$$

A second-order, central-difference method is used to discretize the spatial derivative and results in

$$\frac{\partial}{\partial x} \left(k \frac{\partial T}{\partial x} \right)_{(i)} = \frac{2}{\Delta x_+ + \Delta x_-} \left[k_{(i+1/2)}^n \frac{T_{(i+1)}^n - T_{(i)}^n}{\Delta x_+} - k_{(i-1/2)}^n \frac{T_{(i)}^n - T_{(i-1)}^n}{\Delta x_-} \right] \quad (3.7)$$

In this case, spatial distance differences are computed from the cell center locations as

$$\Delta x_+ = x_{c(i+1)} - x_{c(i)} \quad (3.8)$$

$$\Delta x_- = x_{c(i)} - x_{c(i-1)} \quad (3.9)$$

The intermediate thermal conductivity values are computed as the average between adjacent cells by

$$k_{(i+1/2)}^n = \frac{k_{(i+1)}^n + k_{(i)}^n}{2} \quad (3.10)$$

$$k_{(i-1/2)}^n = \frac{k_{(i)}^n + k_{(i-1)}^n}{2} \quad (3.11)$$

The resulting discrete equations for temperatures within the crystalline phase (used with stage one, two, and three behavior) and the amorphous phase (used with stage three behavior) are derived from the conservation of energy relationship as follows (*Tannehill, Anderson, and Pletcher, 1997*):

$$T_{c(i)}^{n+1} = T_{c(i)}^n + \frac{\Delta t}{\rho_{c(i)}^n C_{c(i)}^n (x_{c(i+1)} - x_{c(i-1)})} \cdot \left[\frac{(k_{c(i+1)}^n + k_{c(i)}^n)(T_{c(i+1)}^n - T_{c(i)}^n)}{(x_{c(i+1)} - x_{c(i)})} - \frac{(k_{c(i)}^n + k_{c(i-1)}^n)(T_{c(i)}^n - T_{c(i-1)}^n)}{(x_{c(i)} - x_{c(i-1)})} \right] \quad (3.12)$$

$$T_{a(i)}^{n+1} = T_{a(i)}^n + \frac{\Delta t}{\rho_{a(i)}^n C_{a(i)}^n (x_{c(i+1)} - x_{c(i-1)})} \cdot \left[\frac{(k_{a(i+1)}^n + k_{a(i)}^n)(T_{a(i+1)}^n - T_{a(i)}^n)}{(x_{c(i+1)} - x_{c(i)})} - \frac{(k_{a(i)}^n + k_{a(i-1)}^n)(T_{a(i)}^n - T_{a(i-1)}^n)}{(x_{c(i)} - x_{c(i-1)})} \right] - \frac{Q_{p(i)}^n \Delta t}{\rho_{a(i)}^n C_{a(i)}^n} \quad (3.13)$$

In the conservation of energy relation within the amorphous phase, energy absorption due to depolymerization (Q_p) becomes a function of the amorphous volume fraction and is discretized as

$$Q_{p(i)}^n = V_{ga(i)} A_p \rho_{a(i)}^n H_{p(i)}^n T_{a(i)}^n \exp\left(-\frac{B_p}{T_{a(i)}^n}\right) \quad (3.14)$$

The heat sink boundary condition at the rear of the domain wall is discretized in a manner similar to the conduction equation by

$$T_{wall}^{n+1} = T_{wall}^n + \left(\frac{2\Delta t}{x_{c(i=2)}^n - x_{c(i=1)}^n} \right) \left(\frac{k_{wall}^n}{\rho_{hs}^n C_{hs}^n \delta_{hs}} \right) (T_{c(i=2)}^n - T_{wall}^n) \quad (3.15)$$

In this case, a single-order central difference is used because of the node locations relative to the rear wall. Since the wall represents the heat sink and is halfway between nodes 1 and 2, linear extrapolation is required to obtain the correct temperature at node 1 (the ghost cell) by

$$T_{c(i=1)}^{n+1} = 2T_{wall}^{n+1} - T_{c(i=2)}^{n+1} \quad (3.16)$$

Node zero is not required in this implementation of the boundary condition and is set to the same value as ghost cell one.

The boundary condition at the exposed surface is discretized in a similar fashion. Crystalline temperatures are used in stages one and two, and amorphous temperatures are used in stage three. As discussed in Chapter Two, the boundary condition in stage one depends only on the applied flux and the surface radiation losses. Note that the applied heat flux in this implementation is defined as negative

when directed into the Teflon domain and positive when directed away from the domain at the exposed surface. The flux boundary condition is thus given by

$$T_{c(i=ics+1)}^{n+1} = T_{c(i=ics)}^n - 2 \frac{\left(x_{c(i=ics+1)}^n - x_{c(i=ics)}^n \right)}{\left(k_{c(i=ics+1)}^n + k_{c(i=ics)}^n \right)} [q + \sigma \varepsilon T_s^4] \quad (3.17)$$

The constant surface temperature used in stage two operating behavior dictates that the ghost cells outside the domain must be discretized somewhat differently from exposed surface ghost cells shown in (3.18). In this case, the ghost cell temperatures are determined by linearly extrapolating the domain thermal gradient into the ghost cells using the location of the surface relative to the cell node. This maintains the surface temperature at the phase transformation temperature (T_m) and is represented by

$$T_{c(ics+1)}^{n+1} = \left(\frac{T_m - T_{c(i=ics)}^n}{s - x_{c(i=ics)}} \right) \left(x_{c(i=ics+1)} - x_{c(i=ics)} \right) + T_{c(i=ics)} \quad (3.18)$$

The two possible exposed surface boundary conditions used during stage three are discretized in a fashion similar to the exposed surface flux condition used in stage one. However, additional terms are necessary to account for energy lost in the ablated mass as well as the blockage effect on the incoming heat flux (used in the convective condition only). The exposed surface convective boundary condition with these added terms becomes

$$T_{c(i=ics+1)}^{n+1} = T_{c(i=ics)}^n - 2 \frac{\left(x_{c(i=ics+1)}^n - x_{c(i=ics)}^n \right)}{\left(k_{c(i=ics+1)}^n + k_{c(i=ics)}^n \right)} [q + \sigma \varepsilon T_s^4 + \dot{m} (\eta (H_e - H_s) - C_s T_s)] \quad (3.19)$$

Likewise, the non-convective exposed surface boundary condition used during stage three becomes

$$T_{c(i=ics+1)}^{n+1} = T_{c(i=ics)}^n - 2 \frac{\left(x_{c(i=ics+1)}^n - x_{c(i=ics)}^n \right)}{\left(k_{c(i=ics+1)}^n + k_{c(i=ics)}^n \right)} [q + \sigma \varepsilon T_s^4 + \dot{m} C_s T_s] \quad (3.20)$$

These relationships comprise the majority of the numerical simulation effort. However, the moving phase interface and ablation surface boundaries remain critical portions of the model.

The phase interface velocity is discretized using single-order forward and backward-differences around the boundary which are represented by

$$v_m^{n+1} = \frac{1}{\rho_m H_m} \left[k_{mc} \frac{\left(T_m - T_{c(i=icsm-1)}^n \right)}{\left(s_m^n - x_{c(i=icsm-1)} \right)} - k_{ma} \frac{\left(T_{a(i=icsm+2)}^n - T_m \right)}{\left(x_{c(i=icsm+2)} - s_m^n \right)} \right] \quad (3.21)$$

The flux conditions on either side of the phase interface boundary are approximated using grid cells two node locations away from the boundary. This approximation avoids divide-by-zero errors as the boundary approaches the nodes to its immediate left or right during simulation. The outer ablation surface velocity becomes a function of the mass depolymerization throughout the amorphous domain given by

$$\dot{m}^{n+1} = \sum_{i=icsm}^{ics+1} \left[V_{ga(i)} A_p \rho_{a(i)}^n T_{a(i)}^n \Delta x_{(i)} \exp \left(-\frac{B_p}{T_{a(i)}^n} \right) \right] \quad (3.22)$$

$$v^{n+1} = \frac{\dot{m}^{n+1}}{\rho_{ref}} \quad (3.23)$$

Once the phase interface and ablation surface velocities are computed, the new locations of the interface surface and ablation surface are easily found by taking an Euler integration step given by

$$s_m^{n+1} = s_m^n + \Delta t (v_m^{n+1}) \quad (3.24)$$

$$s_s^{n+1} = s_s^n + \Delta t (v_s^{n+1}) \quad (3.25)$$

3.4 Material Property Matrices

Material property functions must also be addressed. Since material properties are assumed to be linear functions of temperature within each phase and do not depend on thermal gradients, discretizing these functions is simply a matter of computing the properties at each explicit grid point. The temperature gradients of the material property functions do not change within a given phase, so each material property can be represented by a matrix of values across the domain. These property values can then be computed simultaneously from a composite temperature matrix containing all the cell temperatures values as follows:

$$[\rho_e] = \rho_r + \left(\frac{\rho_{mc} - \rho_r}{T_m - T_r} \right) ([T_e] - T_r) \quad (3.26)$$

$$[\rho_a] = \rho_h + \left(\frac{\rho_h - \rho_{ma}}{T_h - T_m} \right) ([T_a] - T_m) \quad (3.27)$$

$$[C_c] = C_r + \left(\frac{C_{mc} - C_r}{T_m - T_r} \right) ([T_c] - T_r) \quad (3.28)$$

$$[C_a] = C_h + \left(\frac{C_h - C_{ma}}{T_h - T_m} \right) ([T_a] - T_m) \quad (3.29)$$

$$[k_c] = k_r + \left(\frac{k_{mc} - k_r}{T_m - T_r} \right) ([T_c] - T_r) \quad (3.30)$$

$$[k_a] = k_h + \left(\frac{k_h - k_{ma}}{T_h - T_m} \right) ([T_a] - T_m) \quad (3.31)$$

$$[H_p] = H_{p0} - H_{p1} [T_a] \quad (3.32)$$

Using matrices in this way increases the execution speed of an otherwise repetitive and computationally-intensive step.

3.5 Heat Flux Interpolation

Interpolation of heat flux data from the heat flux input file constitutes a 4th aspect of the numerical model. One of the strengths of the numerical modeling method is the ability to solve any problem having variable heat flux boundary conditions. However the method used to vary the heat flux boundary condition can introduce difficulties or place significant constraints on model flexibility. To retain flexibility, problem-specific heat flux data (q) are read as discrete values at specified time intervals from a heat flux input file. This allows generation of any heat flux profile and does not restrict heat flux to a non-configurable function within the code architecture. However, simple use of discrete heat flux values can introduce significant errors unless very high input resolutions are used. To minimize this, the actual heat flux applied to the boundary condition at the exposed surface is computed using linear interpolation between the two nearest heat flux values in the discrete data set by

$$q = q^n + \left(\frac{q^{n+1} - q^n}{\Delta t_{qinput}} \right) \left(t - \Delta t_{qinput} (n_{qcounter} - 1) \right) \quad (3.33)$$

In this equation, q^n represents the heat flux value read at the old time interval, q^{n+1} represents the heat flux value read at the next time interval, Δt_{qinput} represents the time interval specified between

heat flux values (not necessarily the time step size of the main loop), and $n_{qcounter}$ represents the heat flux data input counter. The heat flux counter increments each time a new heat flux value is read in from the data file (done once every heat flux time interval). The interpolation process then continues using the new data point.

3.6 Virtual Probe Temperature Interpolation

Simulated temperatures must be observable at any location within the domain at any point in time. This is required for comparison with experimental thermocouple data or detailed observation of thermal response. Unfortunately, the discrete numerical representation complicates this observation process. As discussed before, the value of a property at any point can be approximated by linearly interpolating values recorded at discrete reference points on either side of the desired location. For the virtual probe temperature, the index of the grid cell to the left of the probe is first located in the same way as for the phase transformation and exposed surface boundaries. This index is then used to select the reference cells on either side of the virtual probe. The temperatures of these cells and their distances from the probe location (x_{ploc}) are used to interpolate the probe temperature (T_{ploc}^n) at the current point in time by

$$T_{ploc}^n = \frac{\left(T_{(i=iploc+1)}^n - T_{(i=iploc)}^n \right)}{\left(x_{c(i=iploc+1)} - x_{c(i=iploc)} \right)} \left(x_{ploc} - x_{c(i=iploc)} \right) + T_{(i=iploc)}^n \quad (3.34)$$

3.7 Numerical Stability Analysis

Stability is an extremely important concern in the numerical solution of the Teflon ablation problem. Given the second-order explicit finite difference technique and the fixed grid, it is straightforward to analyze the numerical stability when defined in terms of the thermal diffusion limit. In other words, it is necessary to employ a time step size small enough so that thermal effects do not propagate more than one grid cell distance each time step. This limiting time step value is a function of grid size and material properties. The material properties vary throughout the domain so the maximum allowable time step size for each cycle is computed using global maxima and minima of these properties by

$$\Delta t_{\max} = \frac{\left(\min(\Delta x) \right)^2 \cdot \min(\rho) \cdot \min(C)}{2 \cdot \max(k)} \quad (3.35)$$

The actual step size used is selected to be some fraction of the maximum.

The diffusion limit criterion is the only condition necessary to ensure stability of the numerical method. Nevertheless, other criteria should be met to avoid creating significant errors in the results or causing the code execution sequence to break down and terminate prematurely because of numerical exceptions. These criteria are difficult to quantify in any general context but can cause the following problems if not met:

- Very coarse grid resolutions can lead to large time step values that cause the ablation behavior of the model to jump between operating stages too quickly. Coarse grids can also cause the outer ablation surface of the phase transformation interface to move more than one grid cell each time step. These problems can result in significant calculation error and lead to premature termination.
- Specific heat, density, or thermal conductivity values that vary significantly with temperature (as defined by the user) can lead to situations where thermal diffusivity values near the ablation surface approach infinity at high temperatures. This reduces the time-step size to zero and can prevent the solution from advancing and producing results.
- A long-duration ablation simulation using a transformed grid that is not periodically regenerated can cause the exposed Teflon surface to recess in such that the effective grid near the surface becomes much coarser than the original grid. This can lead to significant errors or other problems similar to those possible when the grid is initially too coarse. Unlike the stability challenges associated with initially coarse grids, however, problems associated with this may not be apparent at the beginning of the simulation. If later pulses in the simulation process appear to require significantly less computational time than earlier pulses, however, it is an indication such a problem is occurring.

Sufficiently small grid resolutions generally result in time step sizes that prevent these problems from occurring. In some circumstances, it is necessary to initially use coarse grid resolutions to determine general progression of the solution. In these cases, the user will need to use trial-and-error explorations to discover the grid resolution limit that avoids these troubles. In practice, one should use grid resolutions much greater than this limit to minimize error.

3.8 A Computational Example

A scenario similar to what may be encountered in a PPT is generated to test the one-dimensional ablation model and demonstrate the capabilities of the numerical implementation. In this scenario, a 3.0

centimeter Teflon domain is subjected to the pulsed heat flux profile shown in Figure 3.7. This heat flux profile is applied sequentially at one second intervals for 5 minutes resulting in a total of 360 heat flux cycles or pulses. The material properties of Teflon are assumed to vary linearly with temperature within each phase following the properties established by *Clark* (1971). Virtual thermocouples are placed 20mm, 28mm and 29.5mm from the rear PPT wall to assist in characterizing the thermal response.

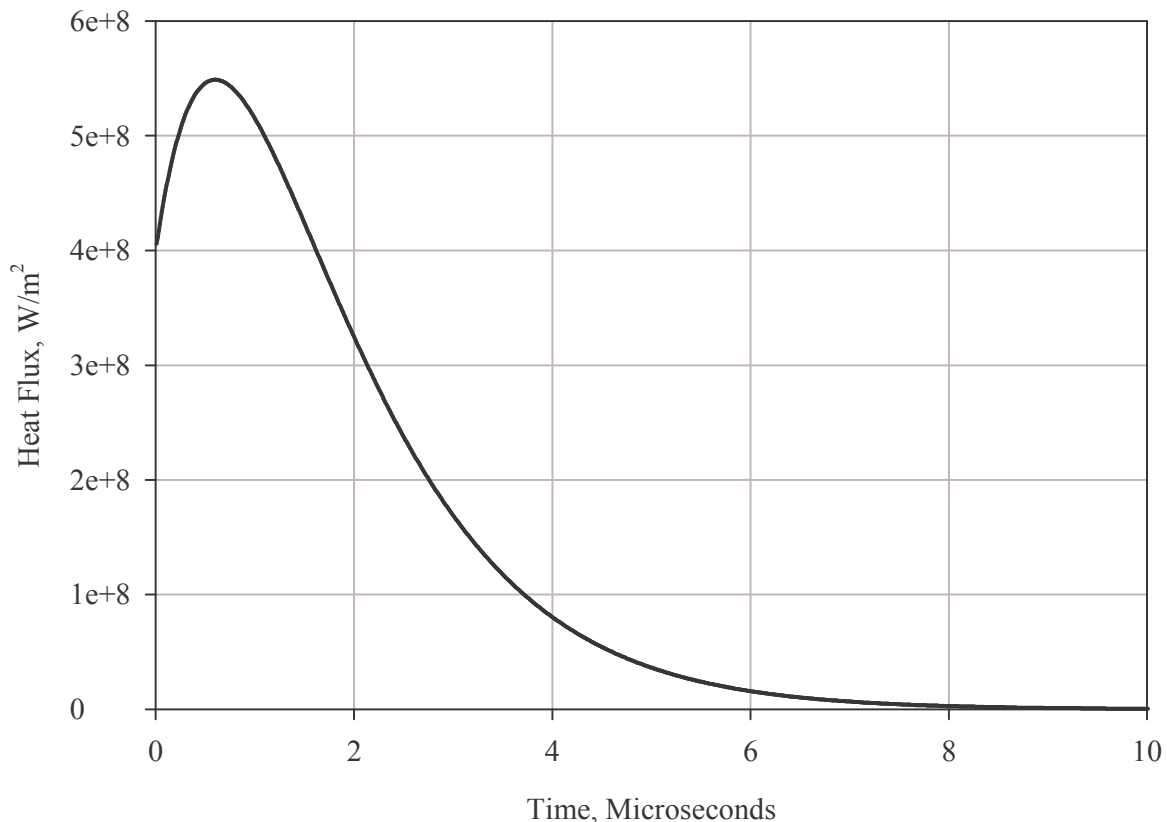


Figure 3.7: Pulsed heat flux profile applied sequentially at 1 second intervals in the example ablation scenario.

For this problem, a non-uniform grid with 400 nodes and a transformation power (p) of 4 is initially generated from the default uniform grid. The number of grid cells and the grid transformation power selected in this scenario provide a reasonable balance between solution error and required computational resources given the domain size and heat fluxes experienced in this problem. This non-uniform grid is regenerated in sequentially coarser forms at 60 microseconds, 500 microseconds, and 10000 microseconds after the start of each pulse to minimize computation time. The grid is restored to its full resolution at the start of each heat flux pulse. The Teflon is assumed to be at room temperature (293 Kelvin) prior to testing, and the heat flux is assumed to be non-convective. A 1.0 centimeter steel heat sink attached to the rear end of the domain completes the model's initial conditions. The resulting

solution data are representative of the types of information that can be obtained from the numerical Teflon ablation model.

One important feature of simulating the ablation process numerically over multiple pulse cycles is obtaining mass flux profiles from the given heat flux input. For this particular scenario, the observed ablation rates during pulses 1 and 360 are shown in Figure 3.8. As can be seen from these results, the mass flux profile changes over the course of multiple firings even though the applied heat flux profile remains the same. This is expected because residual heat within the domain will tend to increase overall propellant temperature and allow easier ablation during subsequent firings. The increase in temperature is apparent by observing the entire domain temperature profile at different intervals just prior to beginning the next period of applied heat flux (Figure 3.9). As can be seen from these results, the domain temperatures tend to increase as the cyclical heat flux process progresses. The low thermal diffusivity of Teflon keeps this effect from producing a uniform temperature increase and instead generates large-scale temperature variation within the propellant. These large scale variations can also be observed in the temperature response from the aforementioned virtual thermocouples shown in Figure 3.10.

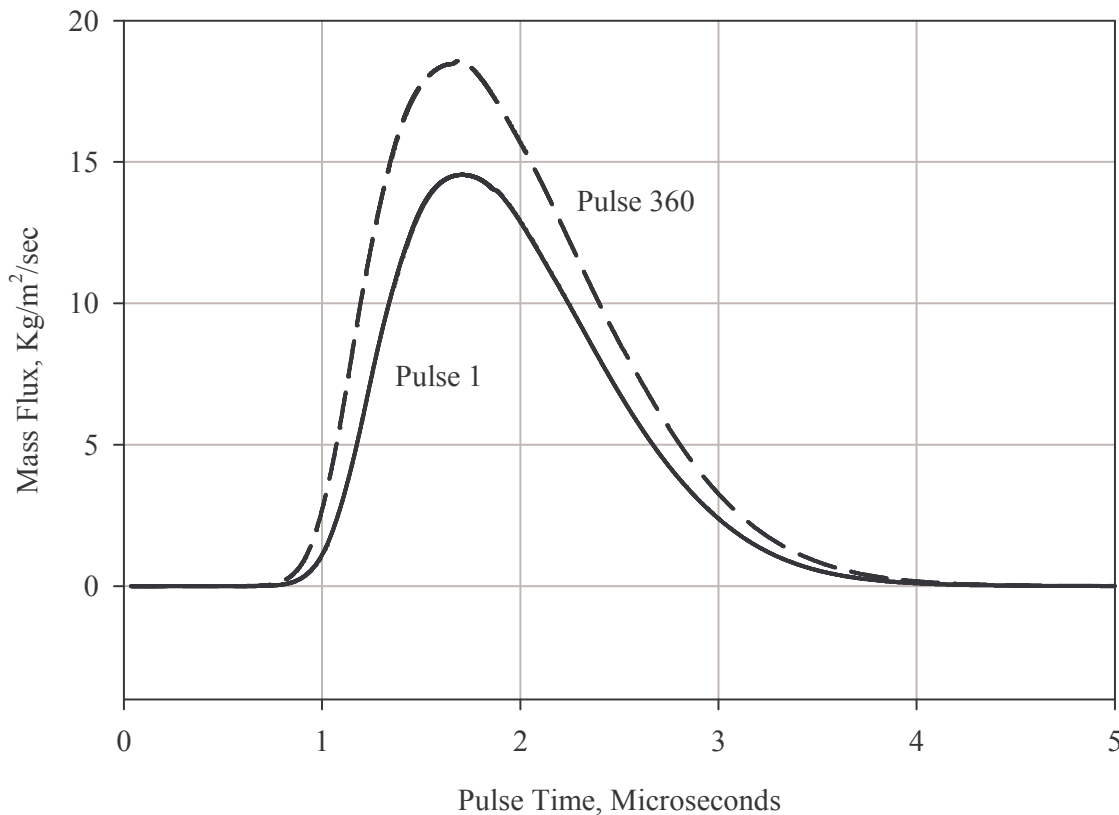


Figure 3.8: Ablation rates during pulse 1 and pulse 360 as a function of pulse time in the example ablation scenario.

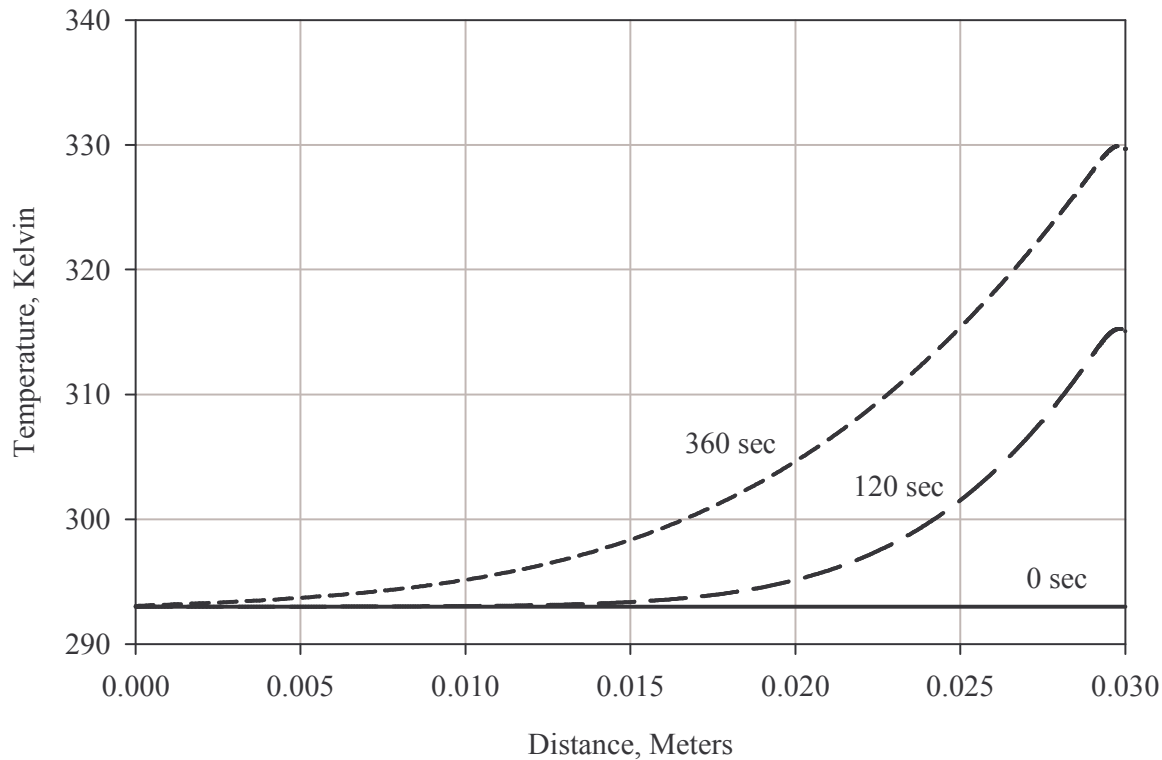


Figure 3.9: Temperature profiles in the entire Teflon domain at zero, 120, and 360 seconds prior to the start of the next applied heat flux sequence.

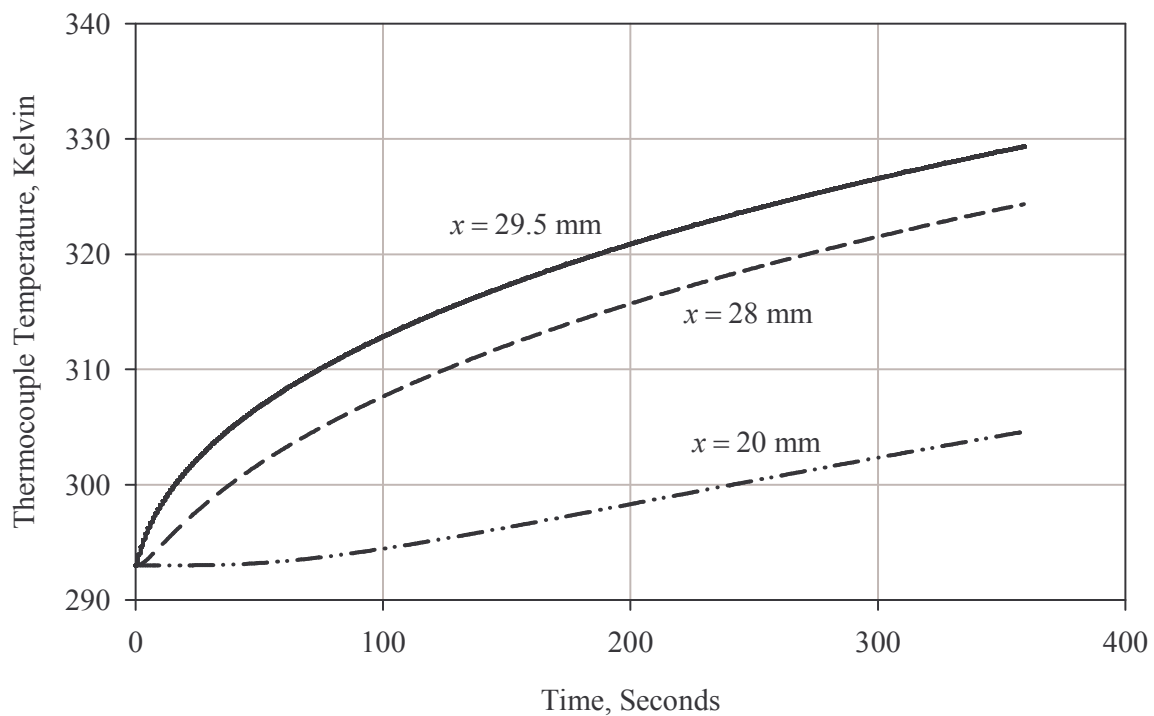


Figure 3.10: Thermocouple responses at three locations over the long duration simulation in the example Teflon domain.

In spite of the noticeable effect on mass ablation rate, the long-term large-scale temperature gradients are dwarfed by the temperature gradients near the forward ablation surface during and immediately after each pulse (shown in Figure 3.11). The heat flux that produces these momentarily large temperature gradients is ultimately what drives the melting and ablation processes. These temperature gradients ultimately produce very high melting rates and ablation rates for the first pulse (Figure 3.12). Nevertheless, the very short duration of the applied heat flux limits the total amount of ablated and melted material to a small region near the exposed surface as shown in Figure 3.13. It should be noted that the fixed grid (whether uniform or non-uniform) tends to produce somewhat noisy boundary velocity data. For this reason, it is necessary to apply a simple moving average over several data values to obtain a smooth representation of these results. Regardless, the quality and diversity of results that can be obtained from the ablation model as demonstrated in this computational example provide greater insight into the heat transfer and ablation process.

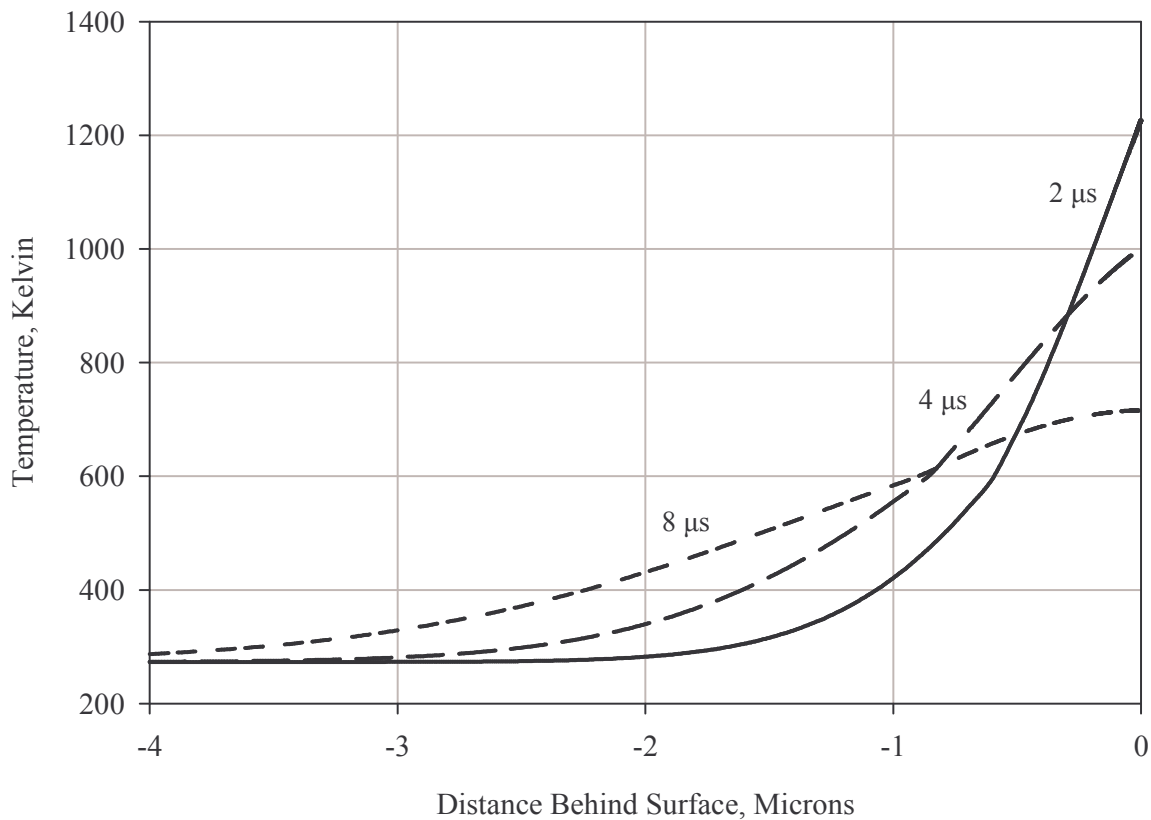


Figure 3.11: Temperature profiles near the exposed Teflon surface at three time intervals after the start of the first pulse in the example pulse sequence.

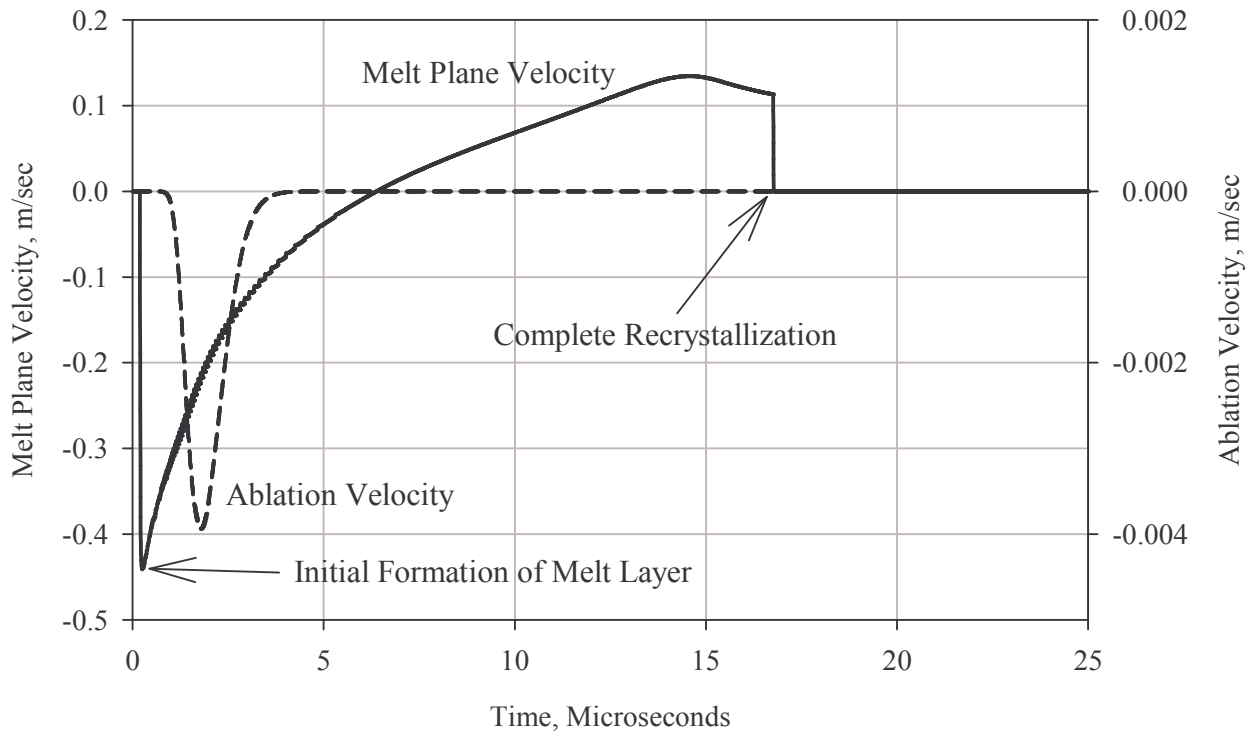


Figure 3.12: Phase transformation boundary velocity and exposed surface ablation velocity during the first pulse in the example pulse sequence.

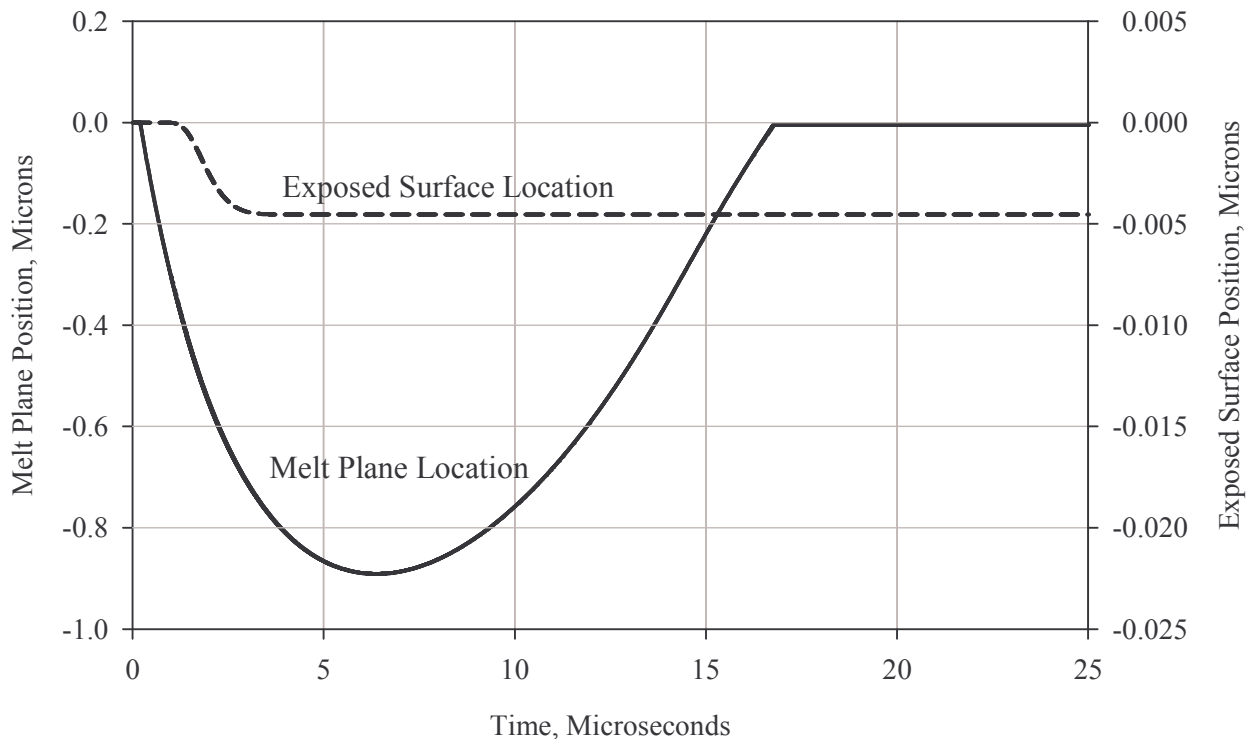


Figure 3.13: Phase transformation boundary and exposed surface locations during the first pulse in the example pulse sequence.

Chapter 4

Model Validation

A model must be validated to ensure accurate and meaningful results. To this end, the one-dimensional Teflon ablation model developed in Chapters Two and Three was tested against documented heat transfer and ablation scenarios. Since individual aspects of the model could only be validated under certain constraints or assumptions, seven scenarios were ultimately selected. Each of the scenarios (listed below) built on the successful validation of concepts in prior scenarios. This allowed all model capabilities to be tested while maintaining independent testing of the each component. The correspondence demonstrated between the model results and those from analytical analysis or prior work indicate that an accurate representation of the physical process was achieved.

1. One-dimensional heat conduction in a one-phase, semi-infinite domain with constant material properties, constant heat flux at the forward boundary, and fixed boundary locations.
2. One-dimensional heat conduction in a one-phase semi-infinite domain with constant material properties, constant rear-boundary temperature, and fixed boundary locations.
3. One-dimensional heat conduction out of a finite heat-sink with constant domain temperature and constant material properties.
4. One-dimensional heat conduction in a one-phase semi-infinite domain with linearly-variable thermal conductivity, constant density, constant specific heat, constant heat flux at the forward boundary, and fixed boundary locations.
5. One-dimensional heat conduction in a two-phase semi-infinite domain with constant material properties, constant heat flux at the forward boundary, and negligible temperature gradients within the crystalline material phase.
6. Steady-state mass flux and surface recession due to molecular depolymerization in a one-dimensional, semi-infinite single-phase domain with variable thermal conductivity, variable specific heat, constant density, and constant heat flux at the forward boundary.
7. Simulated PPT operation with variable heat flux and variable material properties in a finite domain using grid coarsening options to speed simulation.

4.1 Scenario One

The first comparison scenario focuses on one-dimensional transient heat conduction in a single-phase material. This validates the modeling of the governing heat transfer equations in addition to the heat flux boundary condition at the exposed surface. The process of transient heat conduction is described by

$$\rho C \frac{\partial T}{\partial t} = \frac{\partial}{\partial x} \left(k \frac{\partial T}{\partial x} \right) \quad (4.1)$$

To simplify the governing equation such that an exact analytical solution can be found, this scenario assumes constant material properties (thermal conductivity, density, and specific heat), a surface boundary location fixed at 1.0 centimeter, and constant heat flux at the outer surface. The heat conduction is assumed to take place in a semi-infinite domain where thermal gradients at the rear boundary can be neglected and the initial temperatures within the material are constant. These assumptions generate the following initial and boundary conditions:

$$q_g(x, t = 0) = 0 \quad (4.2)$$

$$T(x, t = 0) = T_{init} \quad (4.3)$$

$$q_g(x = 0, t > 0) = q \quad (4.4)$$

$$q_g(x \rightarrow \infty, t > 0) = 0 \quad (4.5)$$

Equation (4.1) must be modified to incorporate these conditions and generate an analytical solution by changing to a function of general heat flux within the domain (q_g) given by

$$q_g(x, t) = q \left[erfc \left(\frac{x}{\sqrt{4\alpha t}} \right) \right] \quad (4.6)$$

The modified equation then becomes

$$\frac{\partial q_g}{\partial t} = \alpha \frac{\partial^2 q_g}{\partial x^2} \quad (4.7)$$

This new governing relationship can subsequently be solved exactly for the heat flux at any position and time by applying Fourier's first law (*Eckert and Drake*, 1987) given by

$$q_g = k \left(\frac{\partial T}{\partial x} \right) \quad (4.8)$$

With this conversion, the analytical solution to temperature is derived as

$$T(x, t) = \frac{q}{k} \sqrt{\frac{4\alpha t}{\pi}} \left[\exp\left(-\frac{x^2}{4\alpha t}\right) - x \sqrt{\frac{\pi}{4\alpha t}} \operatorname{erfc}\left(\frac{x}{\sqrt{4\alpha t}}\right) \right] + T_{init} \quad (4.9)$$

In this solution, the location x is measured in reference to the exposed surface of the material rather than the rear domain wall as is usually specified. Nevertheless, the exact solution can be easily compared with numerical model results assuming all simplifications and conditions are also applied to the numerical model. These conditions are as follows.

$$q = 75900 \text{ W/m}^2$$

$$\rho = 1914 \text{ Kg/m}^3$$

$$T_{init} = 296 \text{ K}$$

$$C = 707.9 \text{ J/Kg/K}$$

$$k = 0.2477 \text{ W/m/K}$$

$$t = 1, 2, \text{ and } 4 \text{ seconds}$$

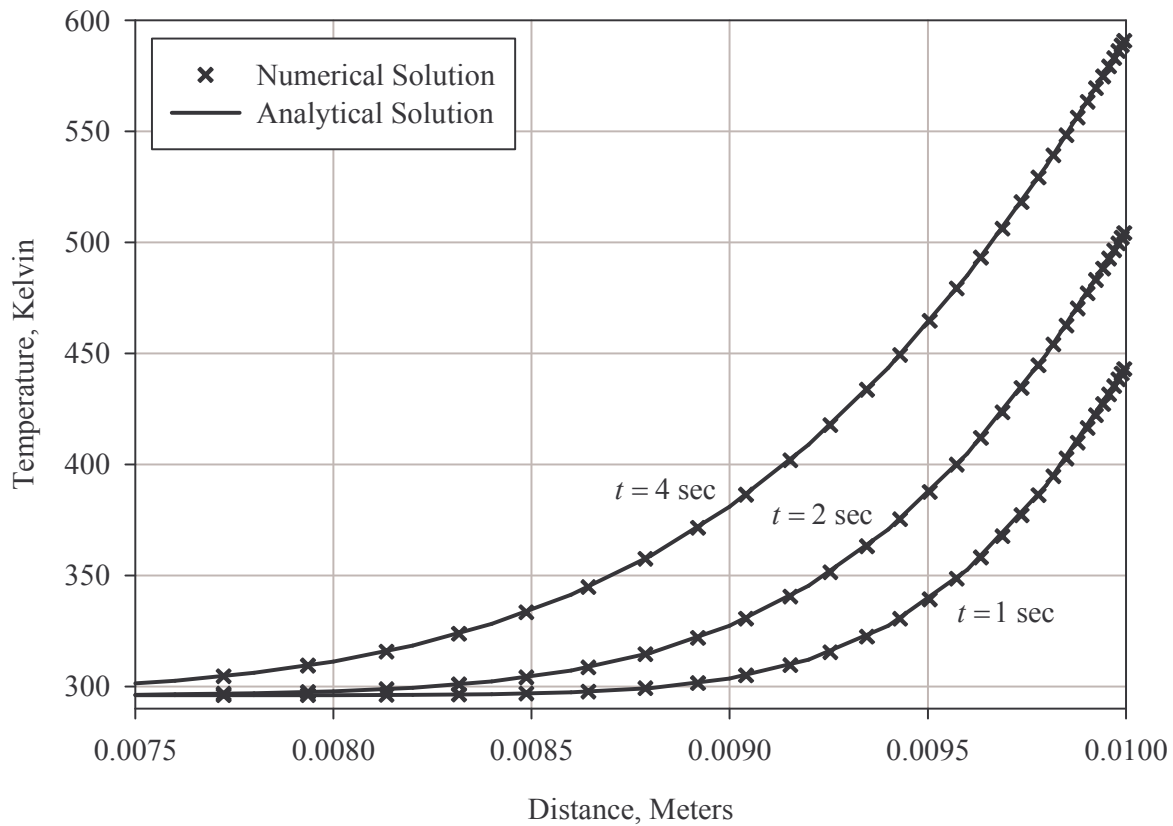


Figure 4.1: Temperature profile comparisons within the Teflon domain for Scenario One assumptions.

The results of this comparison are shown in Figure 4.1. As can be seen, the numerical results (in the form of discrete cell temperature values) match the analytical solution to a high degree of accuracy. Therefore, it can be conclusively stated that the numerical model accurately represents transient heat conduction and the incident heat flux boundary condition. Such a match would not be possible if either was not represented correctly. While this particular scenario involves transient heat flux within crystalline Teflon, the results also validate transient heat conduction within amorphous Teflon because the numerical implementation of the governing equations is the same in both material phases.

4.2 Scenario Two

The second scenario focuses on one-dimensional transient heat conduction in a single-phase material with a prescribed rear surface temperature. All other assumptions are identical to those used in Scenario One. This scenario evaluates the effects of the heat sink on the Teflon domain since the heat sink drives heat flux and temperature distributions near the rear domain boundary. The heat sink boundary condition is not validated by the solution described in Scenario One and thus requires this validation case. As discussed before, transient heat conduction is governed by Fourier's second law, given by

$$\frac{\partial T}{\partial t} = \alpha \frac{\partial^2 T}{\partial x^2} \quad (4.10)$$

The analytical solution to this relationship can be solved in a fashion similar to that of scenario one using the following initial and boundary conditions appropriate to the problem at hand:

$$T(x, t = 0) = T_{init} \quad (4.11)$$

$$T(x = 0, t > 0) = T_{wall} \quad (4.12)$$

$$T(x \rightarrow \infty, t > 0) = T_{init} \quad (4.13)$$

With these conditions, the solution to Fourier's second law takes a form resembling the analytical solution in scenario one where the temperature within the material is given as a function of the distance from the wall (x) and time (t) (Eckert and Drake, 1987) by

$$T(x, t) = (T_{init} - T_{wall}) \operatorname{erf}\left(\frac{x}{2\sqrt{\alpha t}}\right) + T_{wall} \quad (4.14)$$

The analytical solution in scenario one assumed the outer surface was defined at $x = 0$ (with material inside given by a positive x value). The analytical solution in this scenario uses the more conventional coordinate system and assumes the rear wall heat sink is located at $x = 0$ (with material some distance from the rear wall given by a positive x value). It should be noted that in general, a constant temperature boundary condition is not the same thing as a heat sink. In this scenario, however, such a condition is required to validate the effect of a given heat sink temperature on the domain.

The solution outlined above is easily compared with numerical model results computed using the same assumptions and initial conditions. The properties and conditions used in the analytical solution and the numerical model are:

$$\begin{array}{ll} T_{wall} = 0 \text{ K} & \rho = 1914 \text{ Kg/m}^3 \\ T_{init} = 296 \text{ K} & C = 707.9 \text{ J/KgK} \\ k = 0.2477 \text{ W/mK} & t = 1, 4, \text{ and } 16 \text{ seconds} \end{array}$$

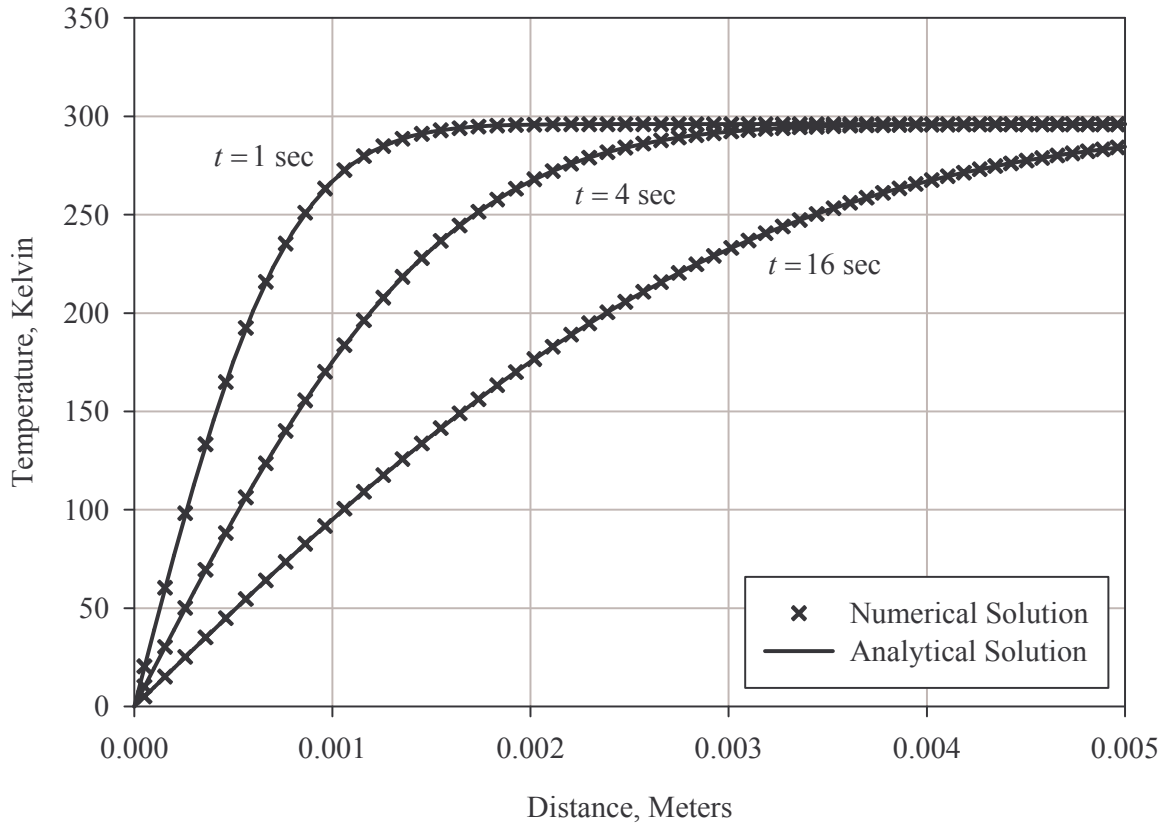


Figure 4.2: Temperature profile comparisons within the Teflon domain using the assumptions and conditions of Scenario Two.

The results of this comparison are shown in Figure 4.2. The numerical results (in the form of discrete cell temperature values) again match the analytical solution to a high degree of accuracy. Therefore, it can be claimed that the numerical model accurately represents heat conduction near the heat sink. In order to completely verify this boundary condition, however, the effects of the Teflon behavior on the heat sink temperature itself must be validated. This forms the basis for scenario three.

4.3 Scenario Three

The second validation scenario focused on the rear boundary condition and the effects of the heat sink on temperatures within the domain. However, the converse was left untested. In other words, the effect of the material temperature near the rear boundary on the heat sink temperature itself could not be evaluated using the same analytical relationship and requires a separate validation scenario. Once again, the heat flux out of the heat sink is governed by Fourier's second law; in this case specified in terms of thermal diffusivity by

$$\frac{\partial T}{\partial t} = \alpha \frac{\partial^2 T}{\partial x^2} \quad (4.15)$$

When applied to the heat sink boundary condition, this expands to

$$-k_c \frac{\partial T_c}{\partial x} = \rho_{hs} C_{hs} \delta_{hs} \frac{\partial T_{hs}}{\partial t} \quad (4.16)$$

Unlike previous scenarios, the only thermal gradient in this scenario is localized just outside of the heat sink in grid cell 2. Temperature gradients within the heat sink are ignored due to the very high thermal conductivity of the metal, and gradients in all other parts of the domain are ignored due to the constant domain temperature. This temperature profile is shown in a hybrid numerical and physical representation of the domain in Figure 4.3.

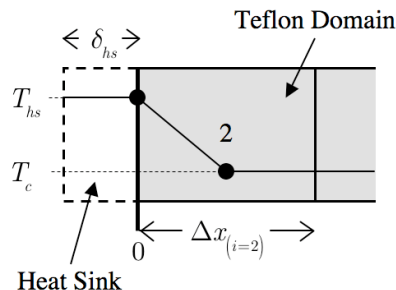


Figure 4.3: Temperature profile used in the scenario three validation case shown with relative wall and node temperature values on a hybrid numerical and physical domain representation.

Under the governing assumptions depicted above, the rate of temperature change in the heat sink is governed by the interface thickness in the numerical domain $0.5\Delta x_{(i=2)}$, the initial heat sink temperature T_{hsinit} , the Teflon boundary temperature T_c , the elapsed time t , and the heat sink material properties by

$$\frac{-k_c}{\Delta x_{(i=2)} (\rho_{hs} C_{hs} \delta_{hs})} dt = \frac{dT_{hs}}{(T_{hs} - T_c)} \quad (4.17)$$

Solving for heat sink temperature as a function of time yields

$$T_{hs}(t) = (T_{hsinit} - T_c) \exp\left(\frac{-2k_c t}{\rho_{hs} C_{hs} \delta_{hs} \Delta x_{(i=2)}}\right) + T_c \quad (4.18)$$

It should be noted that the heat sink temperature can be described by these equations only if the Teflon interface temperature remains constant. In reality, this would not be the case as demonstrated by the variable temperatures observed near the rear domain boundary in scenario two. The effect of the heat sink on these temperatures were validated by the second scenario, so the temperature near the rear boundary can be fixed in this case to validate the effects on the heat sink. All material properties and simulation conditions except the fixed domain temperatures are the same as those of scenarios one and two. The model results are compared with the analytical model described above in Figure 4.4 to completely validate the rear boundary condition. The conditions used for this validation are as follows:

$T_c = 0 \text{ K}$	$\rho_{hs} = 7860 \text{ Kg/m}^3$
$k_c = 0.2477 \text{ W/mK}$	$C_{hs} = 500 \text{ J/KgK}$
$\delta_{hs} = 0.001 \text{ m}$	$T_{hsinit} = 100 \text{ K}, 300 \text{ K} \text{ and } 500 \text{ K}$
$\Delta x_{(i=2)} = 5 \times 10^{-5} \text{ m}$	

As can be seen, the numerical results accurately match the analytical solution as the heat sink cools from the initial temperature T_{hsinit} to the fixed Teflon domain temperature ($T_c = 0 \text{ K}$ in this case for simplicity). These results, taken in combination with those from scenario two, indicate that the heat-sink boundary condition is implemented correctly within the code. If this were not the case, the results would diverge from the analytical solutions in either of the two validation scenarios associated with the rear boundary.

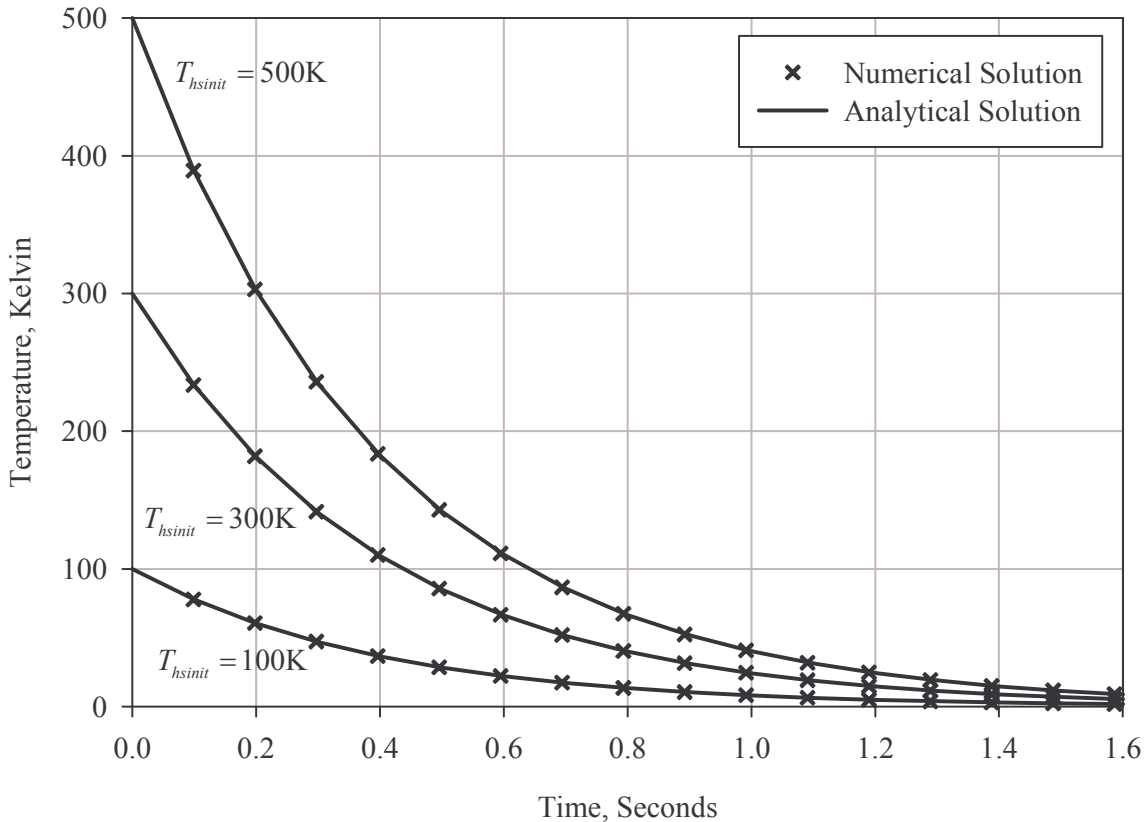


Figure 4.4: Heat sink temperature response over time for the initial conditions and assumptions used in Scenario Three.

4.4 Scenario Four

The fourth validation scenario focuses on the methodology used to implement the material property functions. In all prior scenarios, material properties were assumed to be constant to allow comparison with exact solutions. Since the ablation model considers material properties to be linear functions of temperature, however, the effects of these variable properties on temperature profiles must be evaluated. Unfortunately, factoring variable material properties into this situation greatly complicates analytical analysis and usually makes it impossible to derive exact solutions. Nevertheless, there is a class of problem applicable to this situation that can be evaluated with relative ease. This also starts with Fourier's second law given by

$$\rho C \frac{\partial T}{\partial t} = \frac{\partial}{\partial x} \left(k \frac{\partial T}{\partial x} \right) \quad (4.19)$$

In this situation, thermal conductivity is allowed to vary linearly with temperature. An approximate solution can be derived from this relationship by simplifying the nonlinear boundary-value problem (which would normally arise with temperature dependent material properties) and reducing it to an ordinary initial value problem using a variable transformation given by *Eckert and Drake* (1987). The transformed temperature (given by v) should not be confused with the exposed surface recession velocity (given by v) in spite of the fact that the variables appear similar. This transformation relates temperature to material density and specific heat by

$$v(x, t) = \int_0^T \rho C dT \quad (4.20)$$

The modified governing equation then becomes

$$\frac{\partial v}{\partial t} = \frac{\partial}{\partial x} \left(\alpha(v) \frac{\partial v}{\partial x} \right) \quad (4.21)$$

This equation is integrated with respect to x between the exposed surface (located at $x = 0$ in this case) and the maximum depth of heat penetration into the material δ according to

$$\frac{d}{dt} \left[\int_0^\delta v dx - v_i \delta(t) \right] = -\alpha(v_s) \frac{\partial v}{\partial x}(0, t) \quad (4.22)$$

The following constant flux boundary conditions are subsequently applied:

$$v(x, t = 0) = 0 \quad (4.23)$$

$$k \frac{\partial}{\partial x} v(0, t) = -q \quad (4.24)$$

Since temperature profiles can often be approximated with polynomial functions, a cubic relationship is assumed according to *Eckert and Drake* (1987) to simplify the relationship to

$$\frac{v}{v_s} = \left(1 - \frac{x}{\delta} \right)^3 \quad (4.25)$$

In the case of these relationships, the thermal penetration depth (the maximum distance heat has penetrated into the material at a given time) is given by

$$\delta(\tau) = \sqrt{12\alpha_s t} \quad (4.26)$$

In addition, since thermal conductivity varies linearly with temperature, it is defined with a temperature coefficient β by *Eckert and Drake* (1987) as

$$\alpha = \alpha_{ref} \left(1 + \beta \frac{v}{v_s} \right) \quad (4.27)$$

The transformed variable gradient at the surface and subsequently the surface condition itself can be solved from this by

$$\left. \frac{\partial v}{\partial x} \right|_{x=0} = -\frac{3}{\rho C} \frac{v_s}{\delta} = -\frac{q}{k_s} \quad (4.28)$$

$$v_s = \frac{q\delta}{3\alpha_s} = \frac{2}{\sqrt{3}} \frac{q}{k_{ref}} \sqrt{\frac{\alpha_{ref}t}{1+\beta}} \quad (4.29)$$

This, in combination with the cubic profile distribution, leads to an appropriate temperature solution given by *Eckert and Drake* (1987) as

$$T(x, t) = \frac{2}{\sqrt{3}} \frac{q}{k_{ref}} \sqrt{\frac{\alpha_{ref}t}{1+\beta}} \left[1 - \frac{x}{\sqrt{12\alpha_{ref}(1+\beta)t}} \right]^3 + T_{init} \quad (4.30)$$

This solution is not exact and can only provide approximate results. Nevertheless, the solution is reasonably accurate in most cases and can be used to evaluate the results obtained from the ablation model. Recall that thermal conductivity is the only material property allowed to vary with this particular approach, and it must vary linearly with respect to temperature. Therefore, the following conditions are used for comparison with the numerical solution results:

$q = 75900 \text{ W/m}^2$	$\rho = 1914 \text{ Kg/m}^3$
$T_{init} = 296 \text{ K}$	$C = 707.9 \text{ J/Kg/K}$
$k = 0.2477 + 3.1717 \times 10^{-4} (T) \text{ W/m/K}$	$t = 1, 2, \text{ and } 4 \text{ seconds}$

The comparison of discrete cell temperature values with the above analytical solution is shown in Figure 4.5. Unlike the previous validation scenarios, the numerical results do not exactly match the analytical results. Nevertheless, the error between these two solution methods matches error observed in with other approximate solution methods, and any inaccuracies are more likely due to the approximate

nature of the analytical solution than problems in the numerical implementation (*Eckert and Drake*, 1987). Consequently, it can be stated that the method utilized to vary thermal conductivity with temperature is correctly implemented. While this is a fairly specific result given the large number of other material properties that are functions of temperature, all temperature-dependent material properties are implemented using the same method. Therefore, it is reasonable to extend this confidence to all material property functions within the ablation model.

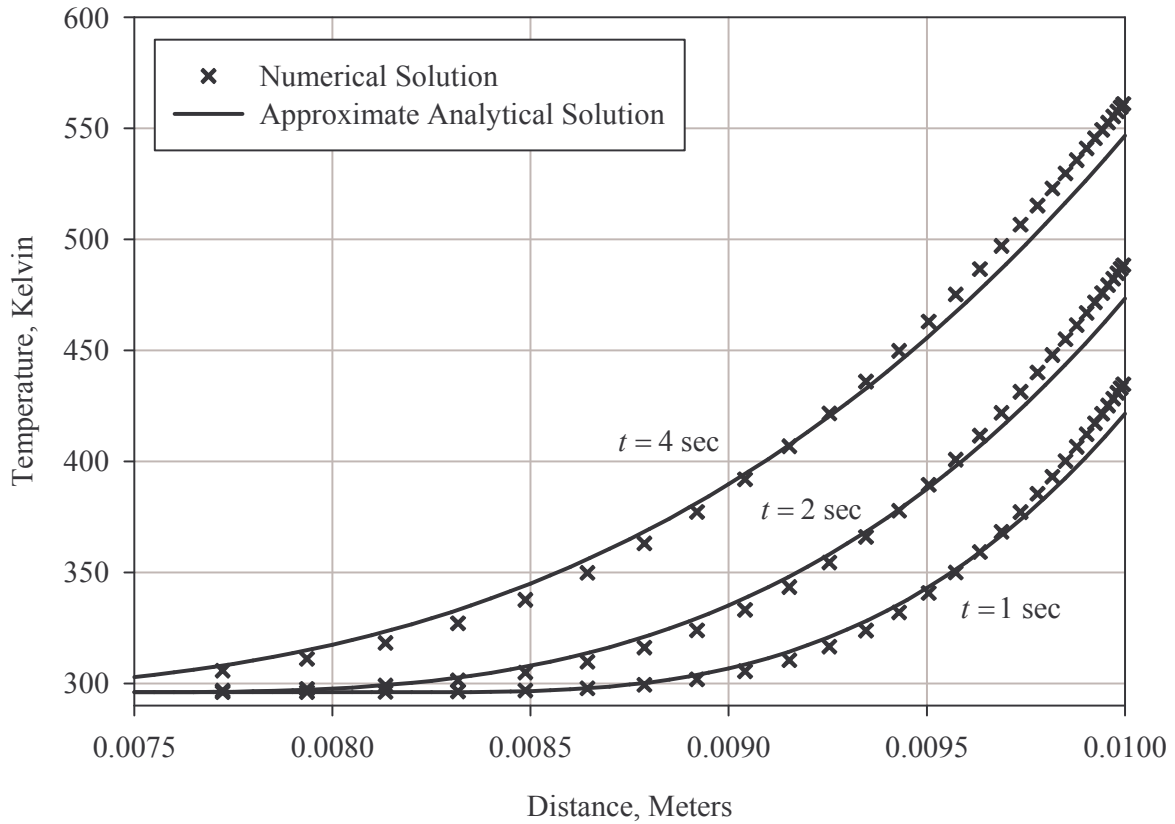


Figure 4.5: Temperature profile comparisons within the Teflon domain for the assumptions used in Scenario Four.

4.5 Scenario Five

The fifth trial scenario implements a modified solution to the familiar transient conduction relationship to validate the effect of the phase transformation interface and latent heat of fusion on the temperature distribution within the amorphous Teflon region. As in validation Scenario One, constant material properties, constant surface heat flux, and a semi-infinite domain are assumed to simplify the analysis. In addition, the crystalline base material is assumed to start just below the phase transition temperature to prevent thermal gradients from existing within the crystalline material itself. These

assumptions are necessary to allow a relatively straightforward analytical evaluation of transient heat conduction with the moving phase transition boundary present.

The solution derived from these assumptions resembles that obtained when investigating heat conduction with variable thermal conductivity and begins with Fourier's second law given by

$$\rho C \frac{\partial T}{\partial t} = \frac{\partial}{\partial x} \left(k \frac{\partial T}{\partial x} \right) \quad (4.31)$$

A similar variable transformation is applied but in this case is based on the relationship between temperature and the phase transformation temperature by

$$v = T - T_m \quad (4.32)$$

Conditions at the phase interface for a constant heat flux situation can then be represented by

$$v(X, t) = 0 \quad (4.33)$$

$$k \frac{\partial}{\partial x} v(0, t) = -q \quad (4.34)$$

$$\left(\frac{\partial v(X, t)}{\partial x} \right)^2 = \frac{H_m \alpha \rho}{k} \left(\frac{d^2 v(X, t)}{dx^2} \right) \quad (4.35)$$

The integrated heat conduction equation then becomes

$$\frac{d}{dt} \left[\int_0^X v(x, t) dx + \frac{H_m \alpha \rho}{k} X \right] = \frac{\alpha q}{k} \quad (4.36)$$

Since constant heat flux is assumed, this can be solved for the initial condition when no melt layer exists to yield

$$\int_0^X v(x, t) dx + \frac{H_m \alpha \rho}{k} X = \frac{\alpha q^2 t}{k} \quad (4.37)$$

In this case, X represents the location of the phase transformation interface relative to the exposed surface location, H_m represents the latent heat of fusion, A and B are constants of integration, and all other variables are as before. To solve this relationship, a parabolic temperature distribution

function is first assumed based on the boundary location. This function is given by *Eckert and Drake* (1987) as

$$v(x, t) = A(x - X) + B(x - X)^2 \quad (4.38)$$

The constants of integration can be determined by applying the necessary boundary conditions and using the assumed quadratic solution to yield

$$A = \frac{H_m}{2CX} [1 - \sqrt{1 + 4\mu}] \quad (4.39)$$

$$B = \frac{H_m}{8CX^2} [1 - \sqrt{1 + 4\mu}]^2 \quad (4.40)$$

Applying the constants of integration to the parabolic distribution defines a function that approximates the temperature distribution within the domain as

$$T(x, t) = \frac{H_m}{2CX} [1 - \sqrt{1 + 4\mu}] (x - X) + \frac{H_m}{8CX^2} [1 - \sqrt{1 + 4\mu}]^2 (x - X)^2 \quad (4.41)$$

This temperature distribution depends on the phase transition boundary location X which is given by

$$X(t) = \frac{\mu\alpha\rho H_m}{q} \quad (4.42)$$

Both the phase transition boundary and the integration constants depend on a constant μ . In this case, μ can be found by expanding equation 4.37 using equation 4.42 to yield

$$\frac{\mu}{6} [\mu + 5 + \sqrt{1 + 4\mu}] = \frac{q^2 t}{\alpha\rho^2 H_m^2} \quad (4.43)$$

The value of μ for a given scenario can subsequently be solved through iteration (*Eckert and Drake*, 1987). The analytical solution described above can be used to validate the numerical implementation of the phase interface boundary condition in much the same way as the analytical solutions in prior scenarios. Unfortunately, this solution can only provide approximate results similar to the analytical solution utilized in Scenario Four. Nevertheless, the analytical results remain fairly accurate according to comparisons performed by *Eckert and Drake* (1987). They can therefore be utilized for validation

purposes as was done in Scenario Four. First, identical assumptions and conditions are applied to the numerical model and the analytical solution.

$$k = 0.2477 \text{ W/mK}$$

$$\rho = 1914 \text{ Kg/m}^3$$

$$q = 75900 \text{ W/m}^2$$

$$C = 707.9 \text{ J/KgK}$$

$$T_{init} = 599.999 \text{ K}$$

$$t = 1, 4, \text{ and } 16 \text{ seconds}$$

The comparison between numerical results and analytical results for these conditions is shown in Figure 4.6. Clearly, the results do not match exactly, but they are well within the error expected with these types of approximate solutions which is sometimes given as no greater than 7% by *Eckert and Drake* (1987). These results imply that the implementation of the phase transformation boundary condition accurately reflects the physical processes associated with melting materials.

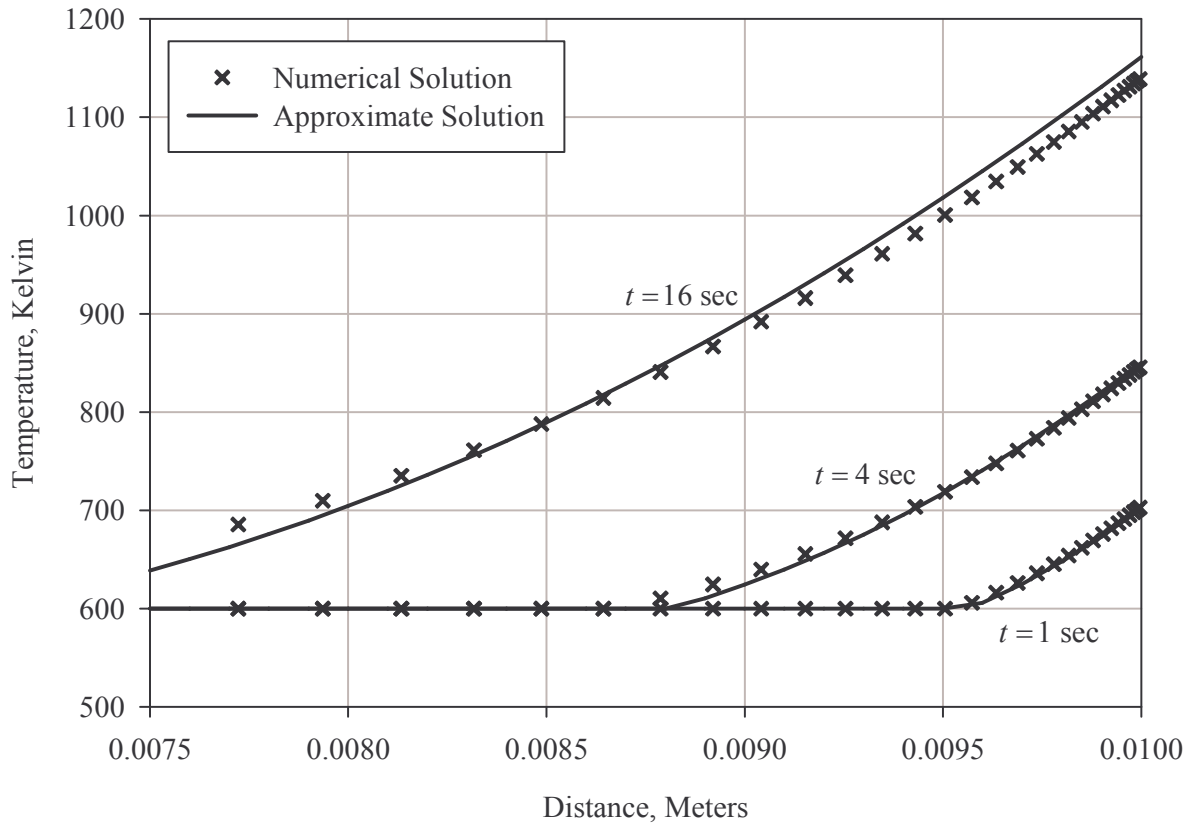


Figure 4.6: Temperature profile comparisons within the Teflon domain for the moving boundary assumptions of Scenario Five.

4.6 Scenario Six

The sixth trial scenario uses steady-state assumptions to validate the relationship between mass flux and the outer surface recession. This scenario assumes a semi-infinite single-phase domain with constant density, linearly variable specific heat, linearly variable thermal conductivity, and constant surface heat flux (*Kemp*, 1968). An approximate solution to this problem exists for these assumptions. Depolymerized mass flux is a strong function of temperature and can be approximated by integrating the molecular depolymerization rate over the entire domain to give

$$\dot{m} = A_p \int_{-\infty}^0 \rho_s \exp\left(-\frac{B_p}{T}\right) dx \quad (4.44)$$

Temperature in this case is assumed to be a linear gradient near the surface where $x = 0$ and b represents the slope gradient. Thus:

$$T = T_s (1 + b T_s x) \quad (4.45)$$

Differentiating with respect to x gives

$$\left. \frac{dT}{dx} \right|_s = b T_s^2 \quad (4.46)$$

$$T^{-1} = T_s^{-1} - bx \quad (4.47)$$

Applying this linear temperature gradient assumption to the governing mass flux relation and integrating yields

$$\dot{m} = \frac{A_p \rho_s}{B_p b} \exp\left(-\frac{B_p}{T}\right) \quad (4.48)$$

Since mass flux depends on the slope of the temperature gradient b , this can be evaluated by solving the conservation of energy over the entire semi-infinite domain (from the cool surface at $x \rightarrow -\infty$ to the hot surface at $x = 0$) by

$$\dot{m} (h_s - h_{-\infty}) = k_s \left. \frac{dT}{dx} \right|_s \quad (4.49)$$

Note that the enthalpy difference between these two faces is simply a function of the thermal gradient at the surface given by

$$bk_s T_s^2 = \dot{m} (h_s - h_{-\infty}) \quad (4.50)$$

From these relations, the temperature gradient reduces to

$$b = \frac{\dot{m} (h_s - h_{-\infty})}{k_s T_s^2} \quad (4.51)$$

Given the assumptions of this analytical technique, the enthalpy difference can be calculated by integrating the specific heat over the domain and adding the heat of depolymerization as given by

$$h_s - h_{-\infty} = \int_{T_{init}}^{T_s} C dT + H_p (T_s) \quad (4.52)$$

Solving this and substituting from above gives the following algebraic expression for mass flux:

$$\dot{m} = \sqrt{\frac{A_p \rho_s k_s T_s^2}{B_p (h_s - h_{-\infty})}} \exp\left(-\frac{B_p}{T}\right) \quad (4.53)$$

Since $\dot{m} = \rho_s v$, the surface recession velocity (v) can also be calculated by

$$v = \sqrt{\frac{A_p k_s T_s^2}{B_p \rho_s (h_s - h_{-\infty})}} \exp\left(-\frac{B_p}{T}\right) \quad (4.54)$$

The above solution is used to validate the numerical implementation of the depolymerization and surface recession process. These are only approximate analytical solutions for mass flux and ablation rate, but the results are fairly accurate even with changing internal properties. It should be pointed out that the validation of the numerical implementation with this analytical method depends on replication of steady state operation with numerical simulations. Unfortunately, given the reaction kinetics, this can be challenging to create because it is difficult to determine when steady-state operation will be reached. Nevertheless, it has been shown that the approximate time necessary to reach steady state operation is based on thermal diffusivity and steady-state surface recession velocity and is given by *Clark* (1971) as

$$t_{ss} = \alpha v_{ss}^{-2} \quad (4.55)$$

The time required to reach steady state operation cannot be calculated beforehand with this relationship since it depends on the steady state recession velocity, however steady-state operation can be verified if it is obtained. The operator must consequently perform some iteration to create a numerical simulation case with sufficient simulation time to reach steady state operation while maintaining the semi-infinite boundary assumption. This is a fairly straightforward process so it usually takes little time to determine the necessary duration. In this particular scenario, six ablation simulations with the following properties are used for comparison with analytical results.

$$\begin{aligned}
A_p &= 3 \times 10^{19} \text{ sec}^{-1} & C_c &= 6.46 + 10.5(T) \text{ J/KgK} \\
B_p &= 41769 \text{ K} & C_a &= 6.40 + 14.1(T) \text{ J/KgK} \\
\rho &= 2310 \text{ Kg / m}^3 & H_p &= 1.774 \times 10^7 - 2790(T) \text{ J/Kg} \\
k &= 0.1209 + 4.853 \times 10^{-4}(T) \text{ W/mK} & T_{init} &= 296 \text{ K}
\end{aligned}$$

These six ablation simulations use the following constant applied heat flux values

$$\begin{aligned}
q_1 &= 5.0 \times 10^4 \text{ W/m}^2 & q_2 &= 2.0 \times 10^5 \text{ W/m}^2 \\
q_3 &= 8.0 \times 10^5 \text{ W/m}^2 & q_4 &= 3.2 \times 10^6 \text{ W/m}^2 \\
q_5 &= 1.28 \times 10^7 \text{ W/m}^2 & q_5 &= 5.12 \times 10^7 \text{ W/m}^2
\end{aligned}$$

The numerical results and approximate analytical values for mass flux and surface recession rates are shown in Figure 4.7. The corresponding results are virtually identical and likely differ only due to the assumption of a constant temperature gradient in the analytical solution. This successful match is obtained by assuming non-convective heat flux, but similar results can be obtained if the heat flux is convective in nature. This is because the ablation rate depends only on material temperatures throughout the domain, and once steady-state ablation is achieved, these temperatures remain constant relative to the exposed surface location regardless of how the constant heat flux is applied. In any case, the accuracy of these results strongly implies that the depolymerization and ablation rate functions are correctly implemented and accurately represent the physical process.

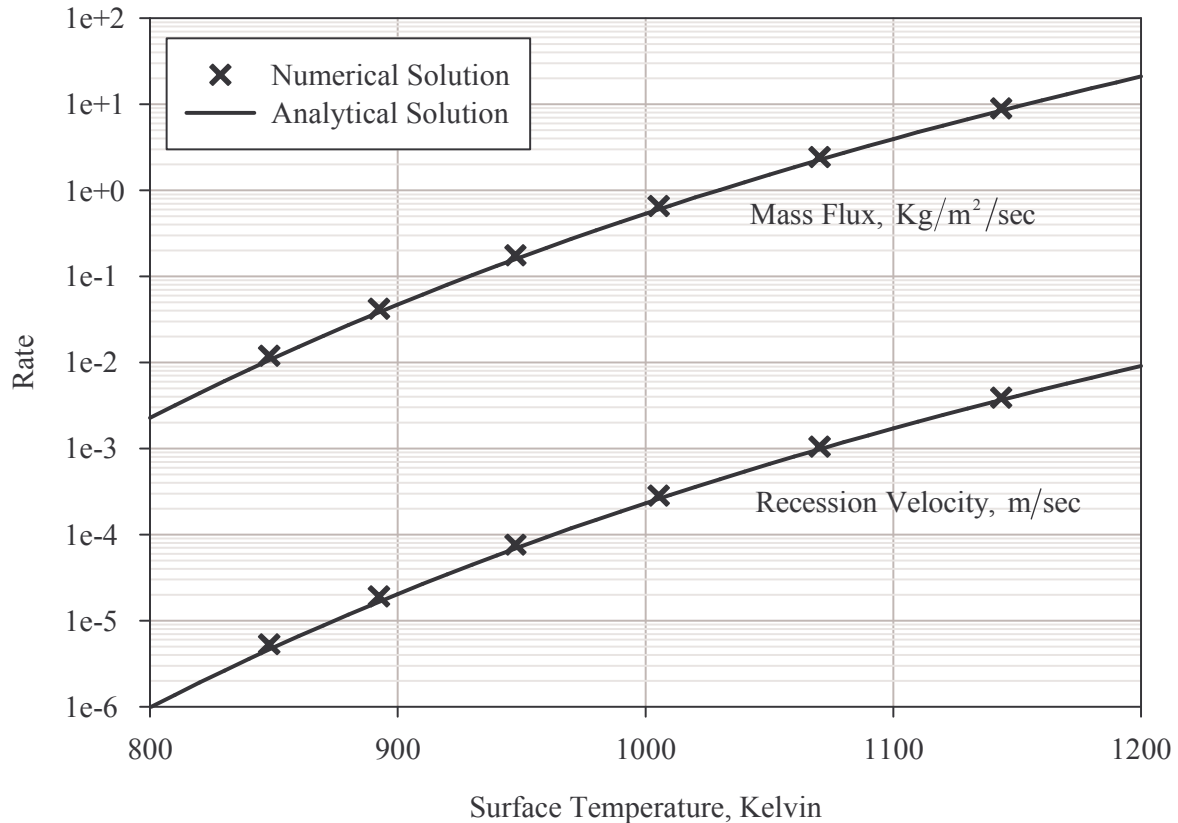


Figure 4.7: Steady-State mass flux and surface recession velocity comparisons for the assumptions and conditions used in Scenario Six.

4.7 Scenario Seven

The final trial scenario uses the sample PPT conditions outlined in Chapter Three to evaluate the effects of periodic grid regeneration and grid coarsening. As discussed in Chapter Three, grid coarsening can dramatically reduce computation time during periods when high heat fluxes and ablation rates are not present. Unfortunately, regeneration of the high-resolution grid from the coarse grid at the beginning of each cycle adds error because grid cell temperatures in the restored high-resolution grid are interpolated from those of the lower-resolution grid. Computation using a coarser grid will itself increase numerical error, so it is prudent to examine the significance of the errors generated by the combination of these two mechanisms. Since the degree of coarsening and the timing of the grid regeneration is controlled by the user, errors introduced by these mechanisms ultimately depend on the desired trade-off between computational time reduction and low error solutions.

To evaluate the error generated by a complete grid coarsening cycle and optimize the grid regeneration timing for the given type of problem (namely PPTs), the temperature profile 1 second after a single PPT pulse is computed using a fixed high-resolution non-uniform grid. This is compared with the

solution computed by regenerating the grid in sequentially coarser intervals at 60 microseconds and 200 microseconds following the pulse activation. These times for performing grid coarsening represent a good balance between solution error and computational time. The results of this comparison are shown in Figure 4.8.

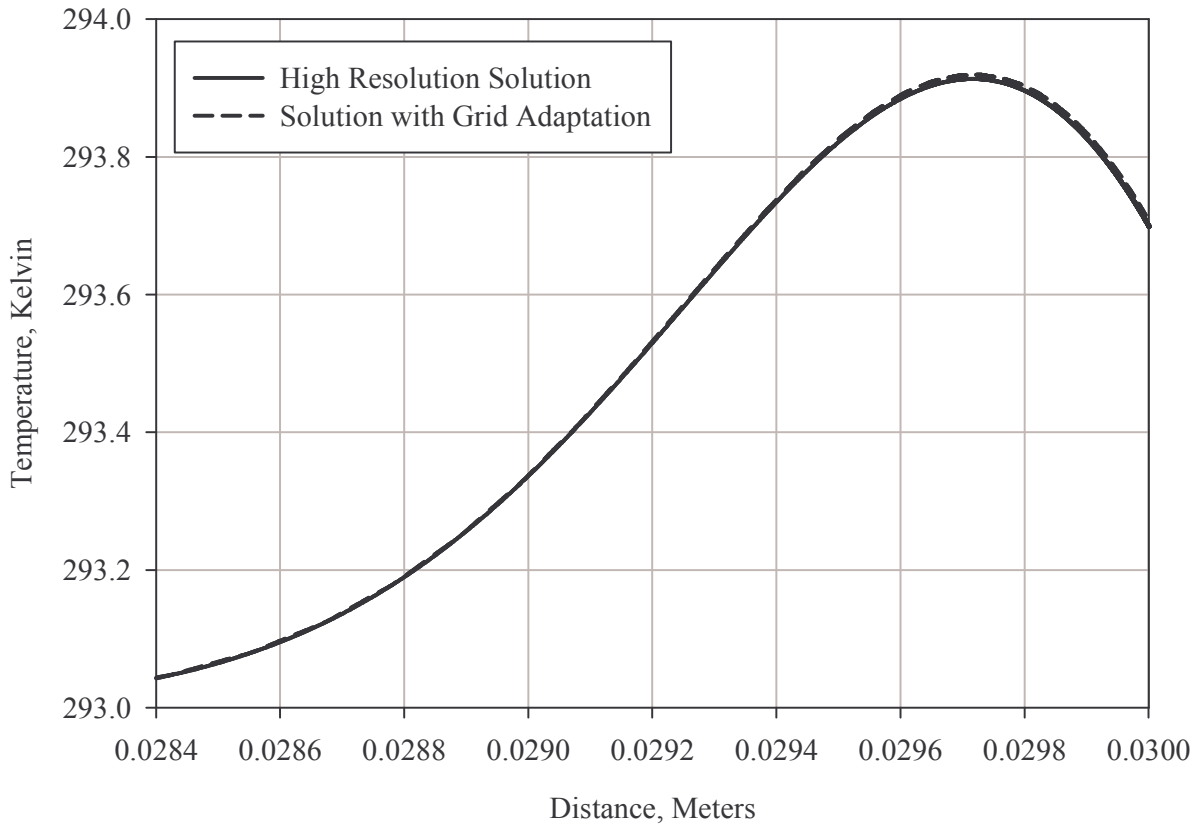


Figure 4.8: Temperature profiles near the exposed surface as computed using a non-adaptive high resolution solution and a solution obtained using grid adaptation.

The temperature profile obtained using grid adaptation is nearly indistinguishable from that obtained using the non-regenerating high-resolution grid. The maximum temperature error in this case is, in fact, less than 6.3×10^{-3} K and is obtained with a 3000-fold reduction in computer time. This is a remarkable reduction and demonstrates the power of grid adaptation implemented in a way that balances solution error and computational costs. The results of this tradeoff are problem-specific so a comparison should be performed for the general type of ablation problem to be investigated. This comparison will ensure that computational performance and solution error are in agreement with expected values.

Chapter 5

Material Property Analysis

Detailed knowledge of a material's properties is required to accurately compute ablation and thermal performance. This is particularly true for Teflon where the physical and chemical changes require additional parameters to accurately describe the ablation behavior. As outlined in Chapter One, these material properties are unfortunately not well known, primarily in the high temperature regime. This may seem surprising in light of the prior efforts spent studying Teflon ablation, but the complicated thermo-physical behavior make it exceedingly difficult to determine these properties and their dependence on temperature. Nevertheless, values do exist, as do thermocouple data from experimental analysis. The properties given in literature are compared and contrasted in this chapter to better characterize the differences in assumed material properties as well as their variability with temperature. The Teflon ablation model is also used to simulate ablation and thermal performance in several situations similar to experimental reference analysis to quantify the effects of different assumed material properties.

5.1 Material Property References

Teflon material properties are not well understood in high temperature regimes as discussed before, but this has not stopped numerous researchers from modeling Teflon ablation and thermal performance. In these situations, material properties from prior researchers are usually used or experimental analysis is undertaken to develop new values. The complicated behavior of Teflon tends to generate disagreement in certain characteristics associated with this more intricate behavior such as depolymerization frequency factor (an empirical constant used in determining rate of bond disintegration). However even more fundamental material properties such as density, specific heat, and thermal conductivity are not well agreed upon. In order to better characterize the discrepancy in these values, the material properties listed in several fundamental references are provided in Table 5.1.

Property \ Reference	Kemp (1968)	Clark (1971)	Pope (1975)	Holzknecht (1977)	Spanjers, et al. (1998)
A_p (sec ⁻¹)	3.00E+19	1.29E+19	N/A	3.10E+19	N/A
B_p (K)	41770	37333	N/A	38046	N/A
k_r (W/m/K)	0.2646	0.2485	0.3360	0.2319	0.1670
k_{mc} (W/m/K)	0.4121	0.3619	0.5377	0.4185	0.1670
k_{ma} (W/m/K)	0.4121	0.2453	0.3890	0.2512	0.1670
k_h (W/m/K)	0.5524	0.2472	0.2882	0.0976	0.1670
c_r (J/Kg/K)	955.6	708.3	711.0	977.0	1200
c_{mc} (J/Kg/K)	1274	1220	1213	1452	1200
c_{ma} (J/Kg/K)	1487	1476	1477	1296	1200
c_h (J/Kg/K)	1894	1537	1547	1484	1200
ρ_r (Kg/m ³)	2310	1933	2193	2169	2152
ρ_{mc} (Kg/m ³)	2310	2174	2172	1836	2152
ρ_{m2} (Kg/m ³)	2310	1740	1739	1650	2152
ρ_h (Kg/m ³)	2310	1086	1085	1448	2152
H_{p0} (J/Kg)	1468584	1577000	1770000	1548080	N/A
H_{p1} (J/Kg/K)	0	-4.603	-279	0	N/A
H_m (J/Kg)	0	58600	0	58576	N/A

Table 5.1: A detailed listing of Teflon material properties from four references shown relative to a more simplified listing from a fifth reference. The reference temperatures for each property are given in the Nomenclature section.

Clearly, a great deal of disagreement exists in many fundamental properties. The values listed are from only five data sets, yet many researchers draw material properties from these earlier references. It is interesting to note that more recent research does not necessarily use more precise representations of ablation behavior. As can be seen from Table 5.1, more recent references often ignore certain aspects of ablation behavior or temperature variability. While most of the material properties listed take into account some form of temperature variability, specific properties at specific temperatures are only one aspect of this variance. The three fundamental properties (density, specific heat, and thermal conductivity) from the four more detailed references are shown in Figure 5.1, Figure 5.2, and Figure 5.3 to provide a better representation of the discrepancy between these properties.

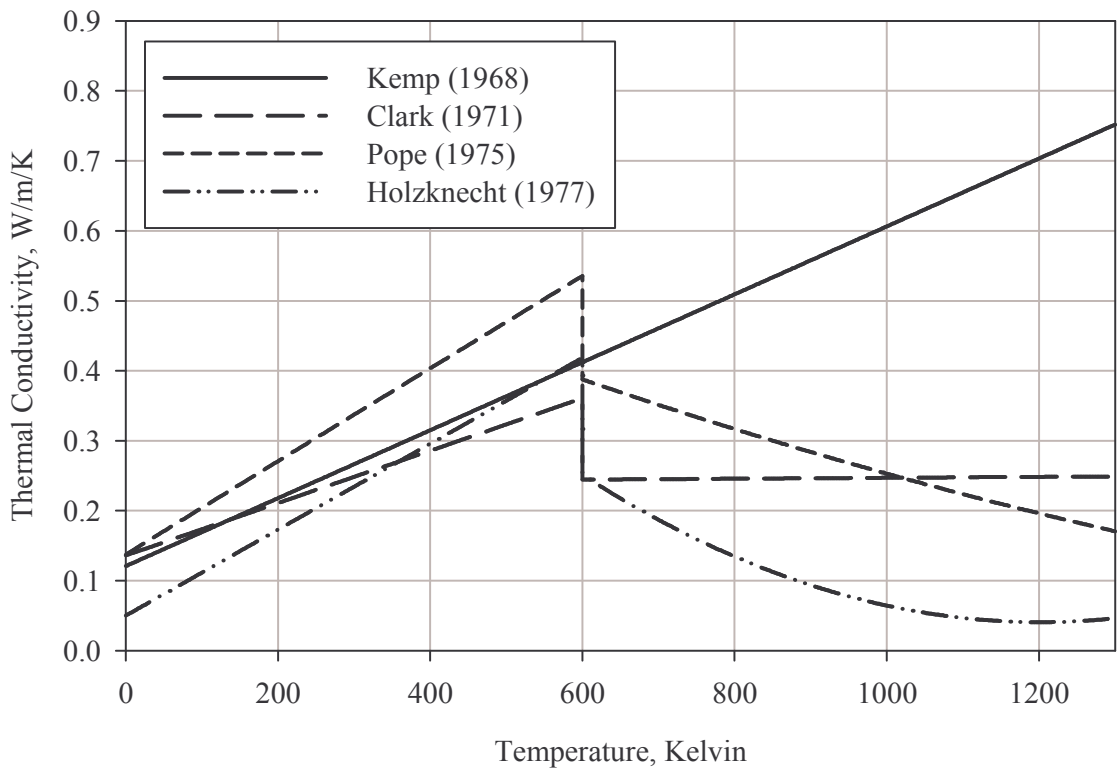


Figure 5.1: Thermal conductivity relative to Teflon temperature as described by four Teflon researchers.

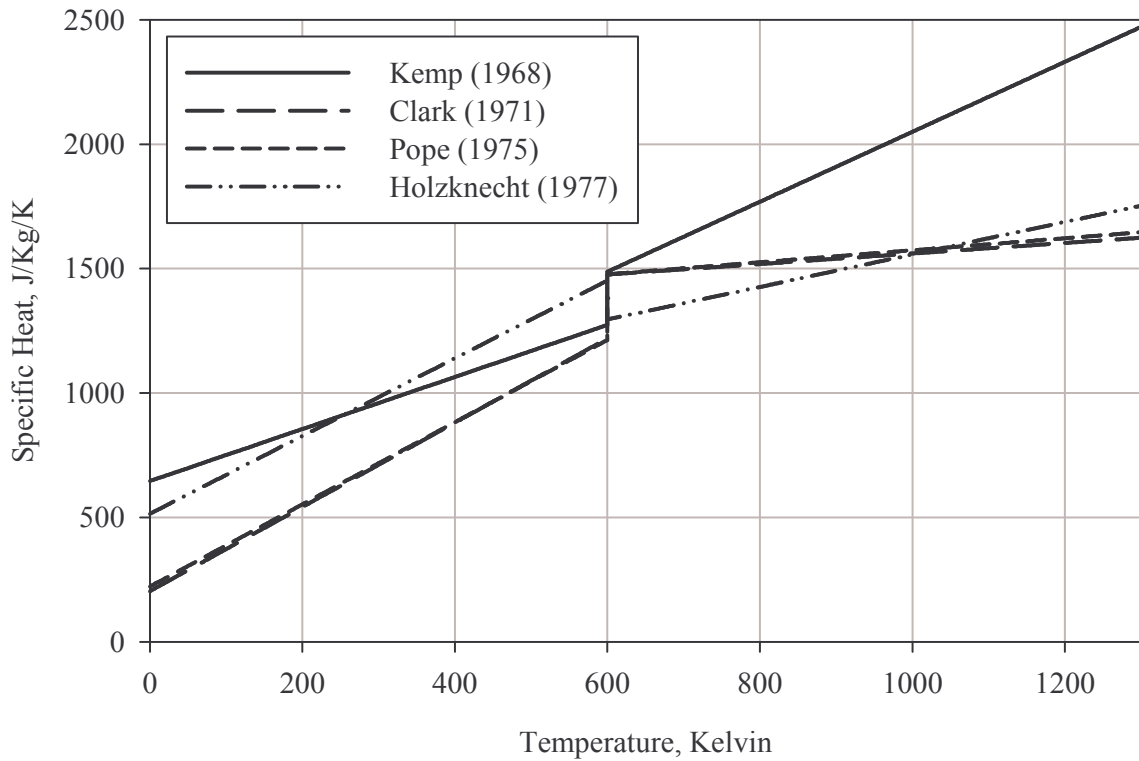


Figure 5.2: Specific heat relative to Teflon temperature as described by four Teflon researchers.

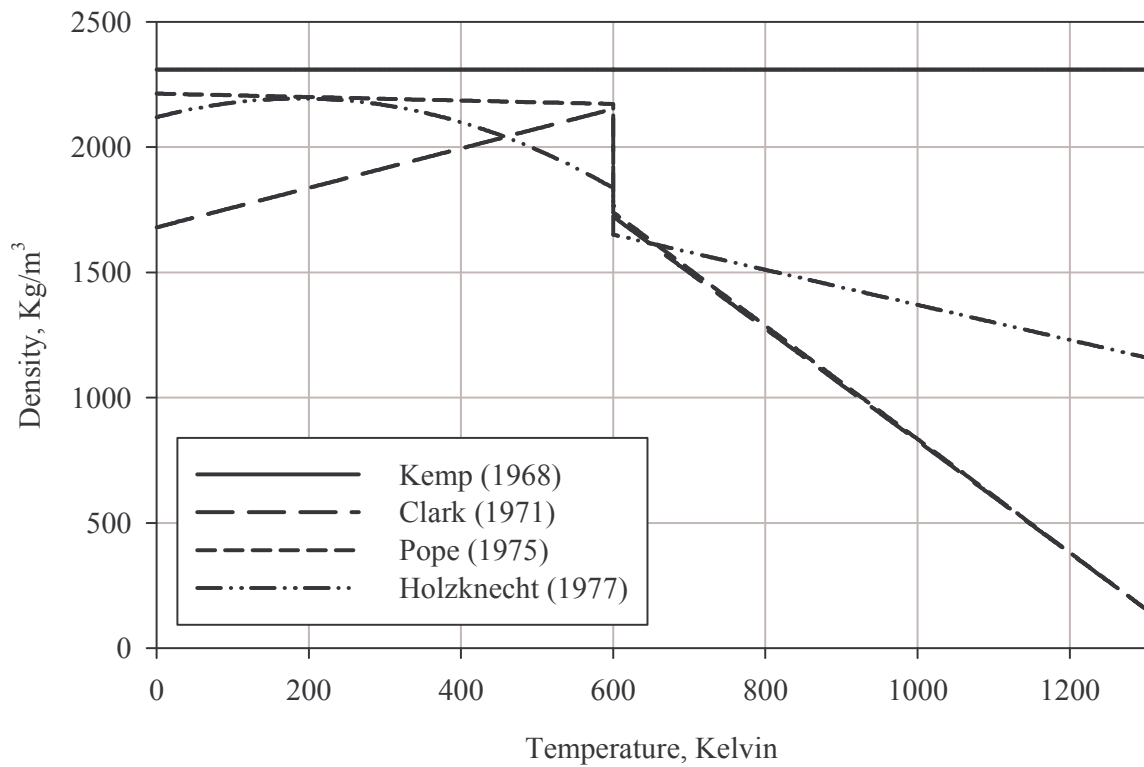


Figure 5.3: Density relative to Teflon temperature as described by four Teflon researchers.

5.2 Effects of Property Error

Clark (1971) provides the most extensive list of material properties to date as discussed in Chapter One and seen in Table 5.1. In addition to accounting for temperature variability in every fundamental material property, *Clark* provides an extensive set of error values associated with each material property. These error values are not based on variations between different researchers, but are self consistent based on the non-linear estimation work performed. To better ascertain the effects of material properties on ablation, the mean material properties reported by *Clark* are assumed as baseline simulation values, and the error values reported by *Clark* are assumed to account for all material property variability. “High” and “low” ablation cases are created from the error associated with each property. These cases are based on the effect of each material property on ablation rate. The “high” ablation case consists of material properties at the extreme error boundary that tend to increase ablation rate. Examples include high thermal conductivity, low specific heat, low density, and high depolymerization frequency factor. The “low” ablation case is constructed using material properties at the opposite extreme error boundary and thus have the opposite effect on ablation. These “high” and “low” property cases and mean (baseline values) are shown in Table 5.2. In addition to the properties discussed previously, non-

dimensional transpiration cooling factor values are also included in order to accurately compare simulation results with experimental data obtained by *Clark* in a convective environment.

Property \ Scenario	<i>Clark</i> High Case	<i>Clark</i> Mean Values	<i>Clark</i> Low Case
A_p (sec ⁻¹)	2.508E+19	1.29E+19	6.94E+18
B_p (K)	36878	37333	37672
k_r (W/m/K)	0.3958	0.2485	0.1752
k_{mc} (W/m/K)	0.5099	0.3619	0.2853
k_{ma} (W/m/K)	0.4308	0.2453	0.1497
k_h (W/m/K)	0.2821	0.2472	0.1901
c_r (J/Kg/K)	469.9	708.3	905.8
c_{mc} (J/Kg/K)	793.3	1220	1614
c_{ma} (J/Kg/K)	1118	1476	1941
c_h (J/Kg/K)	1269	1537	2572
ρ_r (Kg/m ³)	1424	1933	2232
ρ_{mc} (Kg/m ³)	2019	2174	2384
ρ_{m2} (Kg/m ³)	1483	1740	2140
ρ_h (Kg/m ³)	1076	1086	1207
H_{p0} (J/Kg)	1267971	1577000	1794680
H_{p1} (J/Kg/K)	-6.7	-4.603	-3.46
H_m (J/Kg)	58600	58600	58600
η (----)	0.3548	0.5043	0.7333

Table 5.2: Three material property cases that encompass the range of values described by *Clark* (1971).

Three ablation scenarios are constructed to observe the effects of these property extremes on thermo-physical behavior. These scenarios follow the first, second and sixteenth experimental ablation studies undertaken by *Clark*. The experimental conditions used in these three studies are listed in Table 5.3 and shown schematically in Figure 5.4. These particular cases are selected because they represent extremes in the heat flux conditions that have been tested experimentally and thus provide a diverse set of reference data. The recorded thermocouple response at a specific location in these experimental situations is replicated in the simulated ablation samples using virtual thermocouples as discussed in

Chapter Three. Samples 1 and 16 are simulated using a 300 node uniform grid because of the lower ablation rates (relative to PPTs) and the much longer time scales of ablation. A 400 node uniform grid is used in the simulation of sample 2 to obtain somewhat better resolution with the moderately higher heat flux. Numerical errors for these grid resolutions in this domain size are minimal. The resulting temperature response of the virtual thermocouples in each sample is compared with experimental results obtained by *Clark*. These comparisons are shown in Figure 5.5, Figure 5.6, and Figure 5.7.

Scenario Condition	Sample 1	Sample 2	Sample 16
q (W/m^2)	1.711E+06	3.860E+06	7.063E+05
L (mm)	0.7747	0.8001	1.0922
Experiment Time (sec)	1.8	1.4	3.0
x_{ploc} (mm)	0.6477	0.5461	0.8382
h ($\text{Kg}/\text{m}^2/\text{sec}$)	0.2663	0.4259	0.1382

Table 5.3: The conditions of three *Clark* (1971) experimental runs. These conditions are used in numerical simulation as well for comparison purposes.

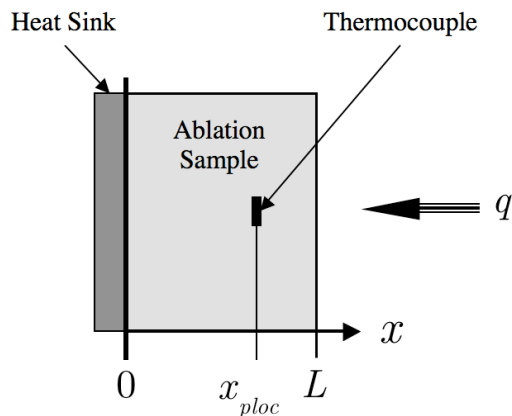


Figure 5.4: A general diagram of the experimental Teflon ablation samples and Thermocouple location undertaken by *Clark* (1971). The diagram is not shown to scale.

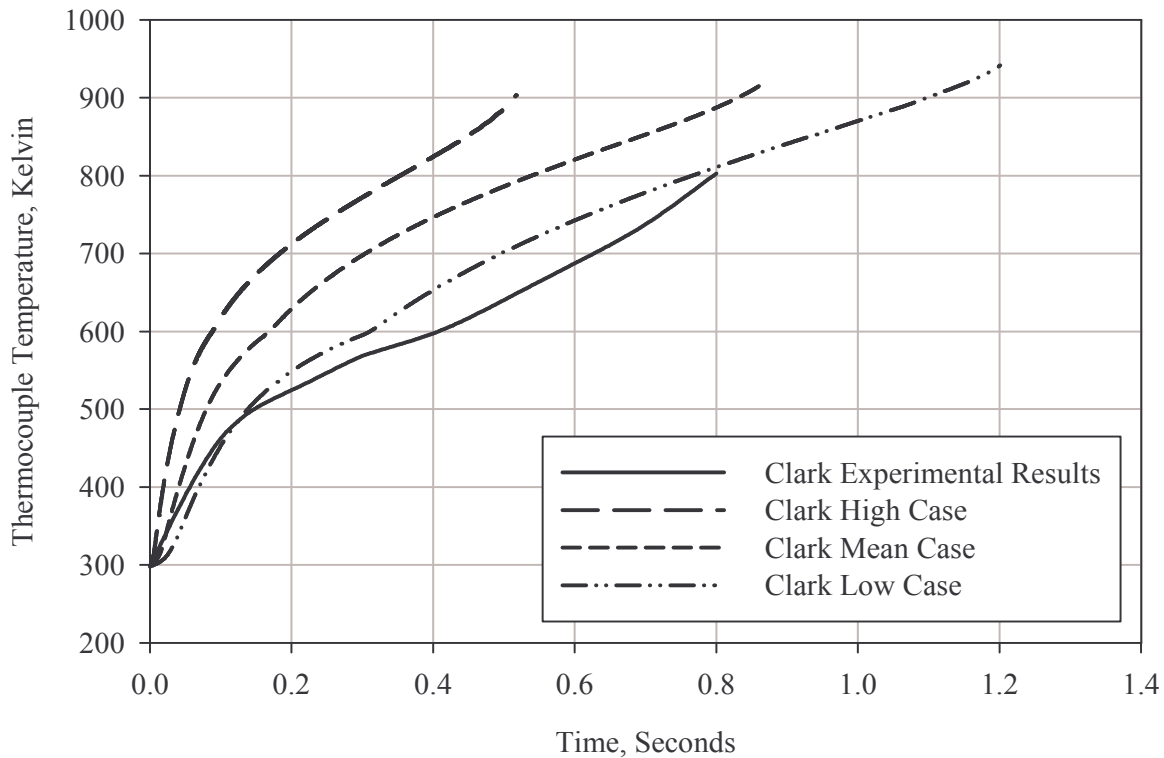


Figure 5.5: Thermocouple one response in *Clark* (1971) sample one. Experimental results are shown relative to simulated results for the range of material property values specified by *Clark*.

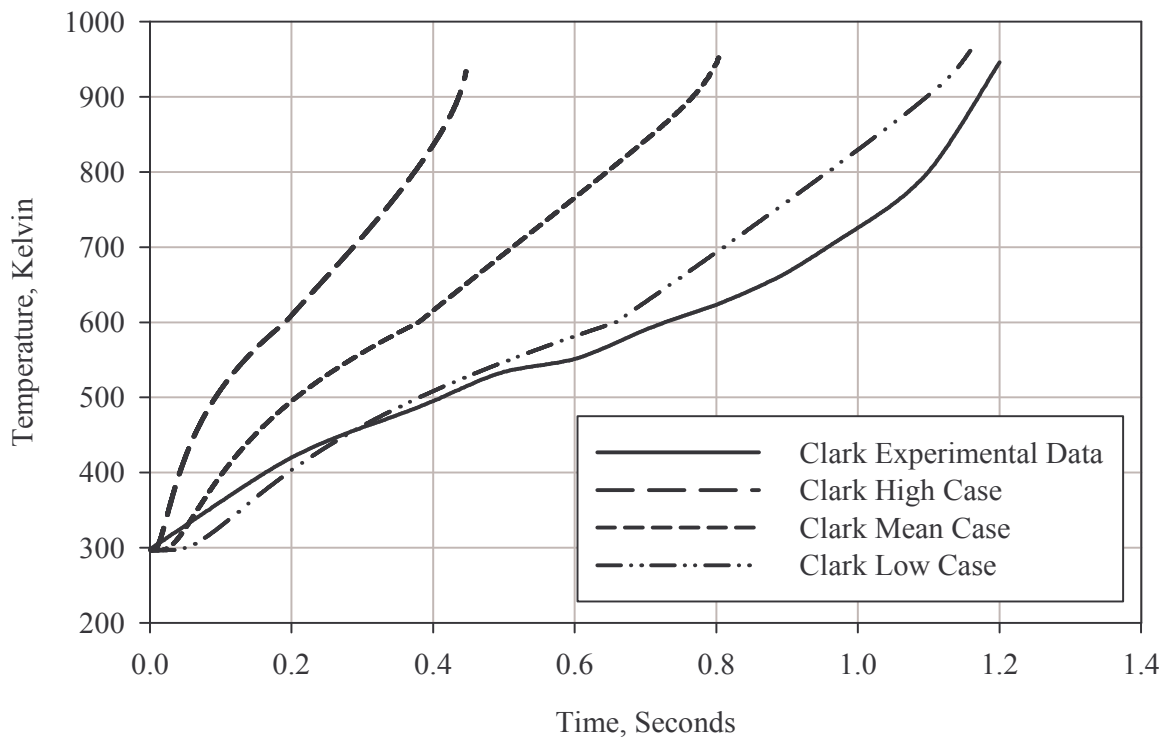


Figure 5.6: Thermocouple two response in *Clark* (1971) sample two. Experimental results are shown relative to simulated results for the range of material property values specified by *Clark*.

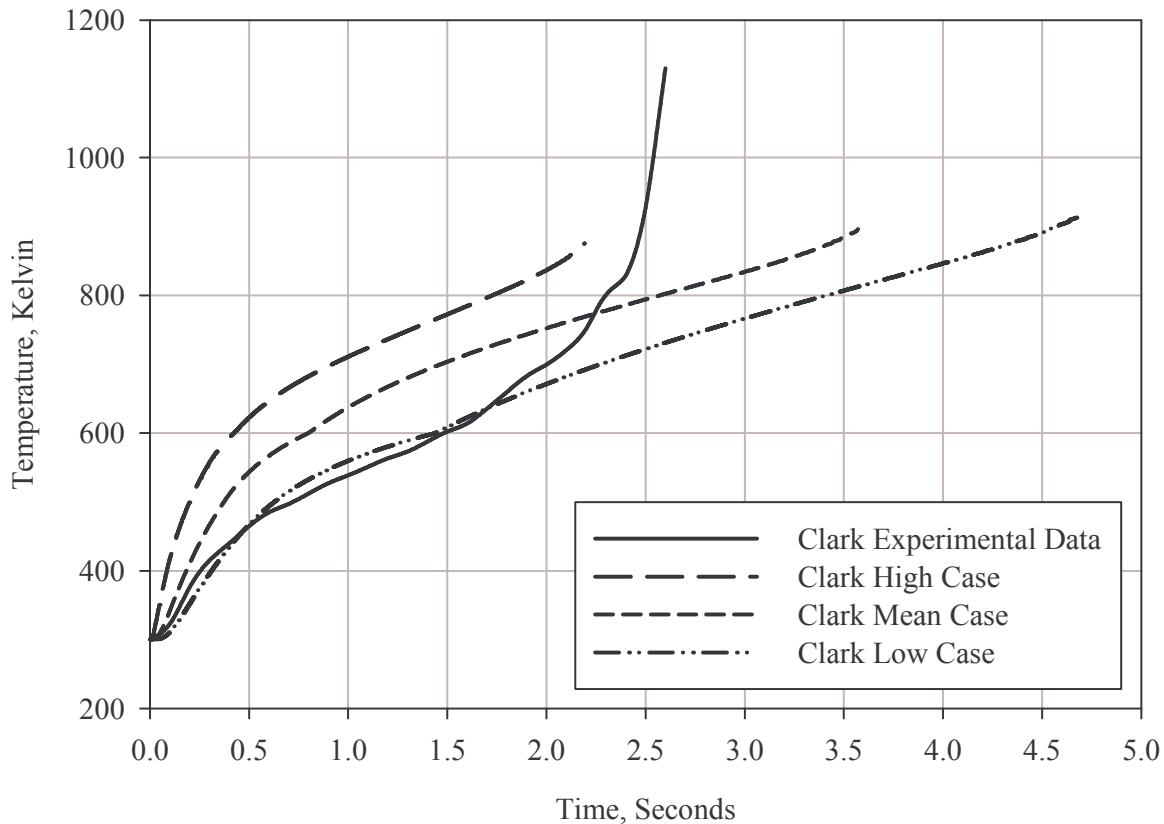


Figure 5.7: Thermocouple two response in *Clark* (1971) sample 16. Experimental results are shown relative to simulated results for the range of material property values specified by *Clark*.

Clearly, the errors in material properties create a fairly wide range of possible temperatures and ablation rates over time. Ablation rate data was not gathered in the experimental analysis conducted by *Clark* (1971), but its effect on thermocouple behavior can be seen in the timing of signal termination. In other words, thermocouples were destroyed and stopped recording data once the ablation surface reached the thermocouple location. This effect is mimicked in the ablation simulation. It can be seen from this that the ablation rate varies between the high material property case and the low material property case by a factor of 2 to 2.5. This margin of uncertainty is fairly high given the constraints placed upon thermal protection system design. Nevertheless, this ablation rate uncertainty does not change significantly with the five-fold difference in heat flux between samples. This suggests that the uncertainty may be fairly insensitive to heat flux conditions in this range of steady-state operating environments. Still, it is not certain a similar insensitivity exists in the extreme and transient environments of Pulsed Plasma Thrusters.

Aside from the ablation rate, it can be seen that the temperature response of the simulated thermocouples also has a very wide range. At some points in time, the temperatures differ by over 400 K depending on which material property extreme is used in which sample cases. The simulated temperature

response appears to more closely follow the experimental results when the low extremes of *Clark* material properties are considered. It is interesting such a similarity exists in all three scenarios, but this could simply represent a coincidence given the small sample size. If it is not a coincidence, then the range of material properties presented by *Clark* may not be an entirely valid representation of the Teflon used in the experimental measurements. More work would be necessary to conclusively verify this.

It should be apparent from these results that the range of possible thermal performance is extremely large, yet this range is based on the assumption that all material property uncertainty can be represented in the error values presented by *Clark*. This assumption is not completely accurate since properties used in other literature can vary even more widely than the extremes presented here. It is consequently difficult to obtain temperature or ablation results from computer modeling that can be exactly compared with experimental situations unless more accurate material properties are available. All results and comparison to this point also depend on the assumption that only one type of Teflon exists. In reality, there are multiple grades of Teflon Fluoropolymer with different material properties including Teflon AF, FEP, NXT, PFA, PTFE, ETFE and a very similar material known as Zonyl PTFE (DuPont, 2004). Teflon material properties in these different grades also depend significantly on the details of the manufacturing process in a manner similar to the dependence of metal properties on heat treatment processes (DuPont, 2004). Future investigation must be made to develop a more detailed and accurate set of high temperature material properties that take into account grades, manufacturing processes, and temperature variation.

Chapter 6

Pulsed Plasma Thruster Operational Analysis

The Teflon ablation model described in previous chapters is implemented in such a way as to be useful evaluating many different types of heat flux and ablation phenomenon. Nevertheless, the primary focus of the model is analysis of ablation in Pulsed Plasma Thrusters. Due to the nature of these thrusters, the ablation process depends on the heat flux profile and this can be difficult to evaluate or observe. Circuit current is more often used in plasma models to determine heat flux to the surface. Because these processes are coupled, however, mass flux affects plasma properties as well. It is thus necessary to either implement a coupled ablation and plasma model, or use simplifying assumptions in the problem conditions to draw any complete comparison with an experimental setup. This work focuses primarily on the ablation process, so the latter method of analysis is used. This method of analysis makes exact quantitative comparison with experimental data difficult; however general trends and qualitative analysis remain possible. Four general PPT effects are investigated using this method. These include effects of long-duration firing on ablated mass and propellant temperature, effects of propellant temperature and heat flux duration on re-crystallization time and potential particulate emission, effects of variable heat flux on mass flux profiles and late-time ablation, and effects of material properties on PPT ablation rates.

6.1 Long-Duration PPT Pulsing

One of the many documented deficiencies of Pulsed Plasma Thrusters is changing behavior over the course of long-duration firing. These changes include mass utilization and propellant temperature distribution and have been well documented experimentally as outlined in Chapter One (*Spanjers, et al. 1998*). The one-dimensional ablation model developed is suited toward simulating entire PPT domains over the course of multi-pulse firing, so it is prudent to examine these experimental effects numerically to better grasp ablation behavior. To this end, the experimental conditions of the XPPT-1 used by *Spanjers et al.* (1998) are input into the numerical ablation model. These conditions include a pulse rate of 1Hz, a discharge energy of 20 Joules, an exposed surface area of 5.29 cm^2 ($2.3 \text{ cm} \times 2.3 \text{ cm}$) and an initial uniform propellant temperature of 0° C (273K). The mean domain length of 3 cm is used, and the simulation is run for 20000 pulses constituting 5.56 hours of pulsed operation. A 1 cm steel heat sink is also assumed to exist at the rear portion of the Teflon domain. This only represents an approximation of

the thruster structure heat capacity; but it should not significantly change overall ablation and heating trends. The exact characterization of the heat flux profile applied to the surface from the given 20 Joules is also not easy to ascertain, so four different scenarios are considered with constant heat fluxes applied for 1, 2, 5, and 10 microseconds. These time scales are characteristic of applied heat flux periods in PPTs but do represent a significant uncertainty.

To better compare the ablated mass and large-scale propellant heating trends in the simulated XPPT-1 with experimental data obtained by *Spanjers et al.* (1998), the amount of heat flux applied to the surface over the course of the constant profiles is scaled in each scenario to match an approximate ablated mass value at room temperature (293 K) of 20 micrograms. This represents a method of fitting certain aspects of initial conditions from experimental data to evaluate performance at later times numerically. This requires assumed constant heat fluxes of $7.18 \times 10^8 \text{ W/m}^2$, $4.72 \times 10^8 \text{ W/m}^2$, $2.72 \times 10^8 \text{ W/m}^2$, $1.81 \times 10^8 \text{ W/m}^2$ respectively which represent between 1.9% and 4.8% of the total discharge energy. The remaining energy in each case is assumed to dissipate through plasma heating, electromagnetic or gas dynamic acceleration, and radiation loss. Density, specific heat, and thermal conductivity are assumed to remain constant at the values specified by *Spanjers et al.* (1998) and listed in Chapter Five. All simulations are solved using a 400 node grid with a transformation power of 4 to group the majority of nodes near the surface. In each, the grid is regenerated each pulse cycle at 60 microseconds and 200 microseconds from the start of the pulse to improve computational speed.

The results of these simulations for the different scenarios are shown in the next three figures relative to experimental XPPT-1 results obtained by *Spanjers et al.* (1998). Figure 6.1 shows simulated mass ablated per pulse for each heat flux case relative to the long-duration pulse number. Figure 6.2 shows temperature profiles in the Teflon domain at specific points in the pulse cycle for the 2 microsecond scenario. Figure 6.3 shows thermocouple response at four locations in the Teflon domain during the initial 5000 pulses in the 2 microsecond scenario. The results do not exactly match the experimental data, but the significant uncertainties in the problem inputs as discussed earlier only allow qualitative comparison of trends and these appear to match quite well. The actual residual heating effects appear to fall somewhere between those observed in the 2 microsecond and 5 microsecond constant heat flux cases.

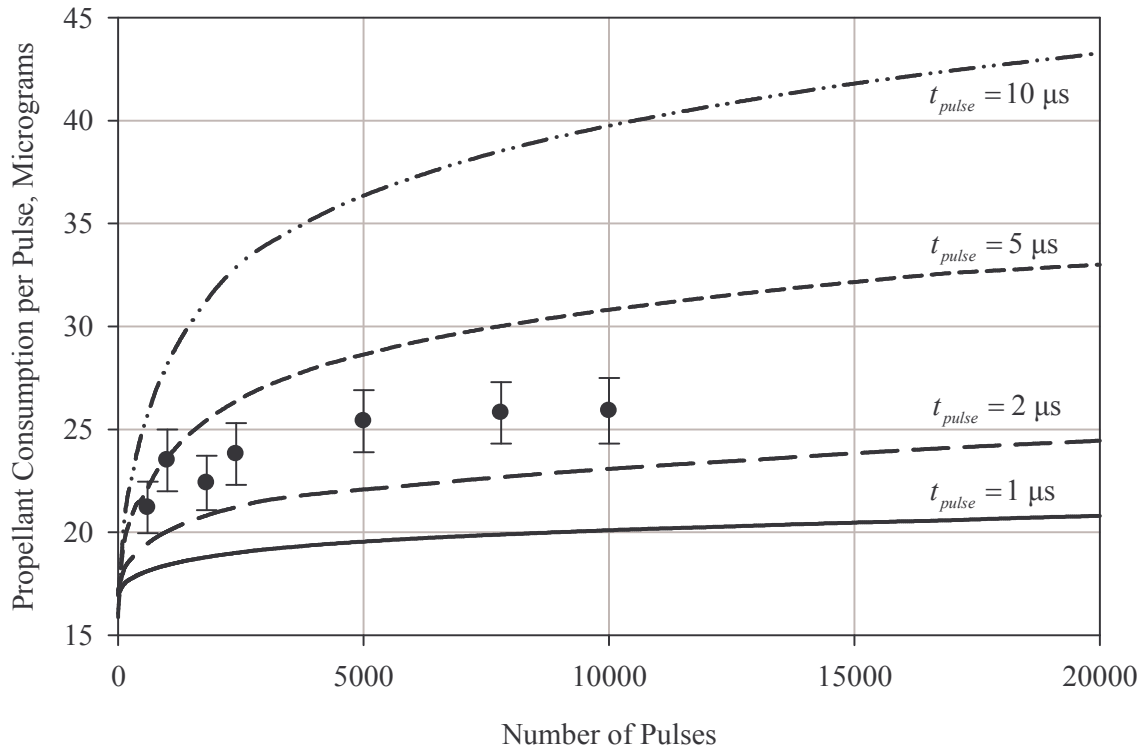


Figure 6.1: Mass ablated per pulse as a function of the number of pulses fired for the four different heat flux scenarios. Experimental data is shown in order to compare general trends (Spanjers, et al. 1998).

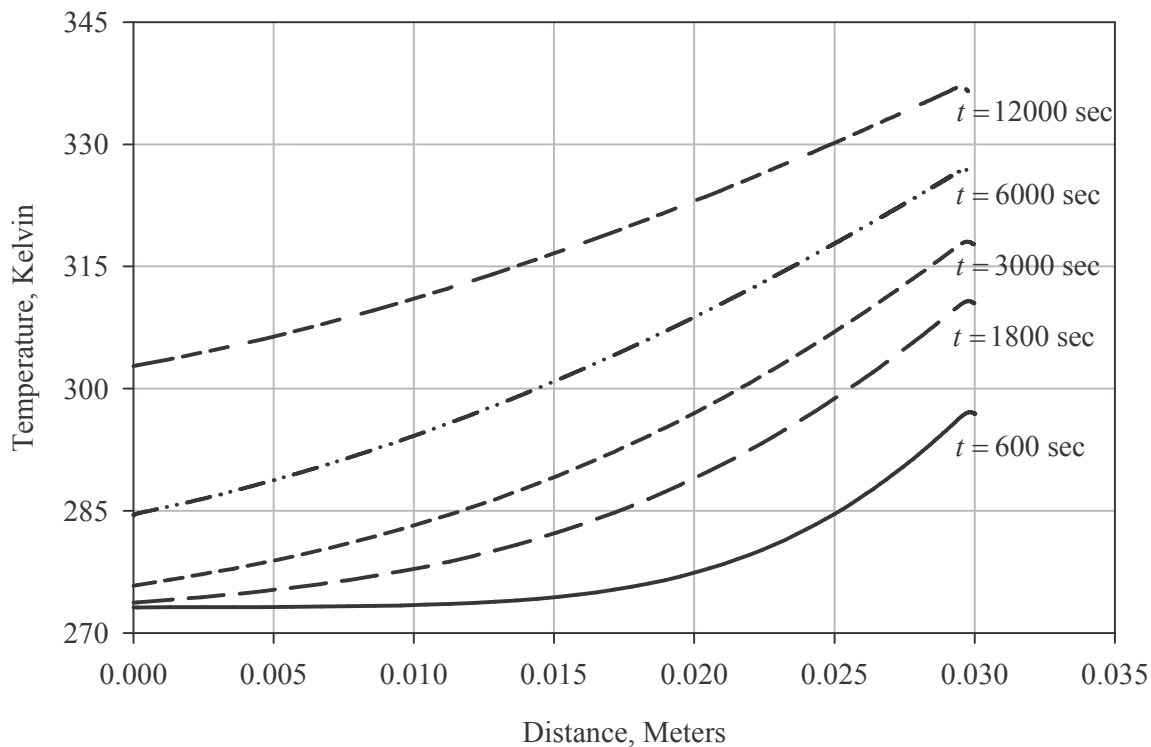


Figure 6.2: Temperature distribution within the PPT at different points in time during the firing sequence for the 2 microsecond heat flux case.

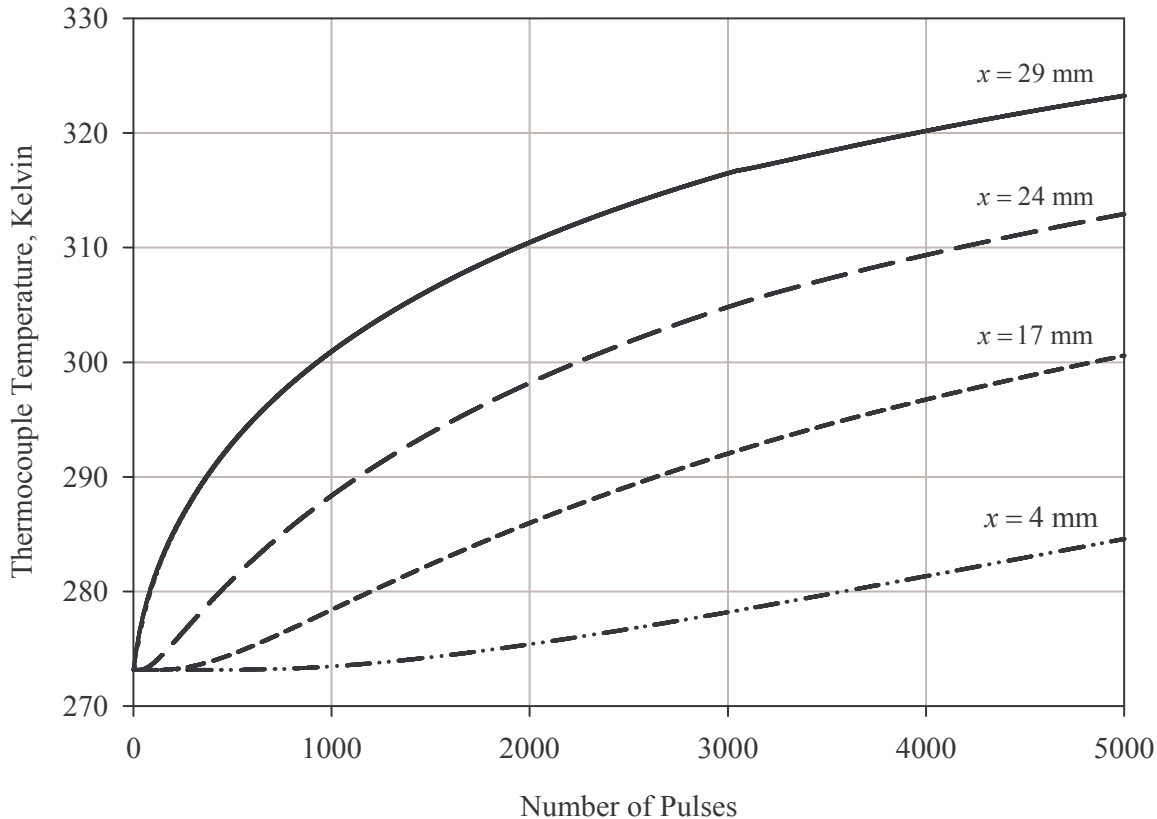


Figure 6.3: Thermocouple response at four locations within the 3 cm PPT during long-duration firing of the 2 microsecond constant heat flux case.

Clearly the amount of mass ablated per pulse increases rapidly as the initial temperatures near the Teflon surface rise. As the temperature changes in the entire Teflon domain slow from an initially rapid increase toward a slower increase, the ablated mass per pulse behaves in a similar manner. It would appear that the direct correlation between propellant temperature and mass ablated per pulse is accurate and that mass ablated per pulse changes significantly less when large-scale temperatures in the domain cease to change as rapidly as well. The decrease in residual heating rate at later points in firing is likely caused by the fact that, as greater amounts of the residual heat are added to the propellant during a pulse, the increased propellant temperatures cause more of this heat to be lost through other means. In these scenarios, a heat sink is assumed to absorb heat at the rear portion of the domain. The heat sink is “finite” in the sense that none of the energy absorbed from the Teflon is dissipated out of the heat sink. All thermal energy absorbed is retained. Consequently, the heat sink will show a continual increase in temperature during simulation once thermal energy has initially penetrated through the entire Teflon domain. In an actual thruster, this heat sink would not be completely finite as it would be coupled to any number of thruster structures thermally that would eventually radiate into space. This temperature rise would consequently reach a steady-state value eventually where all additional heat from a pulse would be

lost elsewhere. The plateau observed in experimental results obtained by *Spanjers, et al.* (1998) is likely caused by a large-scale steady-state temperature distribution in the propellant.

As discussed above, the general trends between numerical data and experimental results match fairly well, but significant uncertainties in the heat flux profile prevent a more quantitative comparison. To better investigate these uncertainties as well as obtain a better understanding of how propellant consumption varies with temperature, the heat flux scenarios are simulated in the XPPT-1 using the specified initial propellant temperature. The propellant temperature is then varied to evaluate the correlation between temperature and propellant consumption per pulse. This correlation is shown in Figure 6.4.

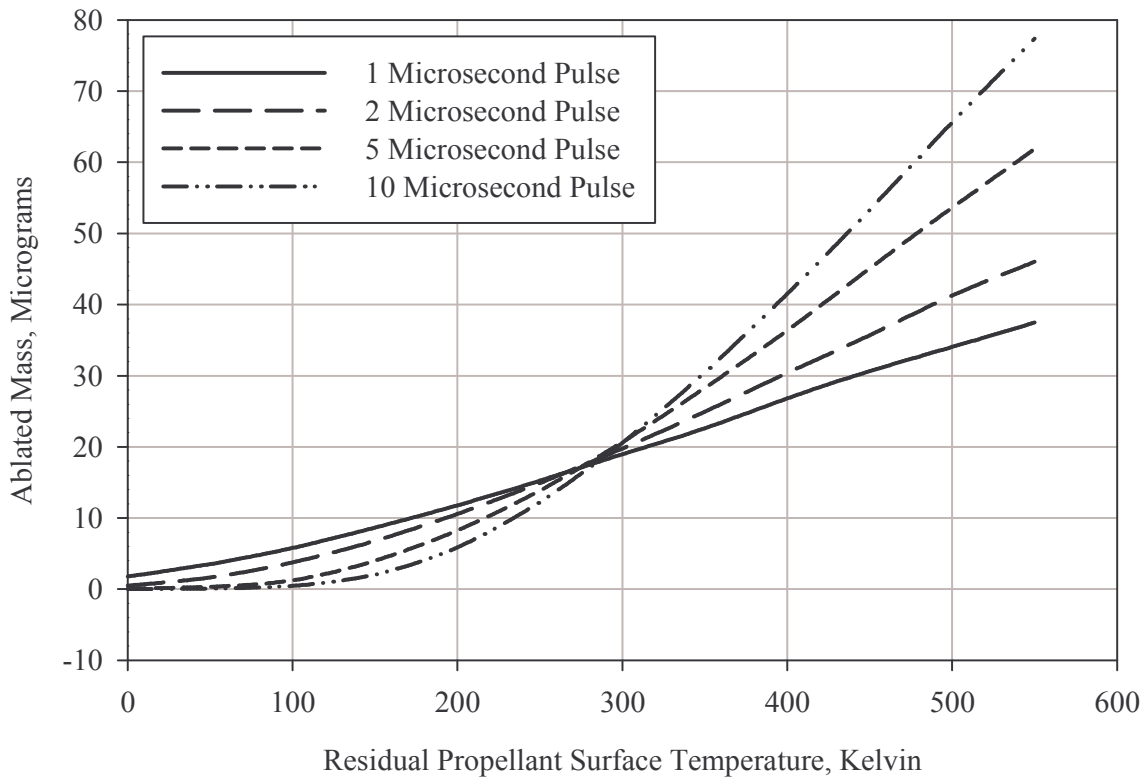


Figure 6.4: Propellant consumption per pulse as a function of pre-pulse surface temperature for four different discharge durations and heat fluxes.

Clearly, propellant consumption is basically a linear function of temperature in warmer conditions, but becomes less so the colder the propellant. In addition, it appears that propellant temperature has a greater impact on per-pulse consumption in situations with longer applied heat flux. Since propellant consumption directly affects thruster specific impulse and propellant temperature is observed to rise over long-duration firing, shorter pulses with higher applied heat flux per pulse appear to reduce the efficiency losses associated with increased propellant temperature. This benefit is insignificant

if the higher applied heat flux used in the shorter pulse scenarios cause more residual heating of the bulk material. To evaluate the residual propellant heating caused by these different discharge scenarios, temperature distributions within the Teflon propellant after a 3000 pulse 1Hz firing sequence are compared in Figure 6.5.

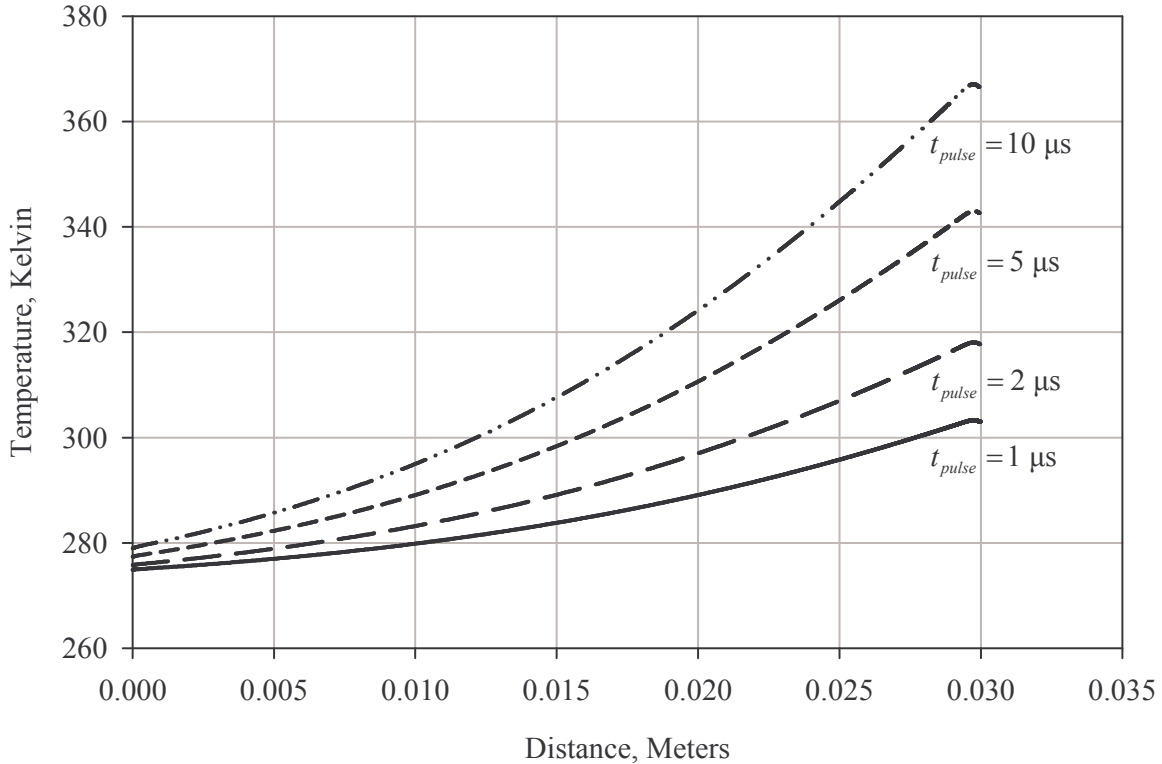


Figure 6.5: Temperature distributions in the Teflon propellant after 3000 seconds of firing at different heat flux pulse durations denoted in the plot.

It is apparent that, in the context of PPTs, residual heat is significantly more affected by the amount of time that a given heat flux is applied than by the amount of heat flux itself. The higher the discharge energy and the shorter the discharge time, the less residual heat is left in the propellant. This reduction in residual heat at higher heat fluxes can occur even if the discharge profile remains the same. Such an effect may appear counterintuitive, but it occurs because more of the material affected by the heat is removed due to the faster ablation rate. It consequentially appears that running a given PPT configuration at higher applied heat flux but shorter application time can reduce bulk heating and the effects of increased propellant temperature on propellant consumption. Considering the complexities of the circuit/plasma interaction, it is difficult to precisely control the heat flux to the surface in this manner. However such an improvement would increase PPT efficiency in long-duration operation.

An additional benefit to shorter discharge times and higher applied heat fluxes occurs because of the reduced total energy required to ablate a given amount material. As can be seen in Figure 6.6 for a $20 \mu\text{g}$ propellant discharge, increasing the time of applied heat flux increases the amount of total energy that must be applied to the surface in order to achieve the desired amount of propellant ablation. This effect is small, but it will nevertheless reduce the amount of energy that remains for acceleration of the plasma (through either electromagnetic or gas-dynamic mechanisms).

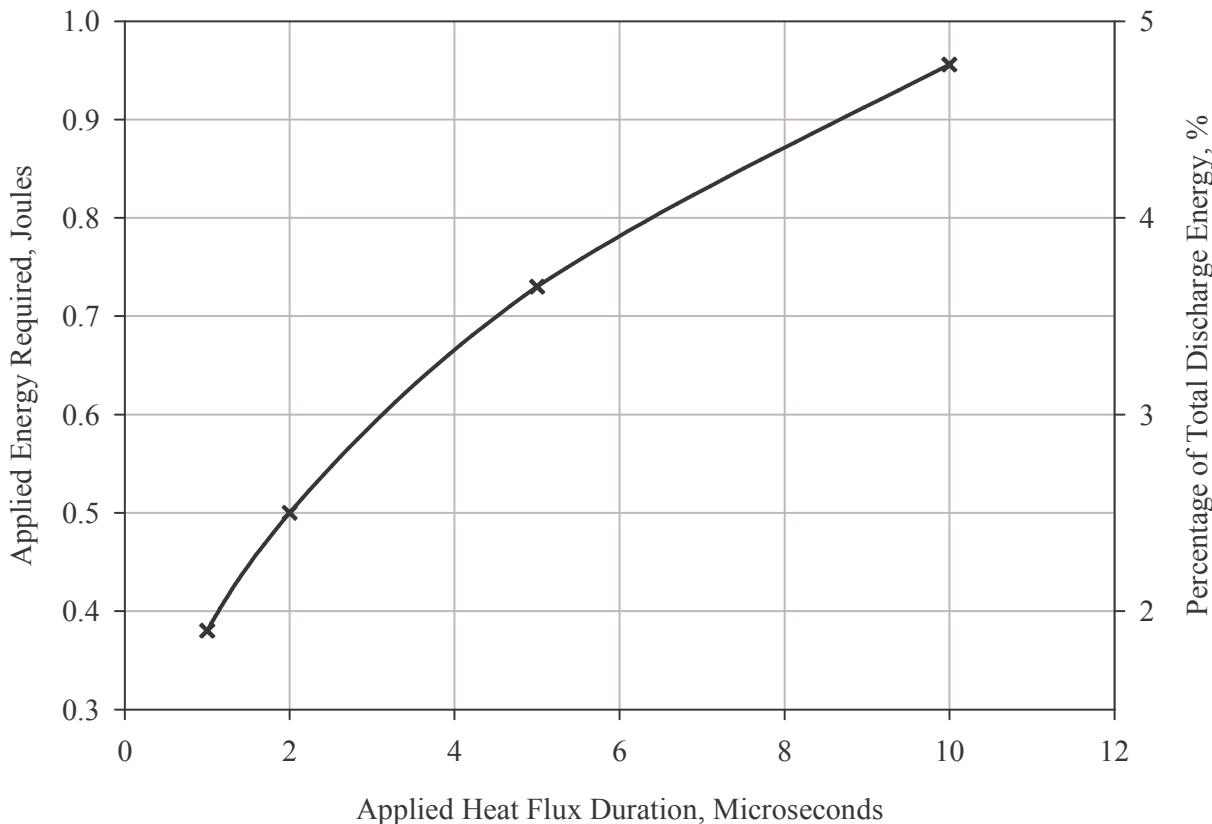


Figure 6.6: Total energy required to ablate 20 micrograms of Teflon in the simulated XPPT-1 as a function of the applied heat flux duration.

6.2 Particulate Emission

Particulate Emission (which occurs when large pieces of the Teflon material discharge) can account for a significant amount of useless propellant consumption. Particulate Emission generally takes place after a PPT pulse is complete, but it is a phenomenon different from conventional late-time ablation (depolymerization that continues to occur shortly after the pulse due to residual heat in the material). Particulate generation (sometimes referred to as macro-particle generation) is well documented experimentally as discussed in Chapter One (*Spanjers, et al. 1998*). Nevertheless, the exact mechanism

behind particulate emission is unclear. It is likely that large particulates can emanate from the Teflon only when amorphous material is present at the propellant surface. This is because the amorphous Teflon is in fact a liquid and while very viscous is still structurally weaker than the crystalline material. This should make it more susceptible to shearing or giving off large pieces when put under stress. If this is indeed the case, then the method of stress may come from the fact that molecular diffusion of the monomer through the material is fairly low, and as such any Teflon monomers generated significantly behind the ablation surface will remain there until the ablation surface reaches that location. In the ablation model, Teflon monomers are assumed to leave the surface once generated since the vast majority are created very near the exposed surface, however this assumption may not be completely accurate in situations with extremely high heat flux. Because the vapor pressure of monomer Teflon is fairly high, it is hypothesized that even a slight buildup of these monomers behind the ablation surface may provide the necessary stress to expel large parts of the structurally weak amorphous non-decomposed polymer. This mechanism is difficult evaluate numerically, however if this hypothesis is correct then particulate generation can be minimized if the amorphous re-crystallization time is minimized. Re-crystallization time as a function of pre-fire propellant temperature near the surface can be seen plotted in Figure 6.7 for the four constant heat flux assumptions outlined in part 6.1.

As can be seen in from these results, the time required to re-crystallize the amorphous Teflon layer ranges from 1 microsecond to over 1000 microseconds depending on initial heat flux duration and pre-pulse propellant temperature. Recall that heat flux in each of these cases is scaled to remove approximately 20 μg of total propellant during a discharge from propellant initially at room temperature (293 K). Heat flux exposure lasting longer than the maximum 10 microseconds shown would further increase re-crystallization time. Given this wide range, it is likely an amorphous surface layer remained in XPPT-1 when particulate emission was documented 100 microseconds following pulses triggered after over an hour of prior operation (*Spanjers, et al., 1998*). It is hypothesized that particulate emissions associated with each pulse would increase during long-duration operation of PPTs due to the increased residence time of the amorphous layer in the hotter bulk propellant. Lower propellant temperature, increased applied heat flux, or reduced discharge time should be used to reduce the amorphous Teflon residence time. It is hypothesized that decreased residence time would also produce a corresponding reduction in particulate emission. If this hypothesis could be verified experimentally, it would identify an additional performance metric coupled with propellant temperature, heat flux duration, and heat flux intensity.

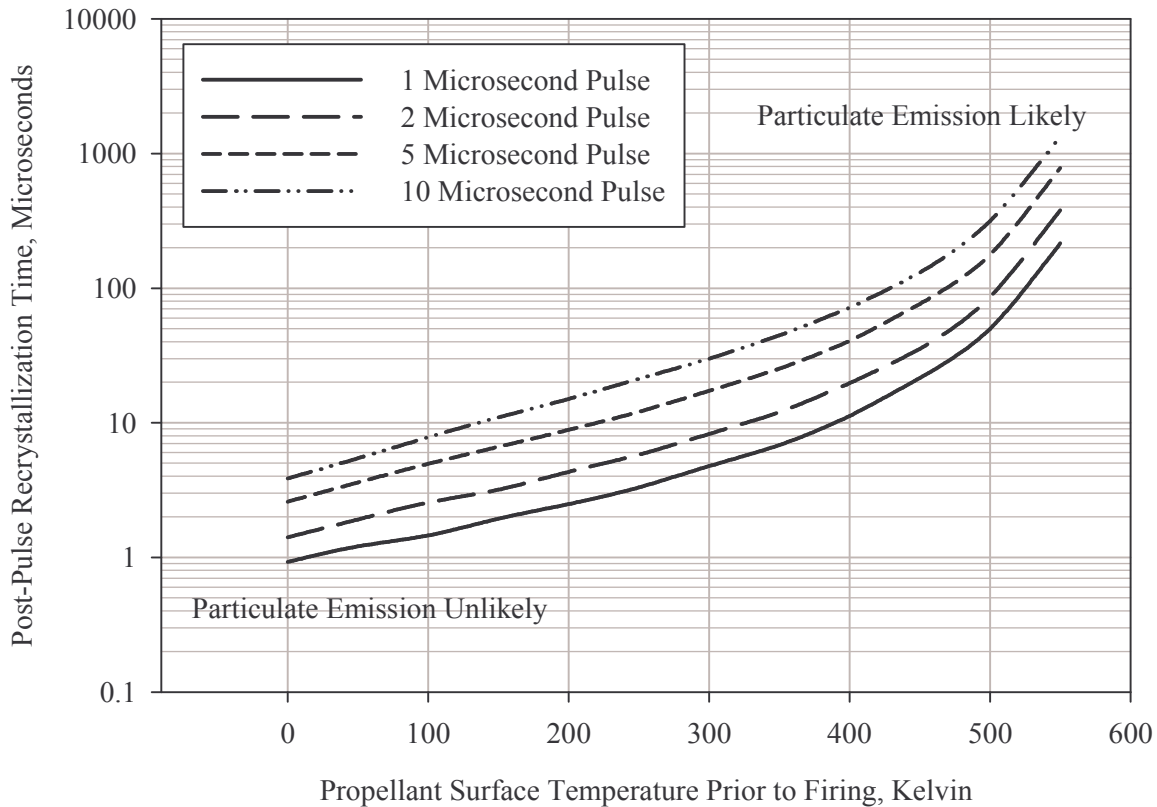


Figure 6.7: Time required to completely re-crystallize the propellant domain after a pulse fired at a given residual propellant temperature. The four PPT discharge scenarios outlined in 6.1 are used.

6.3 Effects of Variable Heat Flux

A great deal of PPT research has been conducted in an attempt to better understand late-time ablation. Late-time ablation, as discussed in Chapter One, is ablation that occurs after the primary portion of the pulse. This ablation contributes negligible thrust because of when it occurs, yet it consumes significant amounts of propellant. The primary effect of late-time ablation is an overall reduction in propulsive efficiency. To gain more insight into the rate of ablation during the application of heat flux, three variable heat flux scenarios are tested in a simulated thruster similar to the XPPT-1 discussed above. The heat fluxes used in these scenarios are scaled to produce a total ablated mass per pulse similar to the initial conditions demonstrated in the long-duration firing tests ($20 \mu\text{g}$ per pulse at 293 K). A grid with 600 nodes and a transformation power of 4 is used for these simulations to better resolve the ablation rate. The first heat flux scenario follows the 2 microsecond constant applied heat flux case described above. The resulting heat and mass flux are plotted in Figure 6.8.

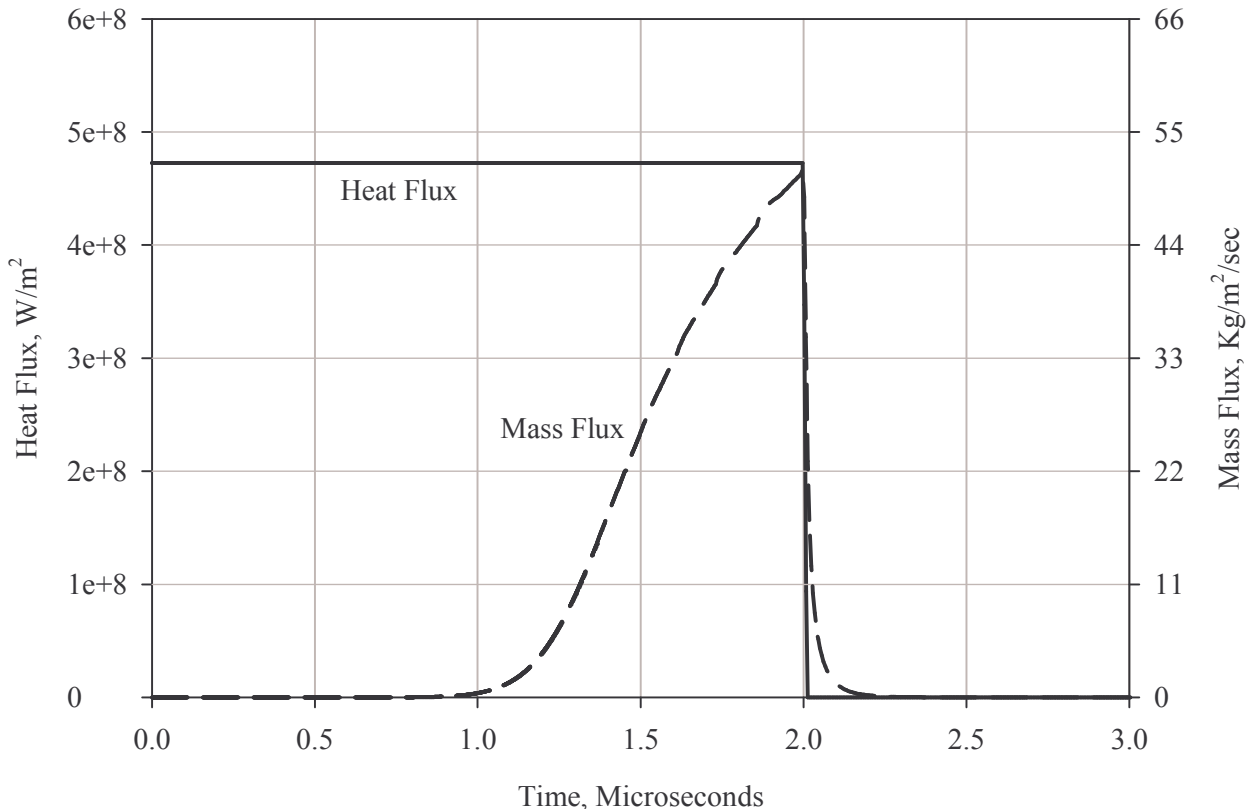


Figure 6.8: Mass flux shown relative to heat flux during the discharge in the simplified 2 microsecond constant heat flux simulation.

Clearly, very little mass flux ablates from the surface following termination of the applied heat flux. It is logical to conclude that instant termination of surface heat flux represents the ideal case for minimizing late-time ablation. Unfortunately, instant termination of heat flux is not realistic. It is more likely that heat flux rises briefly during ignition and increasing plasma density and then drops off gradually during the discharge as the current sheet propagates down the breach of the PPT. To better observe mass flux profiles in more realistic situations such as this, the second late-time ablation scenario uses variable conditions mimicking the heat flux profile more likely found in a PPT. This heat flux profile and the corresponding mass flux profile are shown in Figure 6.9.

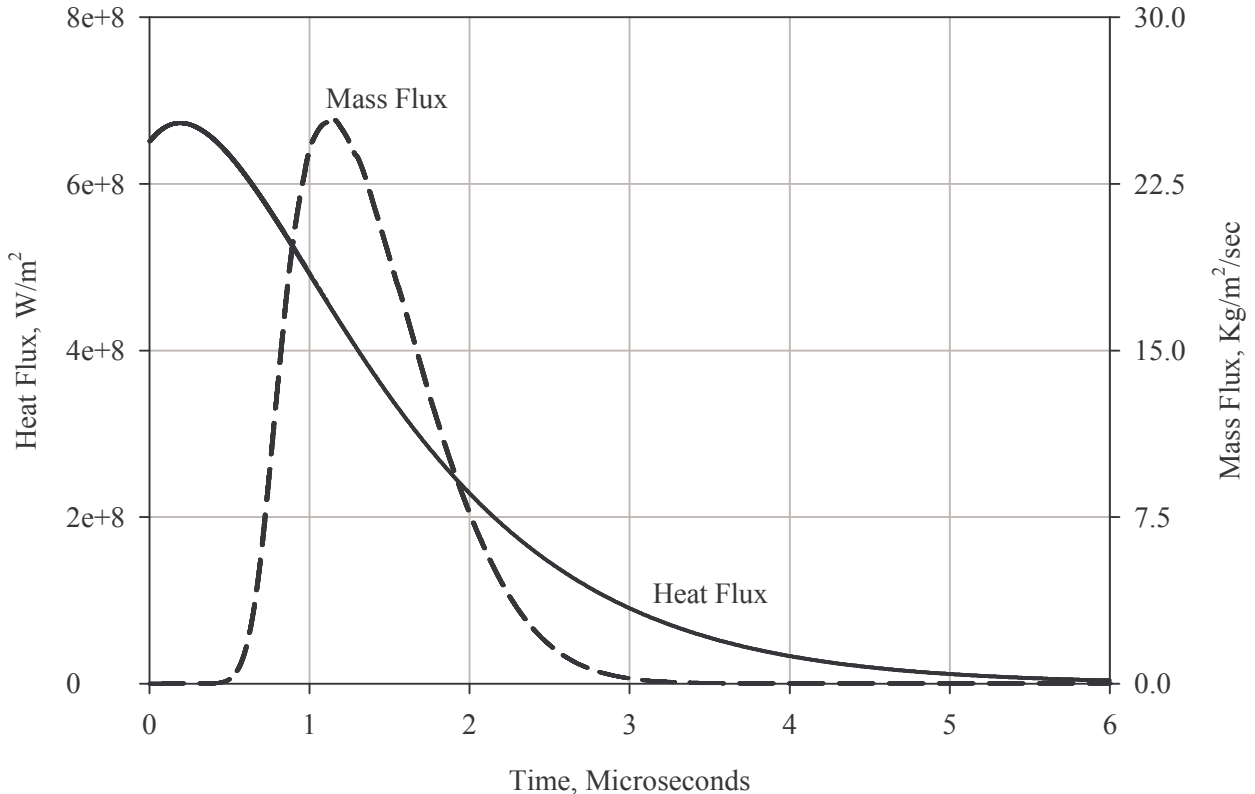


Figure 6.9: Mass flux shown relative to heat flux for a more realistic PPT situation. Scales are selected to show relative comparison between the two fluxes.

Some late-time ablation is present in this more realistic case since the majority of the propellant leaves the surface approximately one microsecond after the peak in surface heat flux. At this point in PPT operation, the current sheet may have propagated significantly far away from the propellant surface that the mass ablated at this point could not be entrained and accelerated with the majority of the plasma. Late-time ablation has been documented by *Burton and Turchi* (1998) and many others, but it is interesting to note that the ablation delay in this case does not appear very large. Removal of material is often observed experimentally to last much longer and in some cases continues to propagate downstream several milliseconds after firing (*Gatsonis, et al.*, 2001). The ablation model developed, however, considers all ablation to occur by long-chain polymer decomposition. It is therefore likely that late-time ablation observed significantly after the pulse occurs through other processes. Nevertheless, it appears in this case that delaying the peak in electromagnetic acceleration to approximately one microsecond following the peak in applied heat flux might allow much more of the ablated mass to become entrained in the electromagnetically accelerated plasma. This improvement would improve thruster efficiency. It is unfortunately unclear how such a delay could be implemented in actual devices.

While the heat flux and ablation profile shown in Figure 6.9 represent a more realistic scenario, they neglect the fact that PPTs often experience current oscillation during discharge due to capacitive – inductive coupling between the PPT circuit and the plasma. This can cause arc reformation (known as “re-strike”) and may result in a rippled heat flux profile. The third heat flux scenario attempts to replicate this rippled heat flux situation and is shown in Figure 6.10 relative to the mass flux profile.

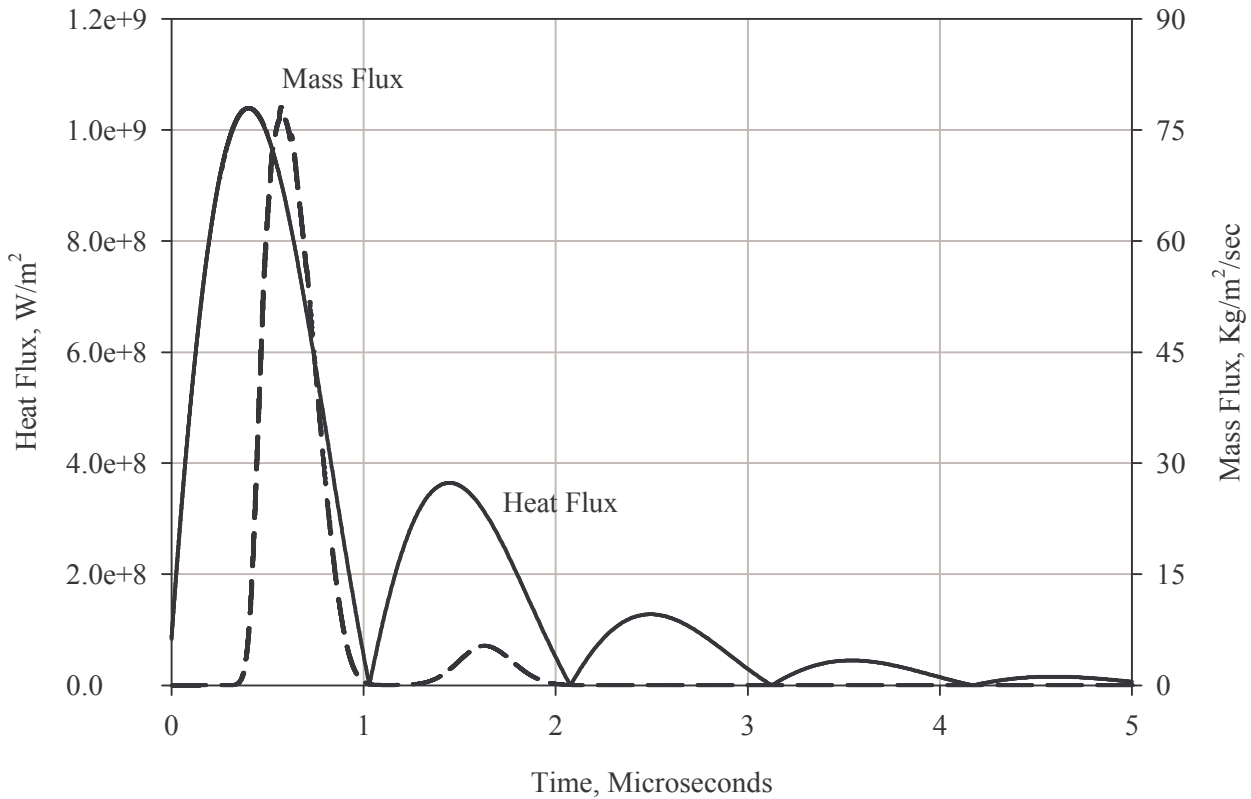


Figure 6.10: Mass flux shown relative to heat flux for a rippled application profile. Scales are selected to show relative comparison between the two fluxes.

The effects of late-time ablation are still present in this case, but it can be seen that the later applied heat flux has little effect on ablated mass. This represents wasted energy and simply adds residual heat to the Teflon domain. As documented earlier, this residual heat can increase total mass ablated in later firings by increasing the overall propellant temperature. Since this doesn't significant alter thrust, increased mass ablation in this context represents decreased efficiency. Additional residual heat can also dramatically increase re-crystallization times as documented earlier, and this can potentially lead to increased particulate emission. The rippled heat flux profile should be avoided if possible in order to minimize this residual heating.

It is apparent from these three PPT scenarios that slow heat flux termination tends to extend the mass flux profile. This is primarily because once heated, the amorphous Teflon needs little additional

heat flux to continue decomposition. The effect is apparent regardless of whether the heat flux terminates smoothly or terminates with residual ripples. Nevertheless, the rippled heat flux profile adds additional residual heat. Improving thruster efficiency requires increasing heat flux termination rate and minimizing circuit oscillations that could cause a rippled heat flux profile. It is also likely that delaying plasma acceleration even briefly for a given heat flux profile would allow more mass to become accelerated electromagnetically.

6.4 Effects of Variable Material Properties

The results generated to this point have all assumed constant material properties following those assumed by *Spanjers et al.* (1998) and listed in Chapter Five. In reality, material properties change as a function of temperature as well as material phase. These properties are unfortunately not well known in spite of the work by *Clark* (1971) to provide more accurate values through nonlinear estimation and experimental analysis. As discussed in Chapter Five, some of this uncertainty is because exact properties are strong functions of manufacturing methods, and many different grades of Teflon with different manufacturing methods exist (*DuPont*, 2004). The variability and relative uncertainties in high temperature Teflon material properties leads to different temperature distributions and ablation rates for general scenarios as shown in Chapter Five. Given the transient conditions experienced in PPTs, it is not obvious that similar uncertainties exist in PPT ablation behavior. If variable material properties have negligible effect on PPT performance relative to constant property assumptions, significant simplifications in PPT analysis may be possible in future work.

To determine the effects of different and variable material properties on the behavior of mass ablation from a PPT discharge, three scenarios are generated using the “high,” “low,” and mean material properties specified by *Clark* and outlined in Chapter Five. These scenarios use the assumed heat flux profile from Scenario Two in section 6.3. This heat flux profile was shown initially in Figure 6.9 and mimics a more realistic application in XPPT-1 than the brief constant heat flux assumptions used in sections 6.1 and 6.2. The scenarios are simulated on an 800 node non-uniform grid with a transformation power of 4. The resulting mass flux using the different assumed material properties is shown in Figure 6.11 along with the mass flux from the constant material property assumption shown initially in Figure 6.9.

It is apparent from these results that mass flux is heavily dependent on the assumed material properties. This is not unreasonable given the steady state ablation scenario results discussed in Chapter Five, but the outcome is more dramatic in this situation. Even with the assumption that all material property uncertainty can be accounted for by using the error values *Clark* reported, possible ablation rates

range from zero to nearly $40 \text{ Kg/m}^2/\text{sec}$. It appears from this that transient ablation situations such as PPTs may, in fact, be more sensitive to differences in material properties. As such, highly detailed characterization of thruster performance using computer models requires much more detailed knowledge of high temperature material properties than currently exist.

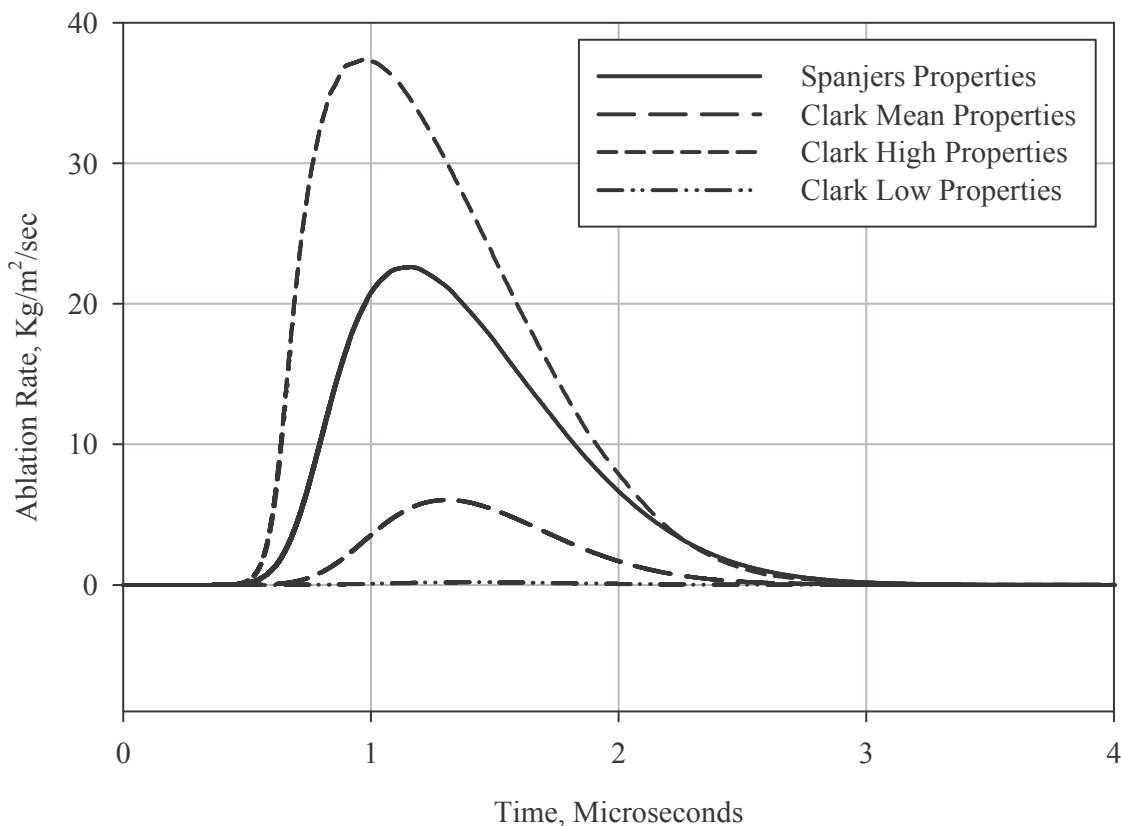


Figure 6.11: Differences in simulated mass flux profile due to differences in assumed material properties in an XPPT-1 thruster using a critically damped heat flux profile.

Material properties appear to be critical in characterizing ablation rates in thrusters, but it is interesting to note from the above results that the exact timing and overall profile of the ablation process apparently changes little between material property scenarios. In other words, widely variable material properties do not appear to dramatically affect when the peak in ablation rate occurs, and they do not appear to dramatically affect the relative rate on either side of this peak. Such a characteristic is surprising given the dramatic differences in thermo-physical response noted in Chapter Five. This has important implications for optimization of ablation profile and late-time ablation, and suggests that it may be possible to more accurately characterize general time-dependent pulse effects in the future without detailed knowledge of material properties.

Chapter 7

Conclusions

The evaluation and modeling of Teflon ablation in Pulsed Plasma Thrusters is a critical component of improving PPT performance, control, and efficiency. Significant effort has been expended focusing on general ablation of Teflon and the analysis and modeling of PPT plasma processes. Unfortunately, the existing set of PPT models often use simplified ablation assumptions that do not always correctly characterize the complex ablation behavior of Teflon. A model using a more accurate representation of the ablation process was developed to improve upon this. This model was divided into three stages to account for the different periods of ablation and heat transfer experienced in a Pulsed Plasma Thruster and the governing relationships were derived from those implemented by *Clark* (1971).

The first stage accounted for heat conduction in one-phase materials during the initial heat transfer period. The second stage accounted for heat conduction during the formation of the melt layer. The third stage accounted for heat conduction in two phase materials, depolymerization kinetics, mass flux, and surface recession. In addition, all stages accounted for the material property variation of Teflon.

Following development of the mathematical relationships, these relationships were discretized numerically using standard explicit finite difference techniques on a flexible adaptive grid system with uniform or non-uniform spacing. Non-uniform grids were generated using an algebraic mapping function suited to the types of ablation scenarios experienced in Pulsed Plasma Thrusters. Volume fractions were used within the grid system to account for phase interface and ablation boundary movement without requiring coordinate transformations. Additional numerical tools were used to allow easy input of transient heat flux as well as thermal analysis from virtual thermocouples. An example PPT scenario was subsequently used to verify that a scalable and flexible numerical implementation capable of analyzing a wide variety of ablation phenomenon had been achieved.

Once the governing relationships were implemented numerically, six simple heat-transfer and ablation scenarios with analytical or prior numerical solutions were established to validate the model. These scenarios tested the complete range of physical phenomenon represented including heat conduction, heat sink boundary conditions, heat flux boundary conditions, variable material properties, two-phase boundary movement, depolymerization mass flux, and surface recession. The comparison between simulation results and analytical solution results in each case demonstrated that an accurate

representation of the physical processes had been achieved. A seventh scenario was used to evaluate the accuracy of grid adaptation in an example PPT situation. The results of this scenario demonstrated that the grid adaptation technique could be used successfully to reduce required computation time in PPT analysis with little increase in solution error. Taken together, the validation and example solution results demonstrated that an accurate, flexible, and scalable ablation model was available for analysis of Pulsed Plasma Thrusters and general thermophysical Teflon ablation phenomenon.

7.1 Implications for Pulsed Plasma Thrusters

The numerical ablation model was used to evaluate certain aspects of PPT behavior. This analysis focused on trends in PPTs associated with ablated mass flux, residual heating, particulate emission, variable heat flux, and variable properties. Comparison of simulated and experimental data demonstrated that certain long-term trends could be replicated numerically. As PPTs are sequentially pulsed, the residual heat left in the propellant appears to increase ablated mass in later firings. It is interesting to see the increased propellant consumption is more dependent on the period of applied heat flux than the amount of heat flux itself. Higher heat fluxes applied over shorter durations tend to reduce the increasing propellant consumption per pulse found in later firings despite ablating the same amount of mass initially. This is caused by reduced residual heating and a reduced effect of any given residual heating on mass ablated per pulse. Higher heat fluxes applied over shorter durations have the added desirable effect of requiring less total energy to ablate a given amount of propellant. One conclusion that can be drawn from these results is that the amount of propellant expelled at any propellant temperature can be calculated if the heat flux profile and propellant consumed per pulse at any other specific temperature are known. This has important implications for control system feedback by monitoring of propellant temperature and onboard evaluation of propellant usage. These results also suggest that running a given PPT configuration at higher discharge energy can improve long-term ablation efficiency. This has been experimentally verified to some extent since it has been found to reduce charring, but limits do appear to exist. Beyond a certain point, experimental studies show that high discharge energies tend to degrade performance due to non-uniform arc distribution and other phenomenon associated with the plasma interaction. It is thus not clear if the theoretical ablation benefits of high discharge energies can be achieved in actual devices.

Results also show that in general mass flux profiles tend to lag the main applied heat flux profile. This lag is likely responsible for much of the poor propellant utilization observed experimentally in pulsed plasma thrusters. The electromagnetic acceleration is likely small by the time the highest ablation rate is achieved. Under-damped heat flux profiles appear even less efficient because less of the thermal energy goes toward ablation and more is lost as residual heat in the bulk propellant. Consequently, a

sharp termination in heat flux is required to decrease late-time ablation characteristics, but achieving it may prove difficult. However, even small amounts of residual-heat flux applied after the main pulse extend the mass ablation profile, so efforts should be made to maximize the rate at which the heat flux drops to zero.

Particulate emission, another source of poor propellant utilization, is still not well understood. It likely occurs only when amorphous material is still present at the propellant surface. This dependence is not yet established experimentally but may be a consequence of the weak structural properties of the viscous amorphous Teflon. This hypothesis is plausible since numerical results indicate amorphous re-crystallization lasts far longer than the experimentally documented time period of particulate emission. If this hypothesis is correct, then minimizing the effects of particulate emission requires minimizing the time required to re-crystallize propellant after a pulse. This appears to be possible through many of the same measures that boost other aspects of PPT efficiency such as reduced bulk propellant temperature, increased heat flux, shorter heat flux application time, and swift termination of the heat flux profile.

A final conclusion can be derived from the numerical simulation: Ablation processes and thermo-physical behavior are extremely sensitive to assumed material properties and material property variability. In fact, they appear to be far more sensitive in Pulsed Plasma Thrusters than in more generic ablation situations. The lack of precise material property values means the majority of results that can be drawn from numerical analysis of PPTs are qualitative. Exact comparison with many characteristics of experimental performance is difficult. Timing aspects of the firing process is one exception because these appear to be less affected by material property uncertainty than other conditions such as mass flux.

7.2 Recommendations for Future Work

The results demonstrated in this work show progress in obtaining a more complete understanding of PPT behavior and a more thorough tool for evaluating Teflon ablation. However, additional progress is limited by several factors. The primary challenge is the lack of reliable high-temperature Teflon material properties. As was demonstrated, ablation performance appears to be very sensitive to these properties and the significant uncertainties in this area make it difficult to generate meaningful comparisons with actual devices. Consequently, it is vitally important to determine accurate property values to facilitate the development of tools such as this ablation model. These properties should account for the different types of Teflon because this would allow experimental and numerical researchers to compare data and results more consistently.

Additional avenues for future work also lie in refining some of the key assumptions used in developing this model. For example, in-depth radiative absorption is considered insignificant in PPTs because of previous work indicated that plasma conduction is the primary mode of heat transfer.

Unfortunately this is only a qualitative assessment. The decision to neglect thermal expansion is similar. In reality, the effects of in-depth radiation or thermal expansion may be sufficient to warrant consideration in future expansions of this model. The use of a one-dimensional Teflon domain may also require re-evaluation in certain circumstances such as smaller device scales, where edge effects and side-wall heat transfer losses can become more significant. Regardless, expanding the ablation model into two or even three dimensions could allow more accurate analysis of a wider variety of ablation situations and PPT geometries.

The ablation model has a final limitation that requires more work. The kinetic description of the ablation process described in previous chapters depends upon known heat flux conditions. Unfortunately, these are often difficult to observe or may be unknown altogether. At the minimum, efforts should be made to better characterize this heat flux profile in given thruster configurations and discharges. A more sophisticated approach would include a model of the plasma processes to obtain thruster heat flux conditions from more measurable parameters such as circuit current. Numerous plasma models have been developed with this capability, but these use mass flux input conditions obtained from simplified ablation models. A much more complete and accurate system would result if the ablation model described in this thesis could be coupled with any of the highly sophisticated plasma models already developed.

References

1. Antonsen, E. L., Burton, R. L., Reed, G. A., and Spanjers, G. G., "Effects of Postpulse Surface Temperature on Micropulsed Plasma Thruster Operation." *Journal of Propulsion and Power*, Vol. 21, No. 5, 2005, pp. 877 - 883.
2. Arai, N., "A Study of Transient Thermal Response of Ablating Materials." Institute of Space and Aeronautical Science, University of Tokyo. Report No. 544. Vol. 41, No. 8. 1976.
3. Arai, N., Karachima, K., and Sato, K., "Transient Ablation of Teflon Hemispheres." *AIAA Journal*, Vol. 15, No. 11, 1977, pp. 1655, 1656.
4. Arai, N., "Transient Ablation of Teflon in Intense Radiative and Convective Environments." *AIAA Journal*, Vol. 17, No. 6, 1979, pp. 634 – 640.
5. Arai, N., and Karashima, K., "Transient Thermal Response of Ablation Bodies." *AIAA Journal*, Vol. 17, No. 2, 1979, pp. 191 – 195.
6. Bespalov, V. L., and Zalogin, G. N., "Ablation of Teflon in a Stream of Dissociated Air." *Izvestiya Akademii Nauk SSSR, Mekhanika Zhidkosti I Gaza*, No. 3, 1984, pp. 103 – 109.
7. Bhutta, B. A., and Lewis, C. H., "New Technique for Low-to-High Altitude Predictions of Ablative Hypersonic Fields." *Journal of Spacecraft and Rockets*, Vol. 29, No. 1, 1992, pp. 35 – 50.
8. Boyd, I. D., Keidar, M., and McKeon, W., "Modeling of a Pulsed Plasma Thruster from Plasma Generation to Plume Far Field." *Journal of Spacecraft and Rockets*, Vol. 37, No. 3, 2000, pp. 399 – 407.
9. Boyd, Iain D., "Numerical Modeling of Spacecraft Electric Propulsion Thrusters," *Progress in Aerospace Sciences*, Vol. 41, 2006. pp. 669 - 687.
10. Burton, R.L., Turchi, P. J., "Pulsed Plasma Thruster," *Journal of Propulsion and Power*, Vol. 14, No. 5, pp. 716, 1998.
11. Bushman, S. S., and Burton, R. L., "Heating and Plasma Properties in a Coaxial Gasdynamic Pulsed Plasma Thruster." *Journal of Propulsion and Power*, Vol. 17, No. 5, 2001, pp. 959 – 956.

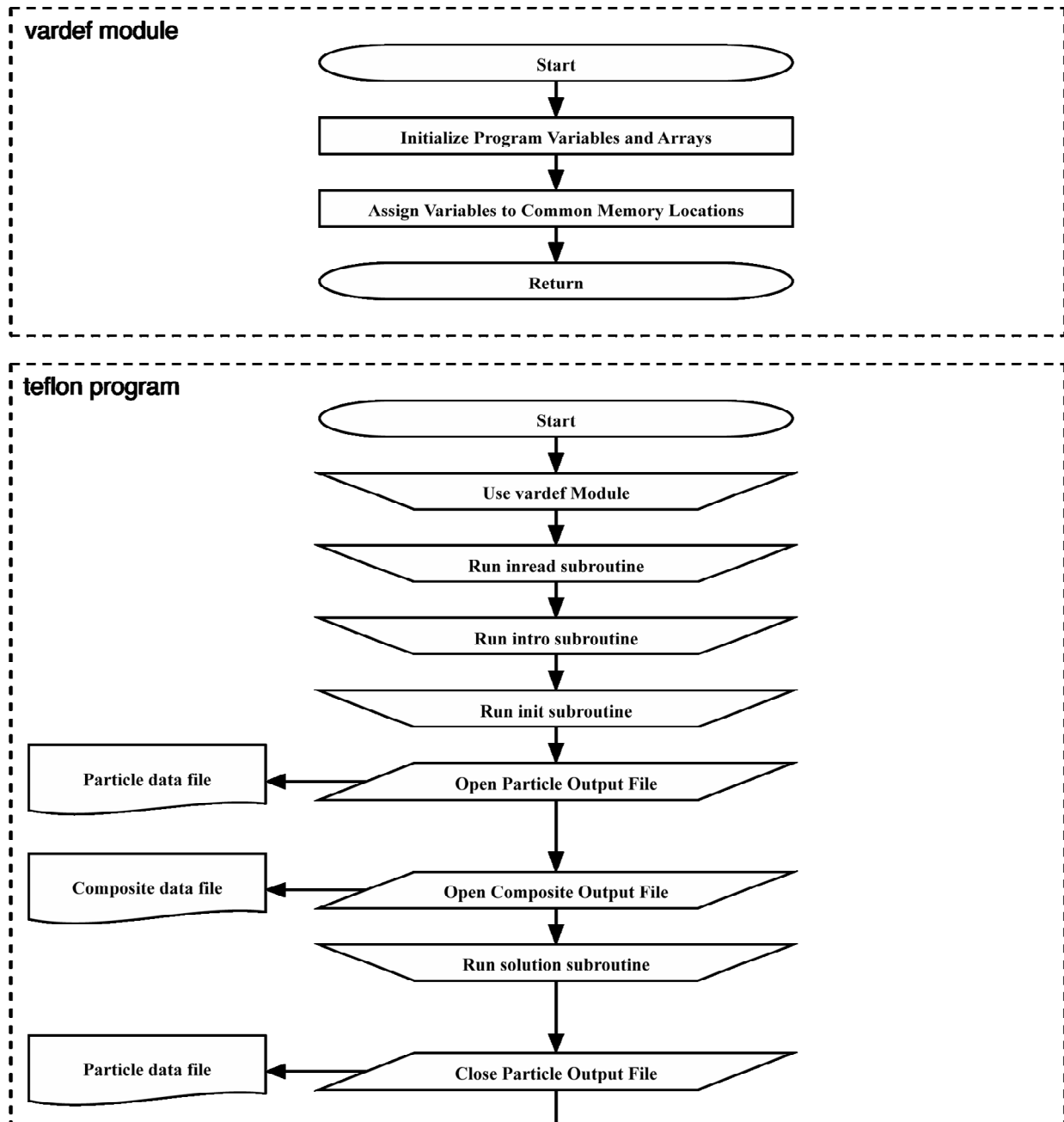
12. Chung, B. T. F., and Hsiao, J. S., "Heat Transfer with Ablation in a Finite Slab Subjected to Time-Variant Heat Fluxes." *AIAA Journal*, Vol. 23, No. 1, 1985, pp. 145 – 150.
13. Clark, B. L., "An Experimental and Analytical Investigation of Teflon Ablation Heat Transfer Parameters by the Method of Non-Linear Estimation," Cornell University, 1971.
14. DuPont, "DuPont Teflon PTFE Fluoropolymer Resin Properties Handbook." DuPont Corporation, 2004.
15. Eckert, E. R. G., and Drake Jr, R. M., *Analysis of Heat and Mass Transfer*, Hemisphere Publishing Corporation, Washington, DC, 1987, Chaps. 4, 5.
16. Gatsonis, N. A., Eckman, R., Yin, X., Pencil, E. J., and Myers, R. M., "Experimental Investigations and Numerical Modeling of Pulsed Plasma Thruster Plumes." *Journal of Spacecraft and Rockets*, Vol. 38, No. 3, 2001, pp. 454 – 464.
17. Gatsonis, N. A., Yin, X., "Hybrid (Particle-Fluid) Modeling of Pulsed Plasma Thruster Plumes." *Journal of Propulsion and Power*, Vol. 17, No. 5, 2001, pp. 945 – 957.
18. Holzknecht, B., "An Analytical Model of the Transient Ablation of Polytetrafluoroethylene Layers." *International Journal of Heat and Mass Transfer*, Vol. 20, 1977, pp. 661 – 668.
19. Hogan, R. E., Blackwell, B. F., and Cochran, R. J., "Application of Moving Grid Control Volume Finite Element Method to Ablation Problems." *Journal of Thermophysics and Heat Transfer*, Vol. 10, No. 1, 1996, pp. 312 – 319.
20. Hogge, M. and Gerrekens, P., "Two-Dimensional Deforming Finite Element Methods for Surface Ablation." *AIAA Journal*, Vol. 23, No. 3, 1985, pp. 465 – 472.
21. Keidar, M., Boyd, I. D., Beilis, I. I., "Electrical Discharge in the Teflon Cavity of a Coaxial Pulsed Plasma Thruster." *IEEE Transactions on Plasma Science*, Vol. 28, No. 2, 2000, pp. 376 – 385.
22. Keidar, M., Boyd, I. D., Beilis, I. I., "Modeling of a Pulsed Plasma Thruster from Plasma Generation to Plume Far Field." *Journal of Spacecraft and Rockets*, Vol. 37, No. 3, 2000, pp. 399 – 407.
23. Keidar, M., Boyd, I. D., and Beilis, I. I., "Model of Particulate Interaction with Plasma in a Teflon Pulsed Plasma Thruster." *Journal of Propulsion and Power*, Vol. 17, No. 1, 2001, pp. 125 – 131.
24. Keidar, M., Boyd, I. D., Beilis, I. I., "On the model of Teflon ablation in an ablation-controlled discharge." *Journal of Physics D: Applied Physics*, Vol. 34, 2001, pp. 1675 – 1677.

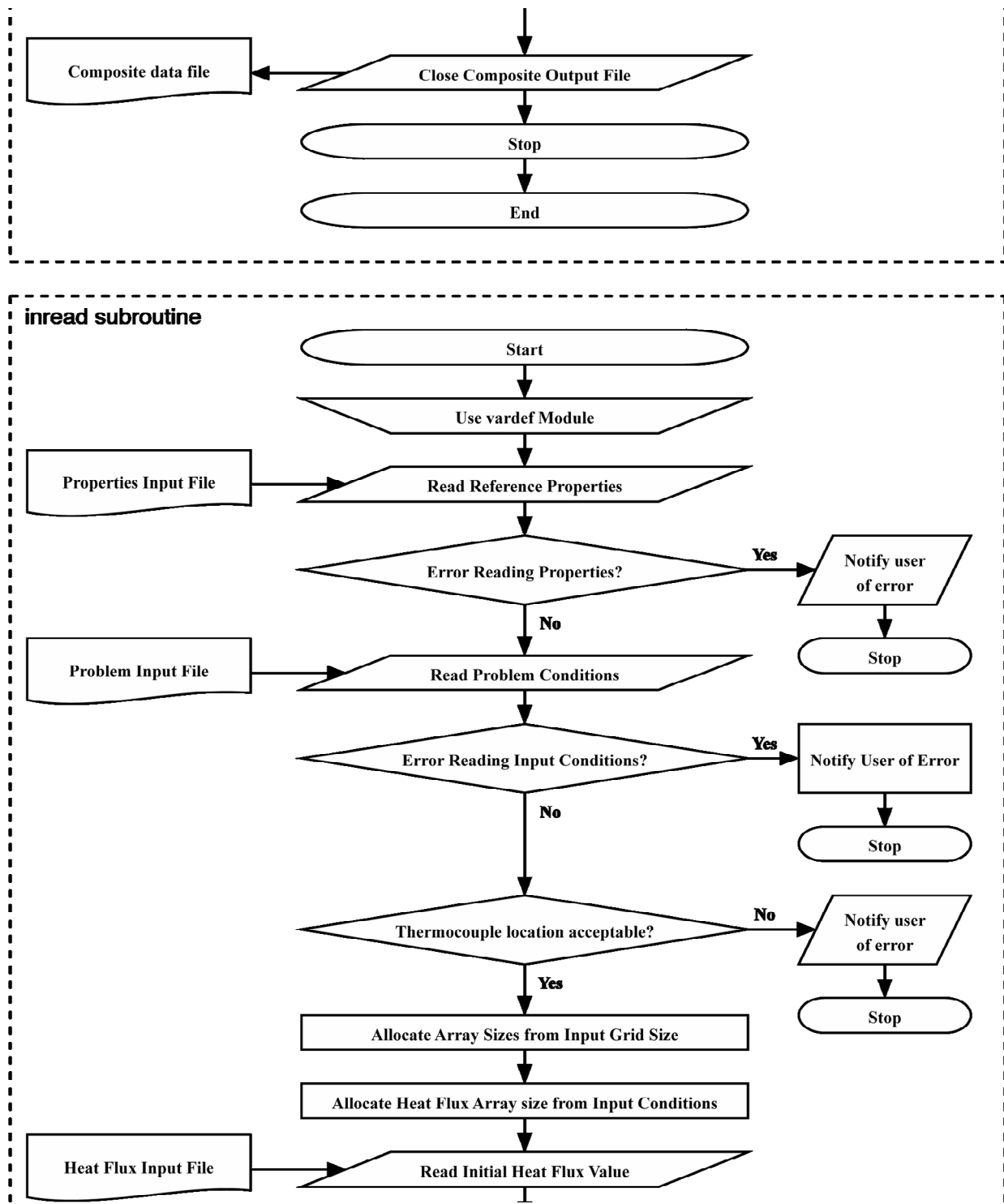
25. Keidar, M., Boyd, I. D., Antonsen, E. L., Gulezinski III, F. S., and Spanjers, G. G., "Propellant Charring in Pulsed Plasma Thrusters." *Journal of Propulsion and Power*, Vol. 20, No. 6, 2004, pp. 978 – 984.
26. Keidar, M., Boyd, I. D., Antonsen, E. L., Burton, R. L., and Spanjers, G. G., "Optimization Issues for a Micropulsed Plasma Thruster." *Journal of Propulsion and Power*, Vol. 22, No. 1, 2006, pp. 48 – 55.
27. Kemp, N. H., "Surface Recession Rate of an Ablating Polymer." *AIAA Journal*, Vol. 6, No. 9, 1968, pp. 1790, 1791.
28. Laperriere, D. D., Gatsonis, N. A., and Demetriou, M. A., "Electromechanical Modeling of Applied Field Micro Pulsed Plasma Thrusters." *41st AIAA/ASME/SAE/ASEE Joint Propulsion Conference and Exhibit*, AIAA-2005-4077, Tucson, AZ, 2005.
29. Lin, G., Karniadakis, G. "High Order Modeling of MicroPPTs," AIAA Paper 2002-2872, 2002.
30. Luikov, A. V., Shashkov, A. G., and Yurevich, F. B., "Polytetrafluoro-Ethylene Ablation in High-Temperature Jet of Different Chemical Compositions." *International Journal of Heat and Mass Transfer*, Vol. 12, 1969, pp. 635 – 643.
31. Michels, C. J., Heighway, J. E., and Johansen, A. E., "Analytical and Experimental Performance of Capacitor Powered Coaxial Plasma Guns." *AIAA Journal*, Vol. 4, No. 5, 1966, pp. 823 – 830.
32. Mikellides, Y. G., "Theoretical Modeling and Optimization of Ablation-Fed Pulsed Plasma Thrusters." Ohio State University, 1999.
33. Milos, F. S., and Rasky, D. J., "Review of Numerical Procedures for Computational Surface Thermochemistry." *Journal of Thermophysics and Heat Transfer*, Vol. 8, No. 1, 1994, pp. 24 – 34.
34. Pope, R. B., "Simplified Computer Model for Predicting the Ablation of Teflon." *Journal of Spacecraft*, Vol. 12, No. 2, 1975, pp. 83 – 88.
35. Shih, Y. C., Cheung, F. B., Koo, J. H., and Yang, B. C., "Numerical Study of Transient Thermal Ablation of High Temperature Insulation Materials." *Journal of Thermophysics and Heat Transfer*, Vol. 17, No. 1, 2003, pp. 53 – 61.
36. Spanjers, G. G., Malak, J. B., Leiweke, R. J., and Spores, R. A., "Effect of Propellant Temperature on Efficiency in the Pulsed Plasma Thruster." *Journal of Propulsion and Power*, Vol. 14, No. 4, 1998, pp. 545 – 553.

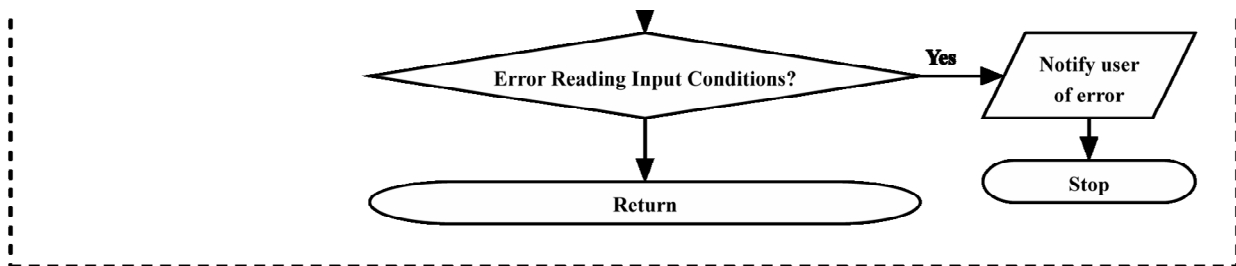
37. Spanjers, G. G., Lotspeich, J. S., McFall, K. A., and Spores, R. A., "Propellant Losses Because of Particulate Emission in a Pulsed Plasma Thruster." *Journal of Propulsion and Power*, Vol. 14, No. 4, 1998, pp. 554 – 559.
38. Tannehill, J. C., Anderson, D. A. and Pletcher, R. H., *Computational Fluid Mechanics and Heat Transfer*, 2nd ed, Hemisphere Publishing Corporation, Washington, DC, 1997, Chap. 7.
39. Turchi, P.J., and Mikellides, P.G., "Modeling of Ablation-Fed Pulsed Plasma Thrusters." *31st AIAA/ASME/SAE/ASEE Joint Propulsion Conference and Exhibit*, AIAA 95-2915, San Diego, CA, 1995.
40. Vojvodich, N. S., and Pope, R. B., "Effects of Gas Composition on the Ablation Behavior of a Charring Material." *AIAA Journal*, Vol. 2, No. 3, 1964, pp. 536 – 542.
41. Wei, C. Y., and Zien, T. F., "Integral Calculations of Melt-Layer Heat Transfer in Aerodynamic Ablation." *Journal of Thermophysics and Heat Transfer*, Vol. 15, No. 1, 2001, pp. 116 – 124.
42. Wentink, T. Jr. "High Temperature Behavior of Teflon." Avco Everett Research Laboratory. Report No. 55. July 1959.
43. Zien, T. F., "Integral Solutions of Ablation Problems with Time-Dependent Heat Flux." *AIAA Journal*, Vol. 16, No. 12, 1978, pp. 1287 – 1295.

Appendix A

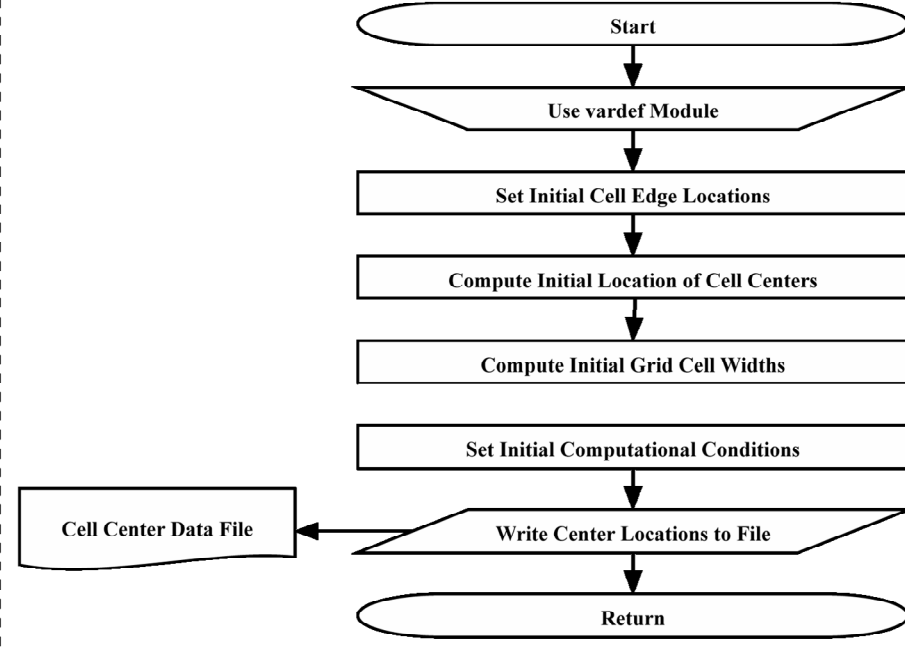
One Dimensional Program Architecture



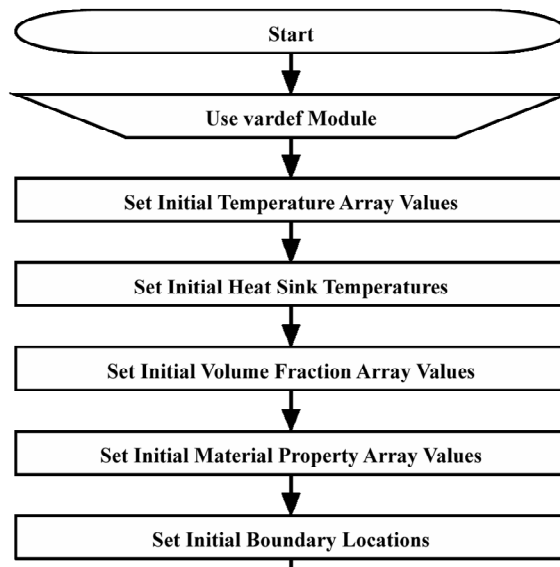


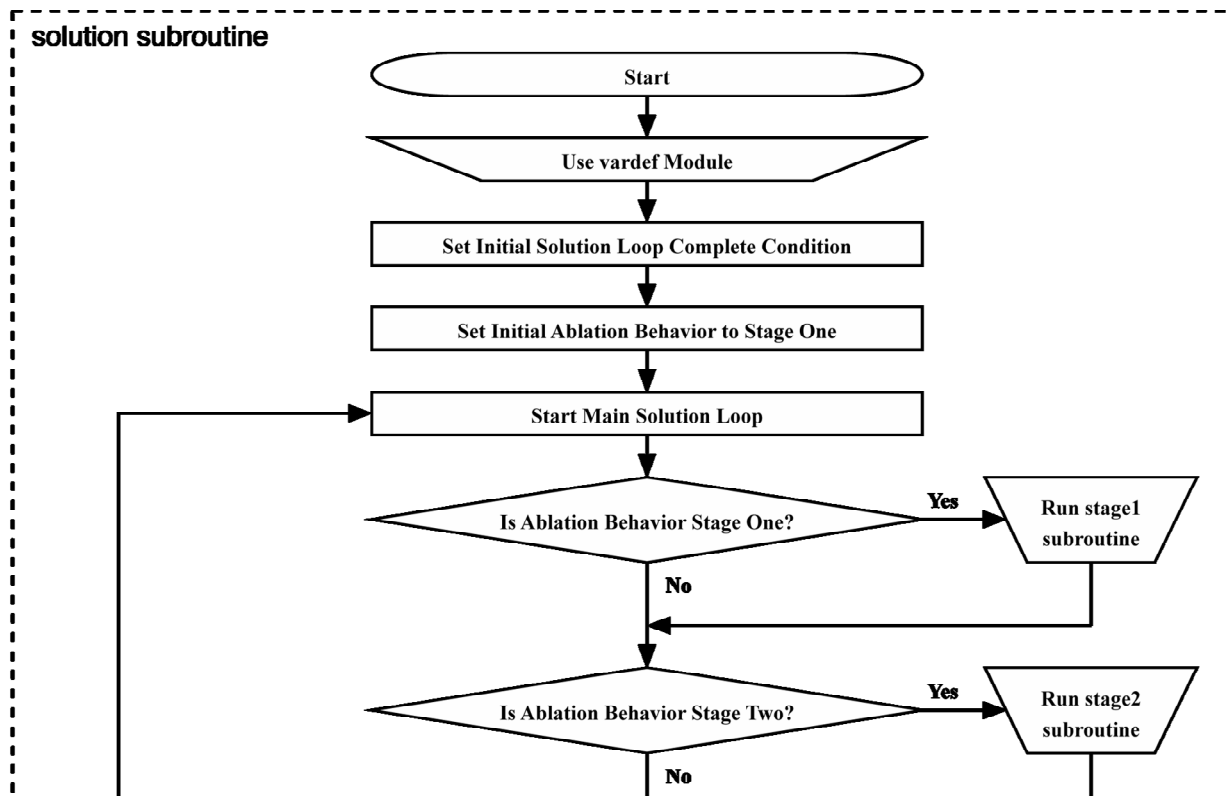
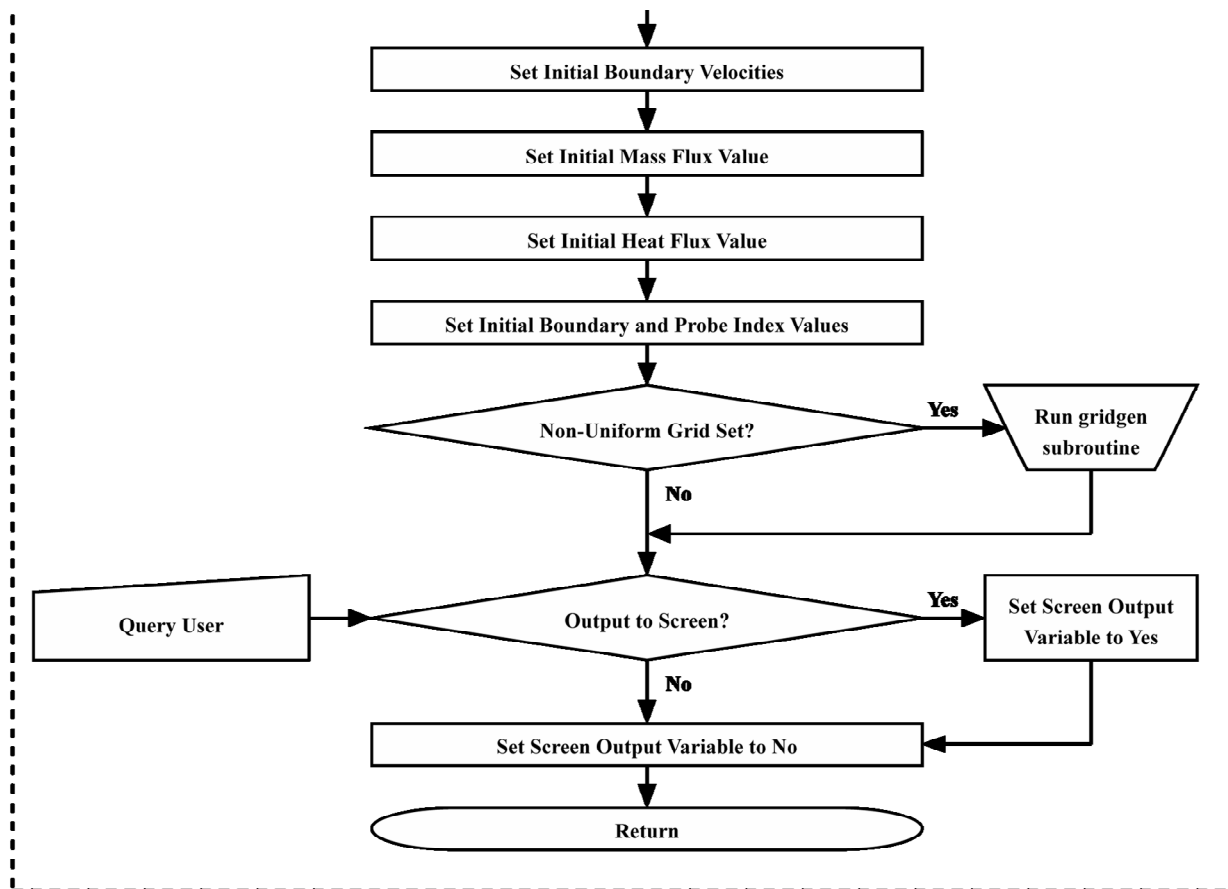


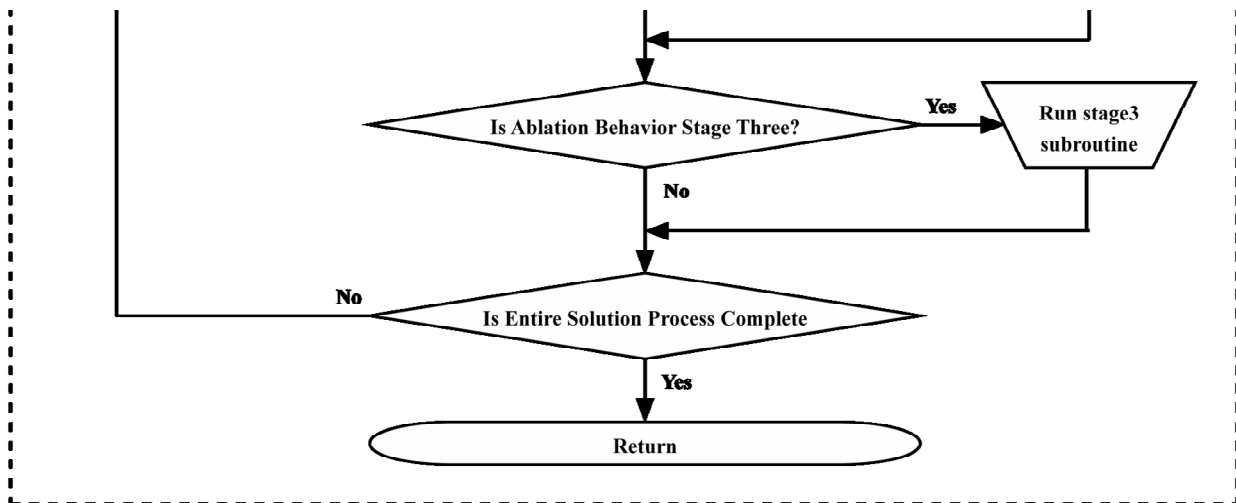
intro subroutine



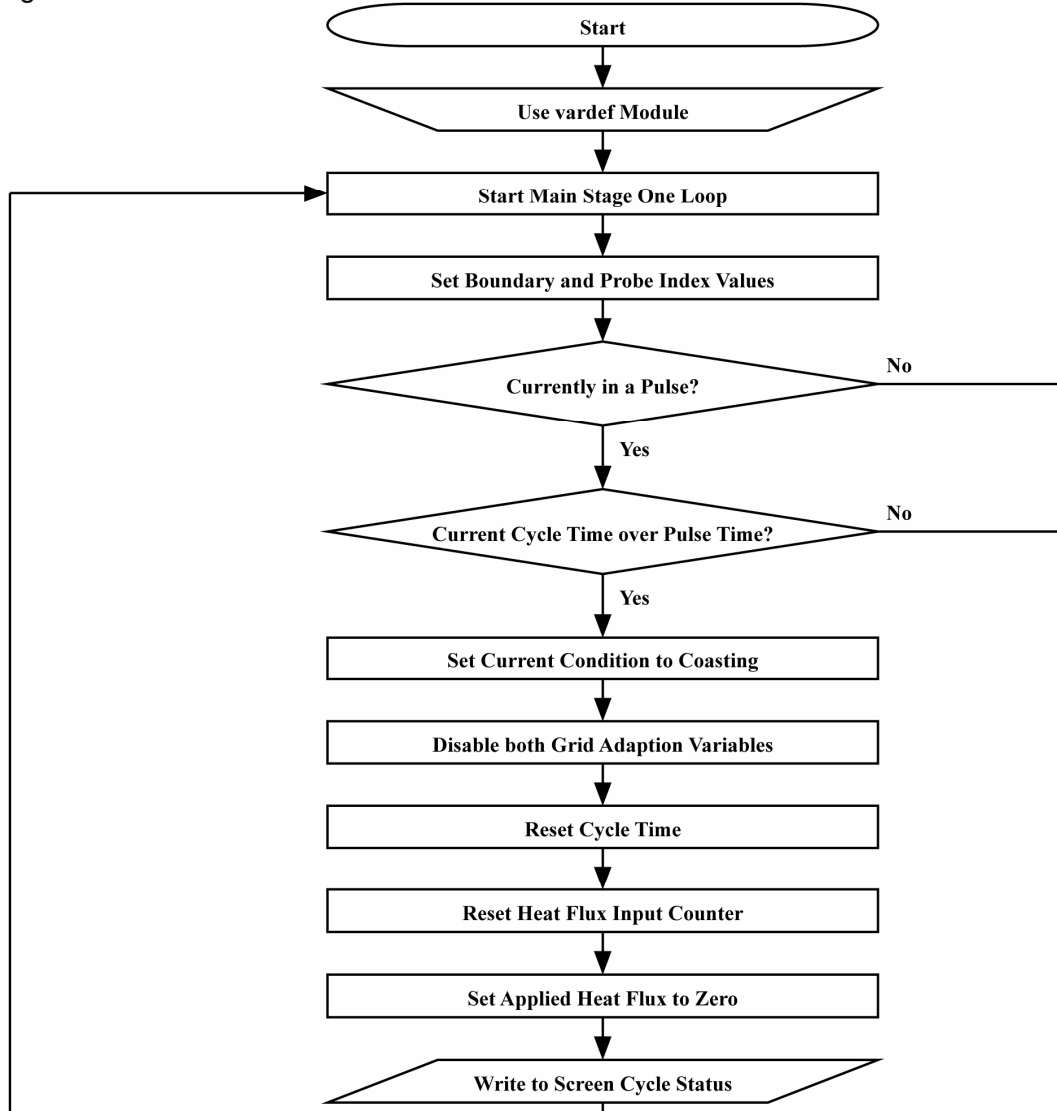
init subroutine

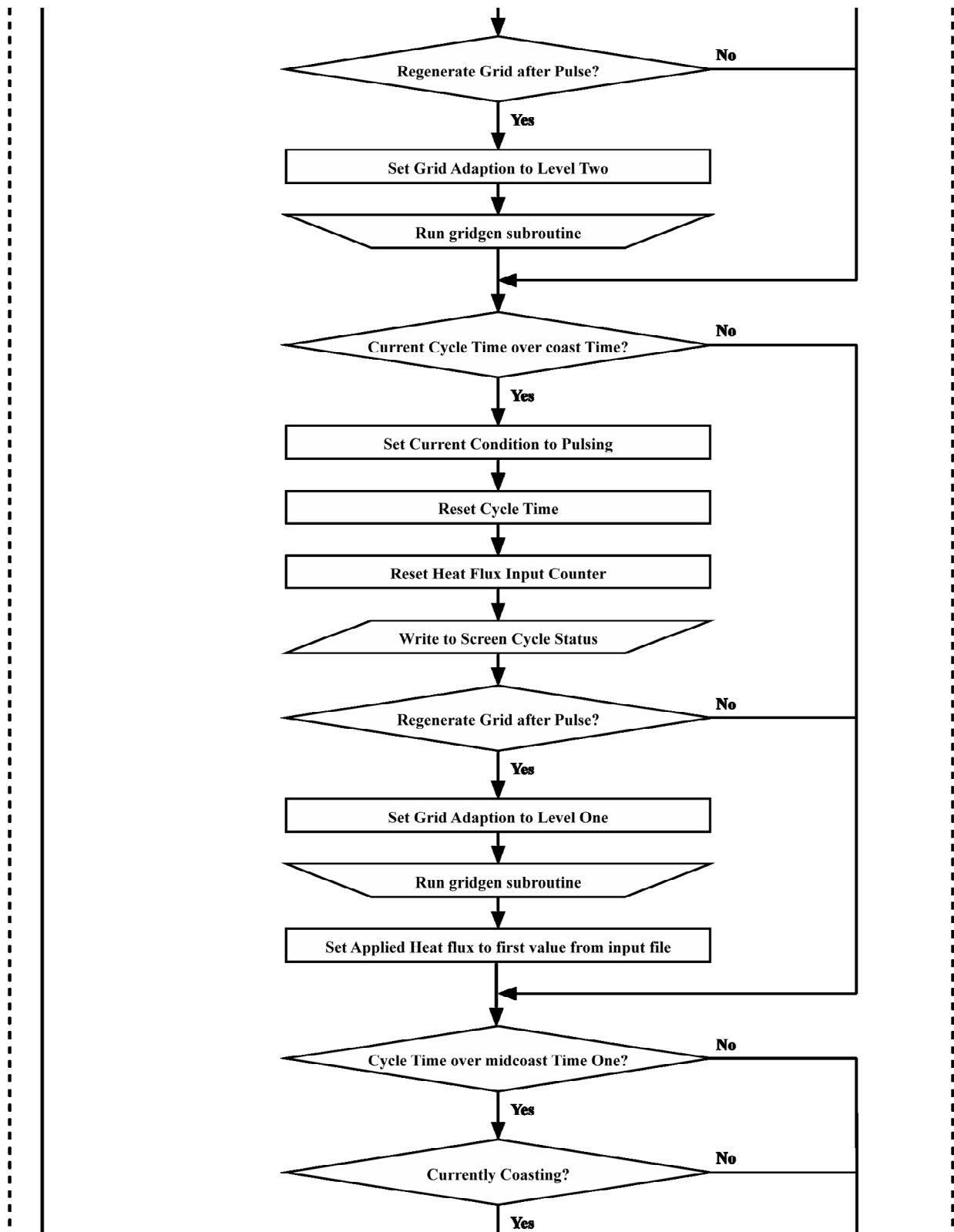


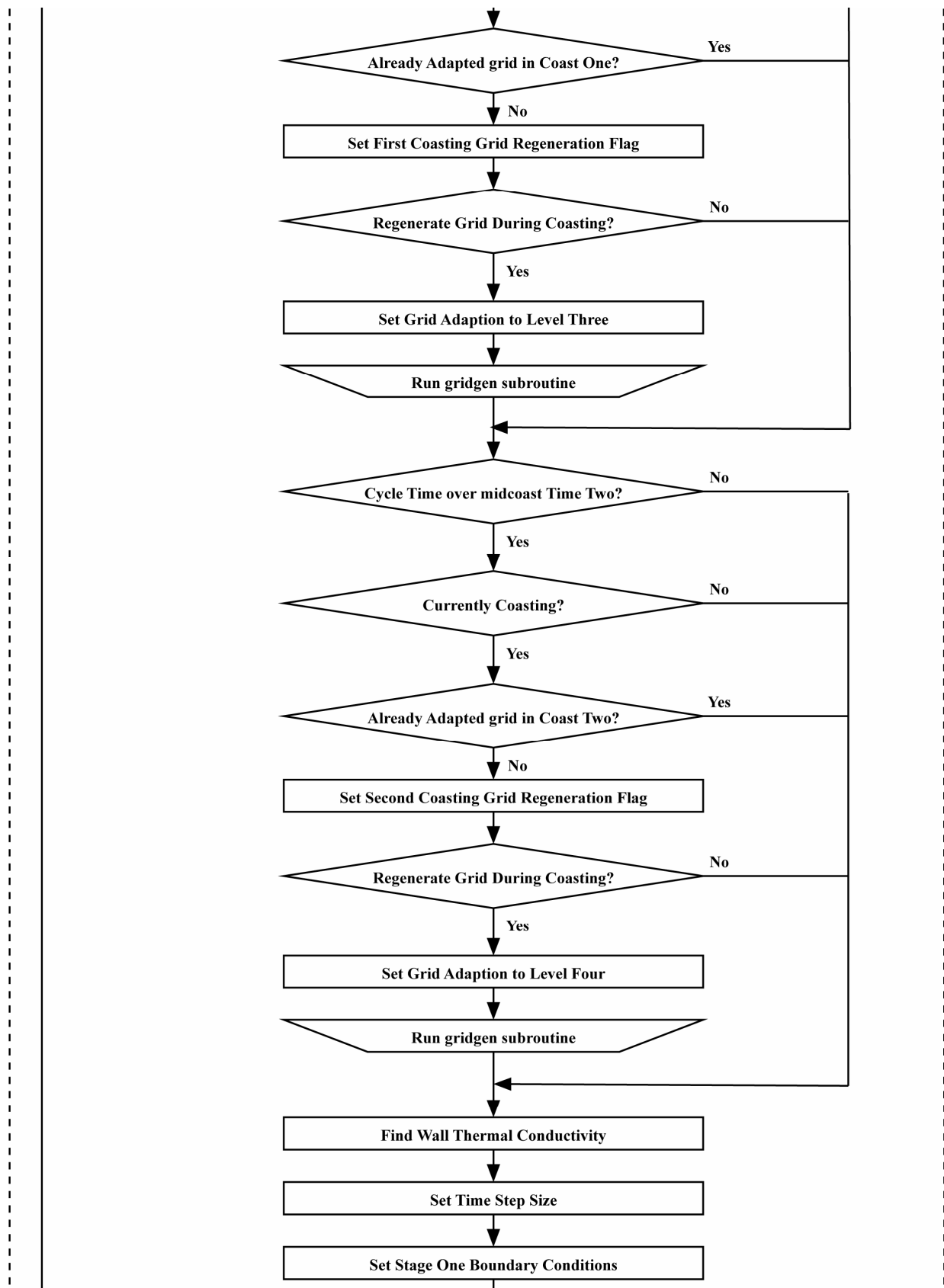


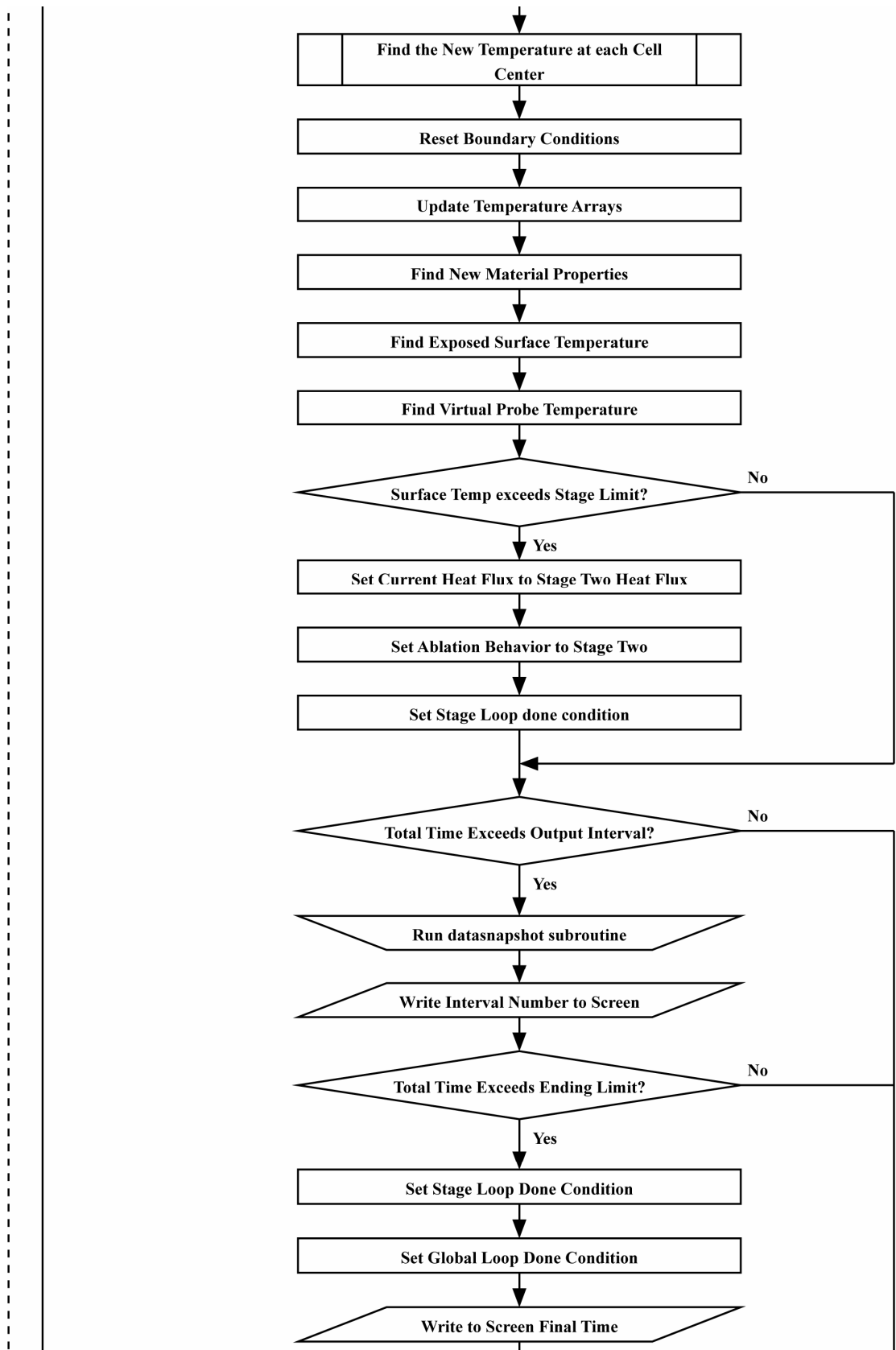


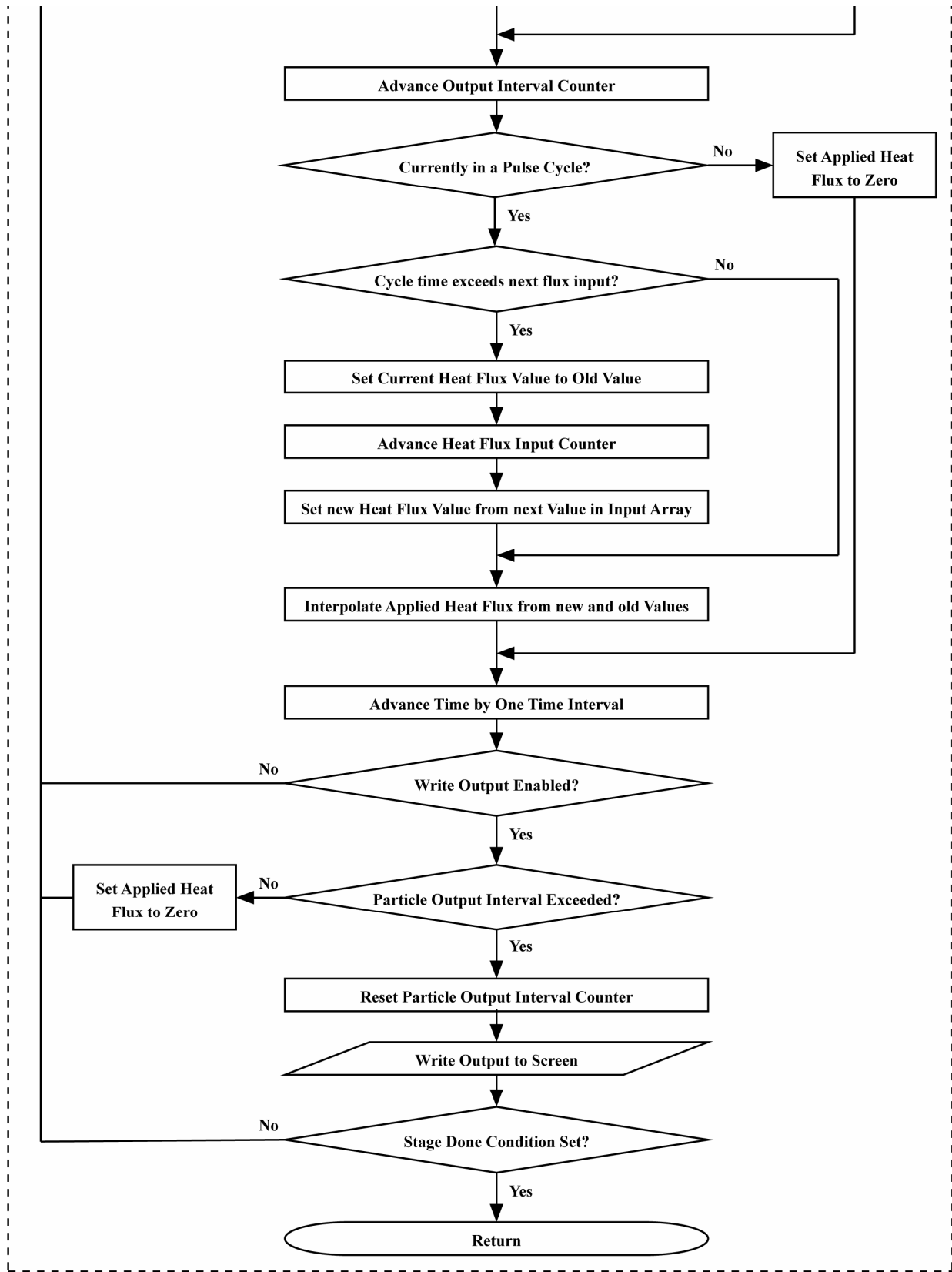
stage1 subroutine



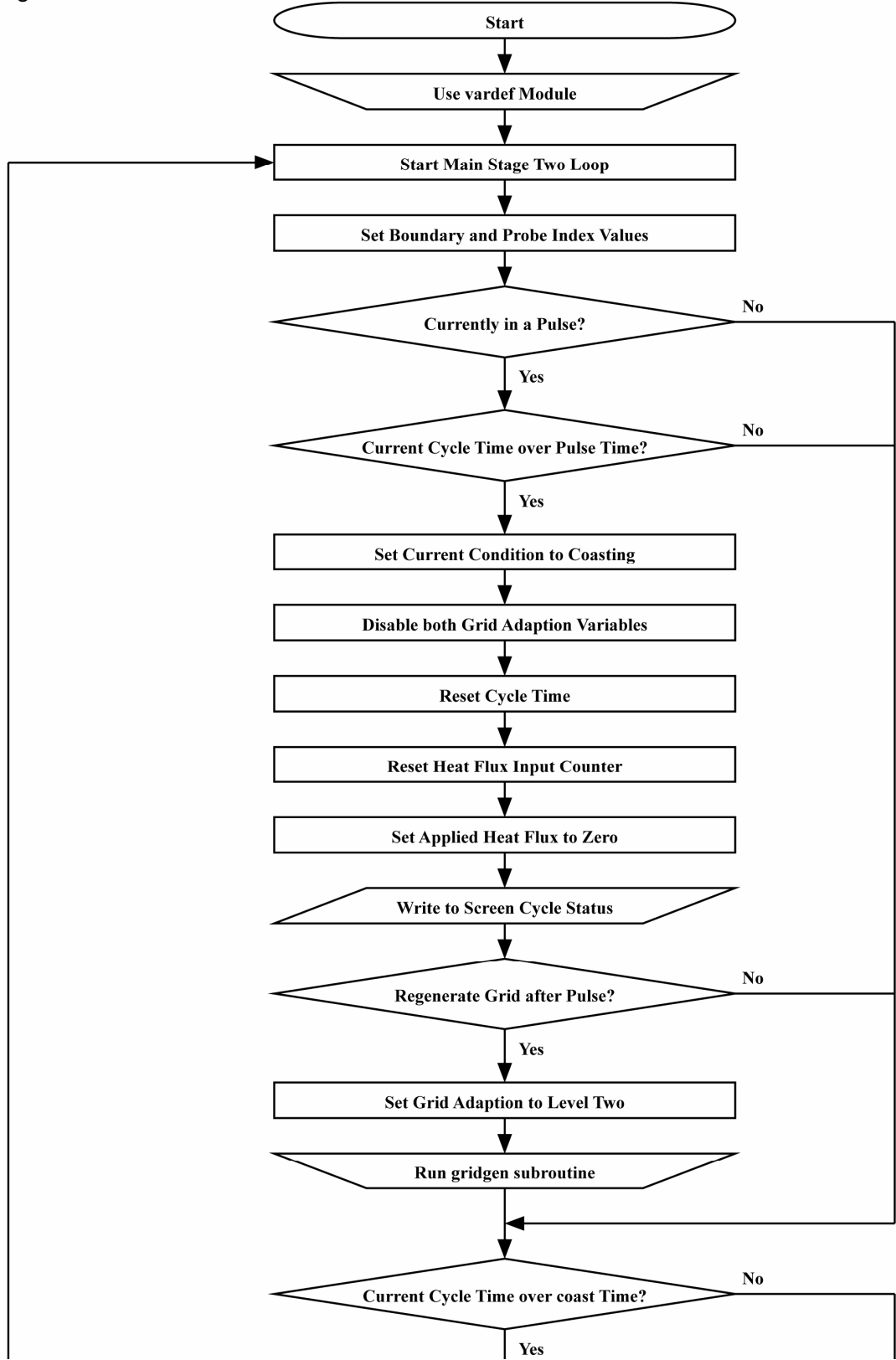


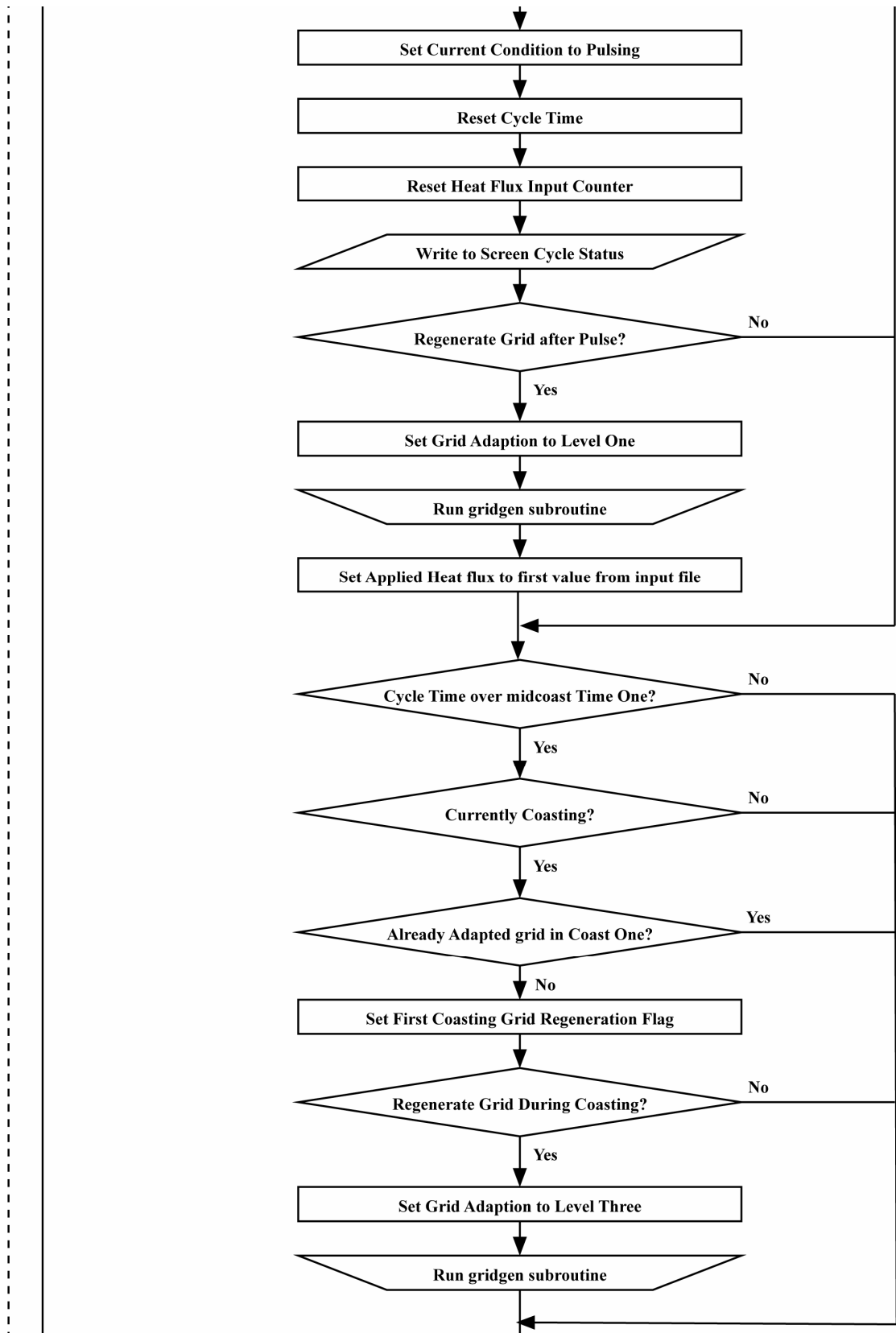


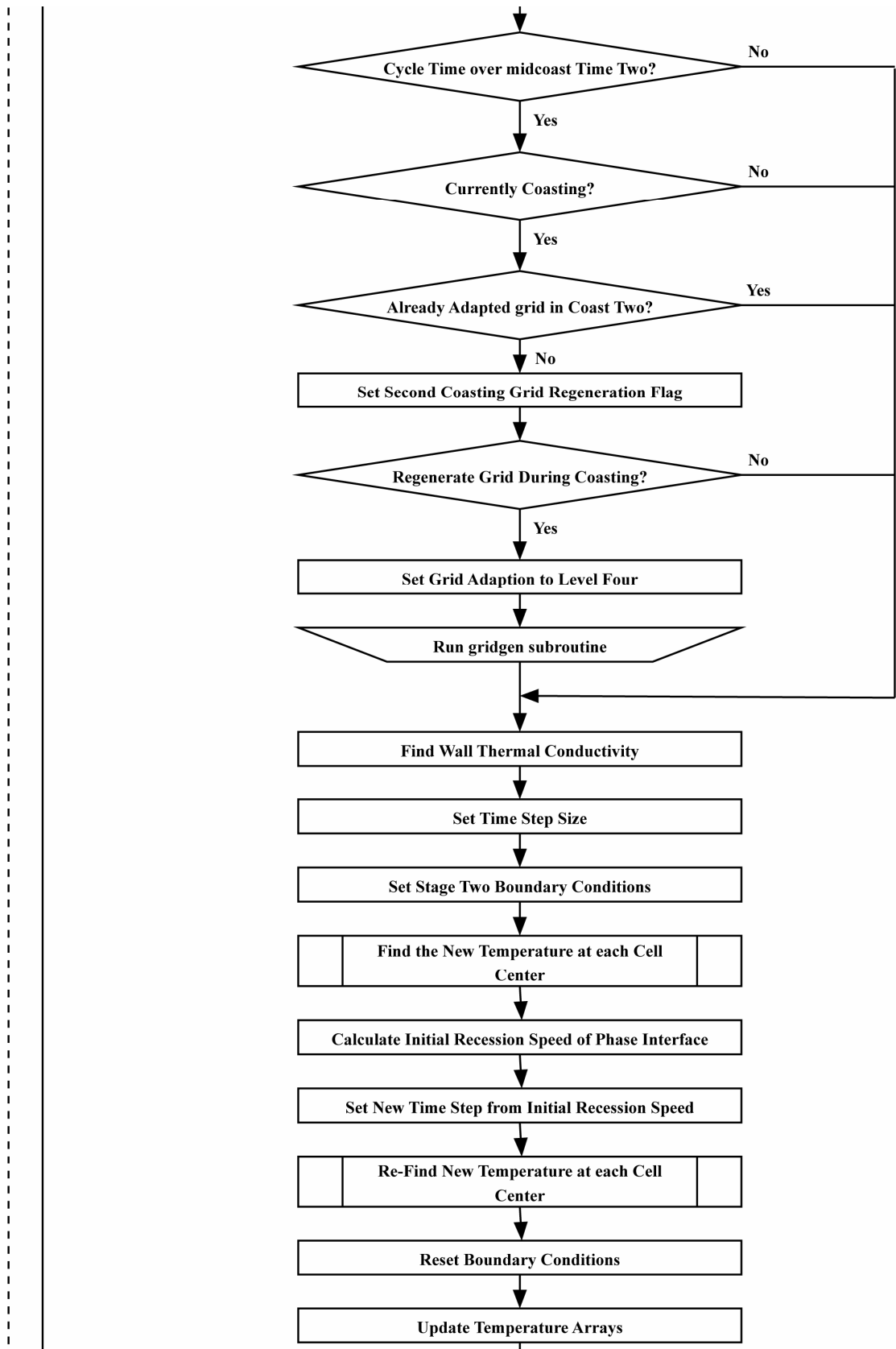


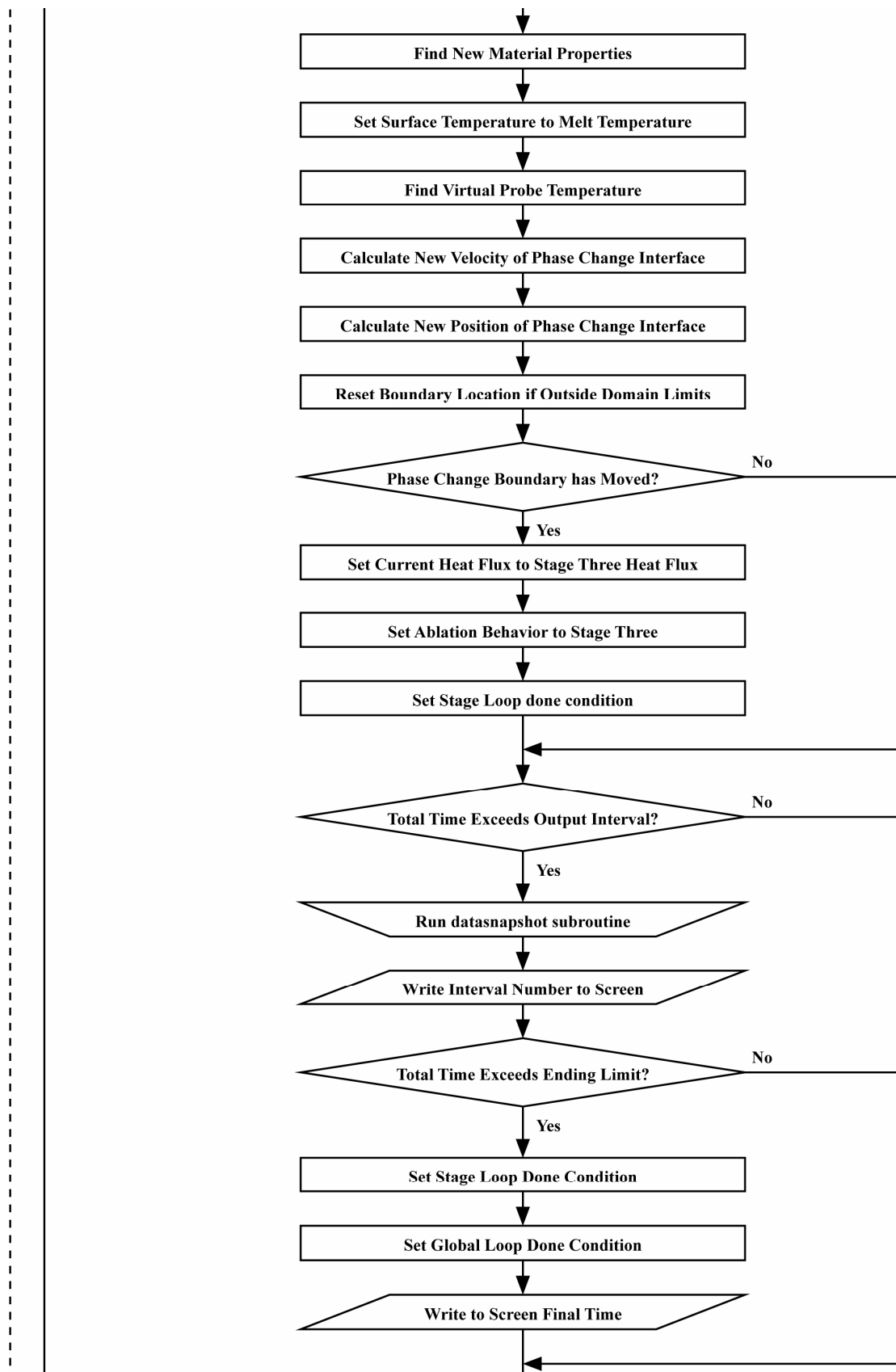


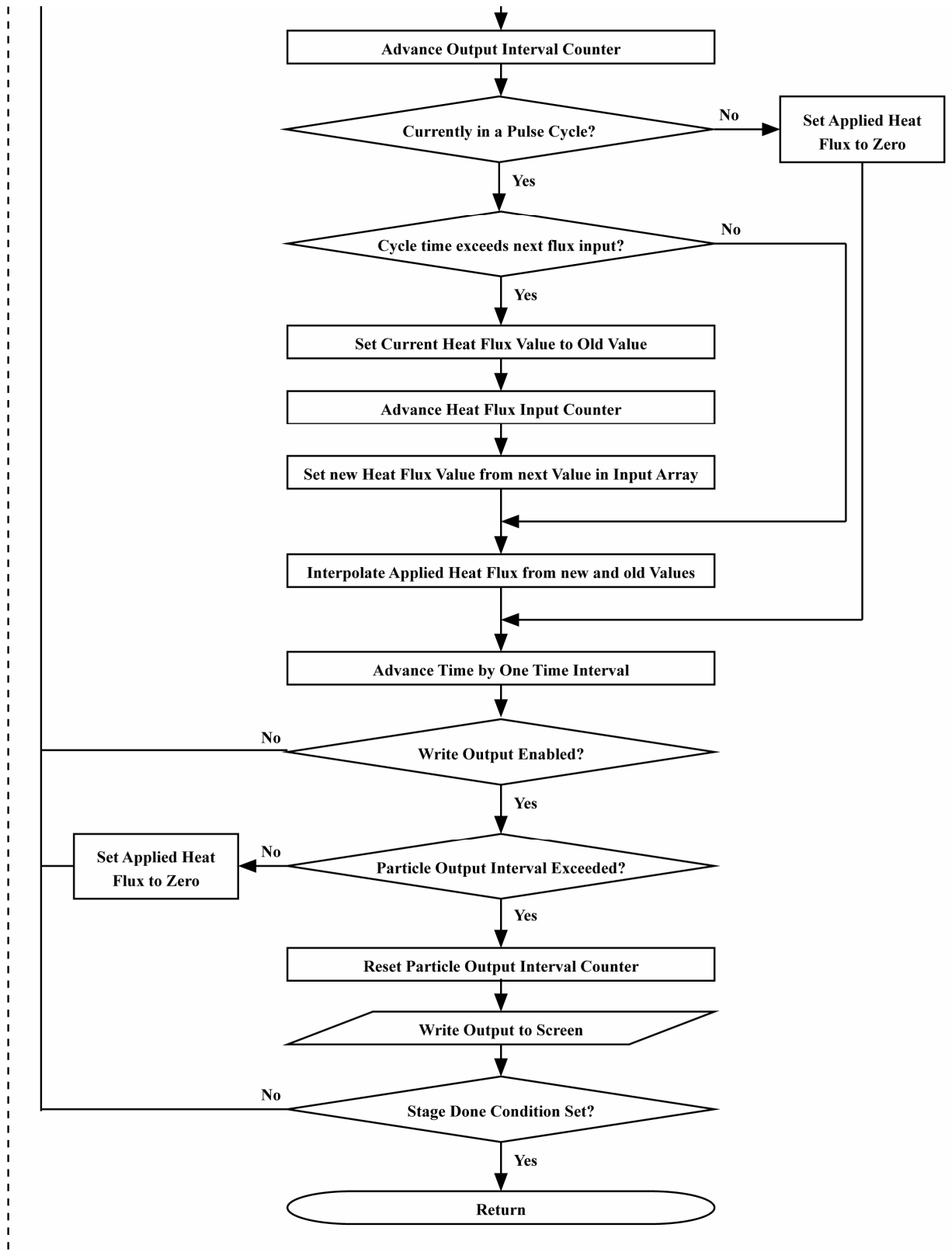
stage2 subroutine











stage3 subroutine

